THÈSE

En vue de l'obtention du

DOCTORAT DE L'UNIVERSITÉ DE TOULOUSE

Délivré par :

Institut National Polytechnique de Toulouse (Toulouse INP)

Discipline ou spécialité :

Dynamique des fluides

Présentée et soutenue par :

M. YOUSSEF NASRO-ALLAH

le lundi 16 décembre 2019

Titre :

Experimental and numerical investigation of electrostatic effects in gas-solid fluidized beds

---

Ecole doctorale :

Mécanique, Energétique, Génie civil, Procédés (MEGeP)

Unité de recherche :

Laboratoire de Génie Chimique (LGC)

Directeur(s) de Thèse :

M. RODNEY FOX

M. RENAUD ANSART

Rapporteurs :

M. HANS KUIPERS, TECHNISCHE UNIVERSITEIT EINDHOVEN

Mme POUPAK MEHRANI, CARLETON UNIVERSITY OTTAWA

Membre(s) du jury :

M. OLIVIER SIMONIN, TOULOUSE INP, Président

M. ALI OZEL, HERIOT WATT UNIVERSITY, Membre

M. JAN BAEYENS, UNIVERSITE DE BEIJING, Membre

Mme ENRICA MASI, UNIVERSITE PAUL SABATIER, Membre

M. RENAUD ANSART, TOULOUSE INP, Membre

M. RODNEY FOX, IOWA STATE UNIVERSITY, Membre

Abstract

Youssef NASRO-ALLAH

Experimental and numerical investigation of electrostatic charges in gas-solid fluidized beds

Keywords: fluidized bed, electrostatic charges, tribocharging, relative humidity, Euler-Euler, CFD.

Gas-solid fluidized beds are widely used in industrial processes for energy such as chemical looping combustion, catalytic polymerization, solar receiver, biomass gasification, polymerization (polyethylene catalytic reactors), and petroleum refinery (fluidized catalytic crackers). In all these processes electrostatic forces were usually neglected and their contribution to force balance considered as a second order in gas-solid fluidized beds. In polyolefin industry, the phenomena of electrostatic charges presents a major issues including wall fouling (particle accumulation on the walls), defluidization...etc. . Moreover, this phenomenon may present some safety issues due to sparks or dust explosions. At a molecular scale, the contact between two particles (particle-wall or particle-particle) generates a transfer of electrons/ions, inducing a charge on each particle. As a result, the surrounding gas carries an electric field. This electric field results in an additional force to the momentum equation known as Lorentz force. The electrostatic phenomenon has been studied for years using both experimental and numerical approach which gives a better understanding but also several discrepancies between findings in literature. The charge generation and charge transfer depend on many parameters, mainly materials properties and operating conditions, including gas relative humidity, gas velocity, pressure and temperature (Park et al. 2002; Sowinski et al. 2010).

Several works in literature studied the effect of each parameter whether through electrostatic probes (intrusive method) or Faraday cups (non-intrusive method). However, there is a lack of research projects which combine both experimental study and theoretical modeling with numerical simulation. Thus, this study falls within the context, with an entitled subject "Experimental and numerical investigation of electrostatic effects in gas-solid fluidized beds". The thesis research program is a part of the Attractivity Chair BIREM (BIological, REacting, Multiphase flows) attributed to Professor Rodney Fox, financially supported by the University of Toulouse, in the framework of the IDEX research program. The project, hosted by the research federation FERMaT, brings together four laboratories from the University of Toulouse in various fields: the Institut de Mécanique des Fluides de Toulouse (IMFT), the Laboratoire d'Ingénierie des Systèmes Biologiques et des Procédés (LISBP), the Laboratoire de Génie Chimique (LGC) and the Institut de Mathématiques de Toulouse

(IMT).

The study aims to combine both experimental data on electrostatic charges in a lab-scale pilot and the numerical modeling to represent inter-particle forces at micro-scaleand to implement in CFD code through the Euler-Euler formalism at micro scale according to the kinetic theory of granular media.

In this work, experiments were performed on different particles size distributions, different materials and different operating conditions. This aimed to understand the influence of each parameter on the charge generation/transfer and to supply the numerical modeling. The experimental setup, designed and built during the PhD thesis, consisted of a 1 m height and 0.1 m inner diameter Plexiglas column. The measuring technique used for charge is a Faraday cup connected to an electrometer. Particles were fluidized for a given time then the air flow was stopped and the gas distributor is opened. Particles falls directly in the Faraday cup and their net charge was measured. Three particle size distributions (PSD) of glass beads and one of ceramic beads were studied for different relative humidity rates and different gas velocities according to an air humidity regulation system. Results shows two categories of particles: dropped particles that falls immediately after opening the valve and wall particles that stick to the wall. The column is taped to make them fall. Each category is measured separately, and the measure is reported to the mass.

The first experiments were performed to determine the minimum fluidization velocity (U_{mf}). Results show no effect of relative humidity on U_{mf}. Comparison to correlation shows that correlation always underestimate the experimental values of U_{mf}.

Next experiments aimed to give access to the kinetics of triboelectrification of the particles according to their physical properties (diameter, density, electrical conductivity) and the operating conditions (velocity and duration of fluidization, humidity of the fluidizing gas). All experiments were performed in bubbling regime. For each time duration, experiments were repeated two or three time to ensure reproducibility. The evolution of the net charge versus fluidization time showed an exponential trend that reached an equilibrium value for both categories (dropped and wall). Wall particles were charged 250 to 450 times than dropped ones. The next step was to investigate the effect of relative humidity, the gas velocity was fixed to a multiple of U_{mf} (minimum fluidization velocity) and various rates of humidity. Results showed that the net charge was decreased by increasing relative humidity for both dropped and wall particles for all PSDs. Small particles of glass beads showed a positive charge whereas all other PSDs were negatively charged. The same behavior for fine particles was highlighted in literature.

After that, the effect of gas velocity on the charge was investigated by fluidizing at different gas velocities and the same relative humidity. The equilibrium charge of dropped particles was not significantly affected. The time needed to reach equilibrium was slightly increased by increasing gas velocity. Wall particles equilibrium charge was significantly increased due to the increasing of the wall-particle collisions frequency and the relative velocity.

On the other hand, the numerical work built an electrostatic model starting from the well-known Maxwell equations, and ending up solving a Poisson equation for the

electric potential. Then the Lorentz force is calculated and added to the momentum balance. Simulations were carried out with a software called NEPTUNE_CFD. It is an unstructured paralleled code (MPI) using unsteady Eulerian multi-fluid approach for dilute and dense particle-laden reactive flows. The walls were assumed to be grounded (zero potential). The boundary condition was also discussed. The model was tested with several test cases, by attribution a prescribed charge for the solid phase. Tests aimed to verify: the resolution of the Poisson equation, the basic laws of electrostatic (attraction and repulsion) and the segregation due to electrostatic charge. After that, a tribocharging model was developed to take into account the charge generation and transfer. The model was inspired from previous works and transposed into an Eulerian approach. It considers a charge per mass unit carried by the solid phase through a transport equation. The diffusive term was derived by analogy with the Kinetic Theory of Gas in another work (Montilla et al. 2019). The wall boundary conditions were developed in this study by performing integrals on the flux of the charge at the wall, by using less restrictive hypothesis. Then, an estimation of the characteristic times of both diffusion and wall charge generation was done. Results shows that the timescale is very high (several days) and does not match with experimental findings (15 to 20 min). A corrective coefficient was proposed to match with experimental results.

Moreover, numerical simulations on a fluidized bed with the same dimensions as the experimental pilot were carried out. In these simulations, the permanent regime was considered, which means after reaching equilibrium charge. The equilibrium charge was prescribed on the particles. Simulations aimed to compare the neutral case where the electrostatic forces were not considered and the charged case. The effect of the charge on the flow properties (solid mass flux, solid distribution, axial and radial mixing and granular temperature) were highlighted. These results pointed out the crucial effect of the electrostatic on the gas-particle fluidized suspension.

Résumé

Les lits fluidisés gaz-solides sont largement utilisés dans les procédés industriels pour l'énergie tels que les boucles chimiques. la combustion, la polymérisation catalytique, la réception solaire, la gazéification de la biomasse, la polymérisation (réacteurs catalytiques en polyéthylène) et la raffinerie de pétrole (craqueurs catalytiques fluides), entre autres. Dans tous ces processus, les forces électrostatiques étaient généralement négligées et leur contribution à l'équilibre des forces était considérée comme un second ordre dans les lits fluidisés gaz-solides. Cependant, les phénomènes de charges électrostatiques représentent un enjeu majeur dans de nombreux procédés industriels dont l'encrassement des parois (accumulation de particules sur les parois), la défluidisation...etc. De plus, ce phénomène pose des problèmes de sécurité : étincelles, explosions de poussière et parfois incendies. A l'échelle moléculaire, le contact entre deux particules (particule-paroi ou particule-particule) génère un transfert d'électrons/ions, induisant une charge sur chaque particule. Par conséquent, le gaz environnant transporte un champ électrique. Ce champ électrique produit une force supplémentaire à l'équation de momentum connue sous le nom de force de Lorentz. Le phénomène électrostatique n'est pas encore bien compris et il existe plusieurs divergences entre les résultats de la littérature. La génération et le transfert de la charge dépendent de nombreux paramètres, y compris les propriétés des matériaux et les conditions de fonctionnement : humidité relative du gaz, vitesse du gaz, pression et température.

Plusieurs travaux littéraires ont étudié l'effet de chaque paramètre que ce soit par des sondes électrostatiques (méthode intrusive) ou par des coupes de Faraday (méthode non intrusive). Cependant, il y a un manque de projets de recherche qui combinent l'étude expérimentale et la modélisation théorique avec la simulation numérique. Ainsi, cette étude s'inscrit dans le contexte, avec un sujet intitulé "Investigation expérimentale et numérique des effets électrostatiques dans les lits fluidisés gaz-solides". Le programme de thèse s'inscrit dans le cadre de la Chaire Attractivité BIREM (BIological, REacting, Multiphase flows) attribuée au Professeur Rodney Fox, soutenue financièrement par l'Université de Toulouse, dans le cadre du programme IDEX. Le projet, hébergé par la fédération de recherche FERMaT, regroupe quatre laboratoires de l'Université de Toulouse dans différents domaines : l'Institut de Mécanique des Fluides de Toulouse (IMFT), le Laboratoire d'Ingénierie des Systèmes Biologiques et des Procédés (LISBP), le Laboratoire de Génie Chimique (LGC) et l'Institut de Mathématiques de Toulouse (IMT).

L'étude vise à combiner les données expérimentales sur les charges électrostatiques dans un projet pilote à l'échelle du laboratoire et la modélisation numérique pour représenter les forces interparticulaires à micro-échelle et à les mettre en œuvre en code CFD par le formalisme d'Euler-Euler à micro-échelle selon la théorie cinétique du milieu granulaire.

Dans ce travail, des expériences ont été réalisées sur différentes distributions granulométriques, différents matériaux et différentes conditions de fonctionnement. Il s'agissait de comprendre l'influence de chaque paramètre sur la génération/transfert de charge et de fournir la modélisation numérique. Le dispositif expérimental, conçu et réalisé lors de la thèse de doctorat, consistait en une colonne en plexiglas de 1

m de hauteur et 0,1 m de diamètre intérieur. La technique de mesure utilisée pour la charge est une coupe de Faraday reliée à un électromètre. Les particules ont été fluidisées pendant un temps donné puis le flux d'air a été arrêté et le distributeur de gaz est ouvert. Les particules tombent directement dans la coupe de Faraday et leur charge nette a été mesurée. Trois distributions granulométriques (PSD) de billes de verre et une de billes de céramique ont été étudiées pour différents taux d'humidité relative et différentes vitesses de gaz selon un système de régulation de l'humidité atmosphérique. Les résultats montrent deux catégories de particules : les particules qui tombent immédiatement après l'ouverture de la valve et les particules de paroi qui collent à la paroi. La colonne est scotchée pour les faire tomber. Chaque catégorie est mesurée séparément et la mesure est rapportée à la masse.

Les premières expériences ont été effectuées pour déterminer la vitesse minimale de fluidisation (U_{mf}). Les résultats ne montrent aucun effet de l'humidité relative sur U_{mf}. La comparaison avec la corrélation montre que la corrélation sous-estime toujours les valeurs expérimentales de U_{mf}.

Les expériences suivantes visaient à donner accès à la cinétique de triboélectrification des particules en fonction de leurs propriétés physiques (diamètre, densité, conductivité électrique) et des conditions de fonctionnement (vitesse et durée de la fluidisation, humidité du gaz fluidisant). A notre connaissance, ce type de résultat n'a jamais été rapporté dans la littérature. Pour chaque durée, les expériences ont été répétées deux ou trois fois pour assurer la reproductibilité. L'évolution de la charge nette en fonction du temps de fluidisation a montré une tendance exponentielle qui a atteint une valeur d'équilibre pour les deux catégories ("dropped" et "wall"). Les particules de paroi ont été chargées de 250 à 450 fois plus que celles qui sont tombées. L'étape suivante consistait à étudier l'effet de l'humidité relative, la vitesse du gaz était fixée à un multiple de U_{mf} (vitesse minimale de fluidisation) et divers taux d'humidité. Les résultats ont montré que la charge nette a été diminuée en augmentant l'humidité relative des particules projetées et des particules de paroi pour tous les PSD. De petites particules de billes de verre présentaient une charge positive alors que toutes les autres PSD étaient chargées négativement. Le même comportement pour les particules fines a été mis en évidence dans la littérature.

Par la suite, l'effet de la vitesse des gaz sur la charge a été étudié par fluidisation à différentes vitesses de gaz et à la même humidité relative. La charge d'équilibre des particules échappées n'a pas été affectée de façon significative. Le temps nécessaire pour atteindre l'équilibre a été légèrement augmenté par l'augmentation de la vitesse du gaz. La charge à l'équilibre des particules de la paroi a été considérablement augmentée en raison de l'augmentation de la fréquence des collisions entre les particules et la paroi et de la vitesse relative.

D'autre part, le travail numérique a construit un modèle électrostatique à partir de la célèbre équation de Maxwell, et a fini par résoudre une équation de Poisson pour le potentiel électrique. Ensuite, la force de Lorentz est calculée et ajoutée à l'équilibre de momentum. Les simulations ont été réalisées avec un logiciel appelé NEPTUNE_CFD. Il s'agit d'un code parallèle non structuré (MPI) utilisant une approche multi-fluide eulérienne instable pour les écoulements réactifs dilués et chargés de particules denses. On a supposé que les murs étaient mis à la terre (potentiel nul). La condition limite a également été discutée. Le modèle a été testé avec plusieurs cas de test, par attribution d'une charge prescrite pour la phase solide. Tests visant à vérifier

: la résolution de l'équation de Poisson, les lois fondamentales de l'électrostatique (attraction et répulsion) et la ségrégation due à la charge électrostatique. Par la suite, un modèle de tribocharge a été développé pour prendre en compte la génération et le transfert de charge. Le modèle s'inspire de travaux antérieurs et se transpose dans une approche eulérienne. Il considère une charge par unité de masse transportée par la phase solide au moyen d'une équation de transport. Le terme diffusif a été dérivé par analogie avec la Théorie cinétique du gaz dans un autre ouvrage (Montilla et al. 2019). Les conditions aux limites du mur ont été développées dans cette étude en effectuant des intégrales sur le flux de la charge au mur, en utilisant des hypothèses moins restrictives. Ensuite, une estimation des temps caractéristiques de diffusion et de génération de charge murale a été faite. Les résultats montrent que l'échelle de temps est très élevée (plusieurs jours) et ne correspond pas aux résultats expérimentaux (15 à 20 min). Un coefficient correcteur a été proposé pour correspondre aux résultats expérimentaux.

De plus, des simulations numériques sur lit fluidisé de mêmes dimensions que le pilote expérimental ont été réalisées. Dans ces simulations, le régime permanent a été considéré, c'est-à-dire après avoir atteint la charge d'équilibre. La charge d'équilibre a été prescrite sur les particules. Les simulations visaient à comparer le cas neutre où les forces électrostatiques n'étaient pas prises en compte et le cas chargé. L'effet de la charge sur les propriétés d'écoulement (flux massique solide, distribution solide, mélange axial et radial, température des granulés) a été mis en évidence. Ces résultats ont mis en évidence l'effet crucial de l'électrostatique sur la suspension fluidisée gaz-particules.

Acknowledgements

I have taken efforts in this work. However, it would not have been possible without the kind support and help of many individuals and organizations. I would like to extend my sincere thanks to all of them.

First of all, thanks God *who gave me power and guidance to complete this work.*

I would like to express my deepest gratitude toward my wife, my mother *and* my parents in law *who have not ceased to encourage me and provide me all support which helped me in completion of this work.*

A tribute goes to my father *who passed away on February 20th, 2017. The person who was dreaming to see me getting this grade. Unfortunately, the death took him away before I accomplish his dream. Yet, he will remain in my heart forever.*

I am highly indebted to Mr. Renaud Ansart *for his constant supervision and day-to-day monitoring as well as providing necessary information regarding this PhD thesis.*

I would like to express my special gratitude and thanks to Mr. Rodney Fox *who managed to share with me a part of his rich experience in numerical modeling despite his busy schedule.*

A special thanks goes to Mr. Olivier Simonin *who contributed to an important part of monitoring even if he was not part of the thesis monitoring committee.*

I would also like to acknowledge with much appreciation the crucial role of the staff of the LGC laboratory, especially Mr. Jack Compain*, who designed the experimental setup and ensured its manufacturing with the collaboration of the laboratory workshop staff.*

Last but not least, many thanks go to all people who contributed directly or indirectly to this work.

Contents

List of Figures

List of Tables

1 Fluidized beds and electrostatic charges

Figures

1.1 Introduction to fluidized beds

1.1.1 Definition and industrial applications

A fluidized bed is a state of a two-phase mixture of particulate solid material and fluid. The condition for a particle to be in suspension is that fluid force of drag and buoyancy balance the force of gravity. This process presents many advantages, including: high surface contact and high relative velocity between particles and gas, high level of intermixing of the solid phase, frequent particle-particle and particle-wall collisions.

Fluidized beds have a wide industrial application, including polymerization, combustion, cracking of hydrocarbons, gasification, synthesis reactions, etc. (see Kunii and Levenspiel 1991). Later, there are some ecological applications like hybrid solar power plants (Li et al. 2019) and biomass gasification (Fotovat et al. 2015).

Generally, there are three distinguishable zones depending on gas velocity (see figure 1.1): the first zone is called fixed bed ($U_f < U_{mf}$) where the pressure drop evolves linearly with gas velocity according to Ergun law in a porous media. The second zone corresponds to the fluidized bed where the pressure drop is constant and equal to bed weight ($U_{mf} < U_f < U_t$). And the third zone is the transported bed where particles begin to leave the bed ($U_f > U_t$). Refer to section 1.1.2 for definitions of U_{mf} and U_t.

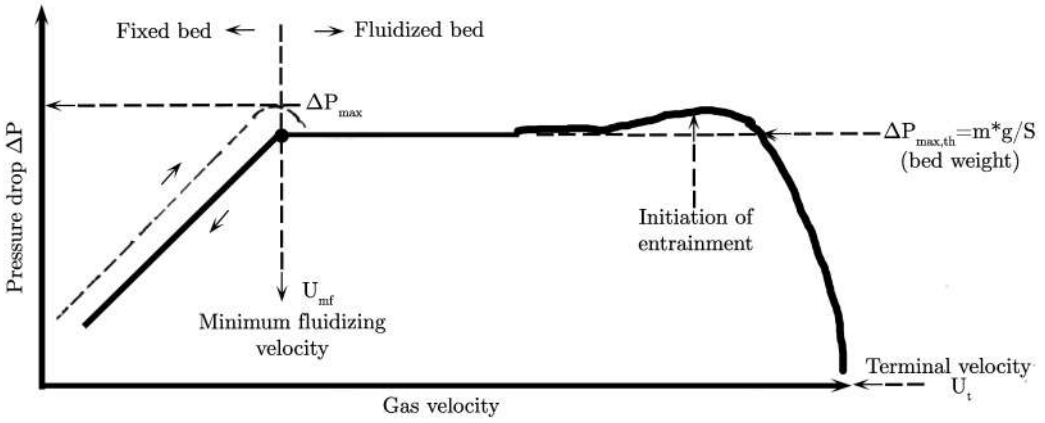

Figure 1.1: Pressure drop versus gas velocity in fluidized bed
(inspired from Kunii and Levenspiel 1991)

There are several types of fluidized bed depending on their uses in industry:

- Bubbling fluidised bed: most common used, where fluidization is performed at low gas velocity and eventually some fine particles are entrained.

- Circulating fluidized beds: like its name says, it is used to make particles circulate in a closed circuit. Entrained particles are re-injected in bed. Depending on the use, a part of particles may be gathered through a cyclone (selective process).

- Transport or conveying beds: gas is injected at higher velocities ($U_f > U_t$) to make particles leave the bed.

- Mechanically Fluidized bed: This technique use an external force to mobilize particles and achieve properties similar to that a well-mixed fluidized bed.

- Narrow fluidized beds: the behavior of this bed is different because bed diameter is about ten time particles diameter.

1.1.2 Characteristic parameters

Minimum fluidization velocity

Minimum fluidization velocity U_{mf} is the gas velocity from which the pressure drop across the bed equals the weight of the bed. It is the parameter on which based any design or operating conditions of a fluidization process. This velocity dependson many parameters, including particles size, shape, density and distribution. It can be estimated based on correlations or experimentally. For example, Wen and Yu 1966 correlation:

$$Re_{mf} = \sqrt{(33.7)^2 + 0.0408 A_r} - 33.7 \tag{1.1}$$

Or Thonglimp et al. 1984 correlation:

$$Re_{mf} = \sqrt{(31.6)^2 + 0.0425 A_r} - 31.6 \tag{1.2}$$

where A_r is Archimedes number:

$$A_r = \frac{\rho_f(\rho_p - \rho_g) d_p^3 g}{\mu_g^2} \tag{1.3}$$

Re_{mf} is Reynold's number at minimum fluidization velocity:

$$Re_{mf} = \alpha_g \frac{\rho_g U_{mf} d_p}{\mu_g} \tag{1.4}$$

α_g, ρ_g and μ_g are volume fraction, density and viscosity of the gas. d_p is particles diameter. The particles diameter can be considered as median diameter of the distribution (d_{50}) or Sauter mean diameter (d_{Sauter}) for a tight particles distribution. It is important to note that these correlation are valid only at ambient pressure and temperature.

Experimentally, U_{mf} is determined trough average pressure drop in the bed. Considering the whole fluidized bed, it is in equilibrium between pressure force, bed weight and walls friction on the bed. According to Vanni et al. 2015, bed walls effect

appears generally in small diameter bed (D$\leq 2cm$). Therefore, if wall friction force is neglected, the pressure drop through the bed is expressed by:

$$\Delta P_{max,th} = \frac{mg}{S} \tag{1.5}$$

Where m is bed mass, g is the gravity and S is the bed cross section. The ratio $\frac{\Delta P}{\Delta P_{max,th}}$ is named fluidization quality index in process field, and it have to be greater than 90% for a good fluidization.

Minimum bubbling velocity

Minimum bubbling velocity U_{mb}, corresponds to bubble appearance in the bed for class A powder in Geldart classification (see subsection 1.1.3). It can be predicted by Abrahamsen and Geldart 1980 correlation:

$$U_{mb} = 33 d_p \left(\frac{\rho_p - \rho_g}{\mu_g} \right)^{0.1} \tag{1.6}$$

Where d_p and ρ_p are particles diameter and density and ρ_g and μ_g are gas density and viscosity.

Terminal settling velocity

The first estimation of this velocity can be considering particles to be separated. For single solid spherical particle in an upward fluid flow, U_t is reached when aerodynamic drag force become greater than its buoyancy (weight of displaced fluid). Its expression using Schiller and Naumann correlation (Clift et al. 1978) for drag coefficient is as follows:

$$U_t = \sqrt{\frac{4 d_p (\rho_p - \rho_g)}{3 \rho_f \frac{24}{Re_{p,t}} \left(1 + 0.15 Re_{p,t}^{0.687}\right)}} \tag{1.7}$$

Where $Re_{p,t} = \frac{\rho_g U_t d_p}{\mu_g}$ is the particulate Reynolds number corresponding to a particle with diameter d_p. ρ_g and μ_g are respectively the gas density and viscosity. This expression is valid for $Re_p \leq 1000$.

Average bed height

In fluidization domaine (between U_{mf} and U_t), the bed height fluctuate around an average value due to bubble eruption at the surface of the bed. Above the minimum fluidization velocity, the sum of drag force and Archimedes force is equal to bed weight if particle friction forces at the wall are neglected. For a control volume of the suspension with a given cross section S and height z, considering that drag force is composed only from pressure force, the force balance is expressed as:

$$PS + \alpha_p \rho_g S z g = \alpha_p \rho_p S z g \tag{1.8}$$

Where P is the pressure load, z is the height and g is the gravity. α_p and ρ_p are volume fraction and density of the particles respectively. Thus, for an infinitesimal

variation dz of height, equation 1.8 can be expressed by pressure gradient through the bed:

$$\frac{dP}{dz} = \alpha_p(\rho_p - \rho_g)g \tag{1.9}$$

Based on this assumption, the pressure gradient in the bed is constant in bubbling regime since α_p is constant. Practically, the pressure profile is plot versus height at different location in the bed using pressure sensors.

Bubble frequency

Bubble frequency gives an idea about fluidization regimes. Experimentally, pressure fluctuations around an average value with sufficient sampling frequency gives an idea on bubble frequencies. Pressure fluctuations are analysed trough the normalized standard deviation (He et al. 2014) or Fast Fourrier Trasform spectrum (Felipe and Rocha 2004). Although most authors perform analysis in the plenum (before the distributor) based on bed beats frequency, He et al. 2014 found that it is is not representative because fluctuations are extenuated. The spectrum analysis can also indicate the transition between fluidization regimes.

1.1.3 Geldart classification

Based on published literature and experimental work, Geldart 1973 classified materials according to their behavior in fluidized bed to four groups described as below:

Group C: known also as cohesive powder. For this type, the gas passes up voids extending from distributor to bed surface, this phenomena is called "channeling". "Normal" fluidization of this type of powder is extremely difficult, this difficulty is due to the fact that inter-particle forces are greater than those exerted by the fluid on the particle. These forces are generally resulting from the very small particle size (Van Der Waals forces), strong electrostatic charges or the presence of very wet or sticky material in the bed. Fluidization can generally be performed or improved by the use of vibrators to break up the stable channel or humidification of incoming gas.

Group A: contains materials with small mean size and/or low particle density, like some cracking catalysts. Bubbles appear when the superficial gas velocity reaches a critical value U_{mb} called minimum bubbling velocity. For this type, the fluidization pass through a smooth regime before reaching bubbling regime. It is the only type of particles for which $U_{mb} > U_{mf}$. When the superficial gas velocity is sufficiently high to cause the formation of slugging conditions, the produced slugs are axi-symmetric: as the superficial gas increased slug flow breaks down into a turbulent regime.

Group B: known also as sand-like materials. Opposing to group A, bubbles formation in this group occurs at or only above U_{mf}. Bed collapses very rapidly after cutting off gas supply. In the absence of bubbles, there is little or no powder circulation. Most bubbles rise more quickly than the interstitial gas; coalescence is predominant. Both back-mixing of dense phase gas and the exchange between bubbles and dense phase are relatively low. When the superficial gas velocity is high and slugging begins, slugs are initially axi-symmetric, but as gas velocity increases an increasing proportion become asymmetric.

Group D: this group includes powder with large and/or very dense particles. Largest bubbles rise more slowly than the interstitial gas so that gas flows into the base of the bubble and out of the top, providing a mode of gas exchange and by-passing different from that observed with group A or B powders. The gas velocity in the dense phase is high, solids mixing relatively poor; consequently back-mixing of the dense phase gas is small. The flow regime around particles in this group may be turbulent, causing some particle attrition with rapid elutriation of the fines produced.

Geldart determined boundaries between these groups by plotting particle-fluid density difference against particle diameter. It is worthy to note that Geldart 1973 classification employed fluidization data obtained only at ambient temperature and pressure and from beds fluidized only with air. At elevated pressure and temperature, this classification was modified by Yang 2007 and re-interpreted by plotting a dimensionless density $\frac{\rho_p - \rho_g}{\rho_g}$ against the Archimedes number $\frac{\rho_g(\rho_p - \rho_g)d_p^3 g}{\mu_g^2}$ (cf. figure 1.2).

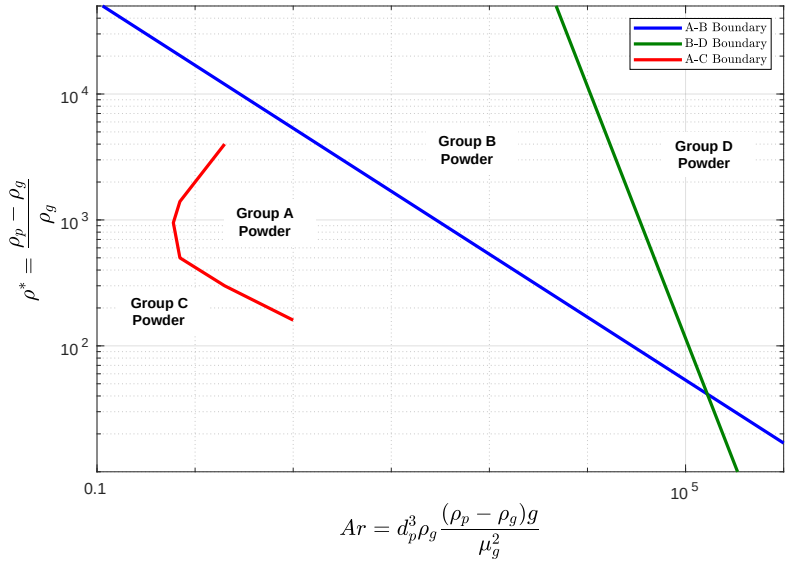

Figure 1.2: Geldart classification modified by Yang 2007

1.1.4 Fluidization regimes

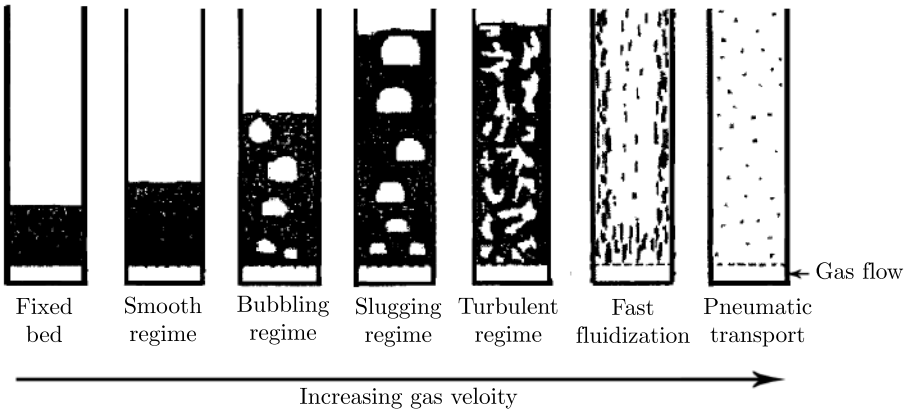

Figure 1.3: Fluidized bed preview for different fluidization regimes (Modified from: Crowe and Mechaelides 2006)

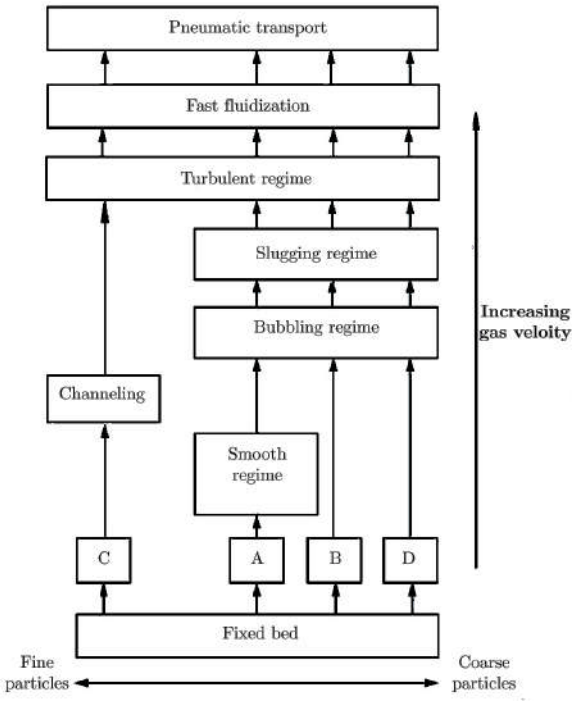

Figure 1.4: Fluidization regimes for Geldart's classification (inspired from: Antonini 2008)

Fluidization regimes can be classified on the basis of gas velocity. Figure 1.3 illustrates the fluidized bed preview for different regimes. Following ascending order, figure 1.4 shows different fluidization regimes for Geldart classification:

Smooth regime: this regime appears only for group A. As described before, an homogeneous expansion of the bed is observed before attaining bubbling regime.

Bubbling regime: the bubbles form at superficial gas velocities only slightly higher than that required to just fluidize the particles. Under these conditions, the bed appears to be divided into two phases, the bubble phase and the emulsion phase (the remainder of the bed). The bubbles coalesce as they rise through the bed.

Slugging regime: it is defined as the regime when formed bubbles diameter is comparable to the bed diameter. This happens at increasing gas velocity when bubble coalescence is predominant. It occurs only in beds with bed height H over bed diameter ratio D larger than about 2 (Stewart and Davidson 1967).

Turbulent regime: at increasing gas velocity, the regime evolves and as bubbles splitting at the bed free-board become dominant, the regime become turbulent. The transition is gradual. It can be characterized by two velocities: U_c, the velocity at which the pressure fluctuations peak, and U_k, the velocity at which the pressure fluctuations, having decayed from their peak value, begin to level off. U_k marks the onset of the turbulent regime (Yerushalmi and Cankurt 1979).

Fast fluidization regime: increasing gas velocity leads to a fast fluidization regime. This regime is used in circulating fluidized beds in which the particles transport is important. According to Yerushalmi and Cankurt 1979, a critical solid circulation rate may exist where a sharp change in the pressure gradient occurs when the solids circulation rate is varied at a given gas velocity in the riser of a circulating fluidized bed.

Pneumatic transport: further increasing gas velocity leads to a pneumatic transport characterized by critical velocity U_{CA} named accumulative choking velocity. It sets the minimum superficial gas velocity required to make a given flux of solid particles fully suspended in the whole transport line without accumulation. U_{CA} is related to the solids elutriation rate from the top of the bed (Bi et al. 1993).

1.1.5 Numerical modeling of fluidized beds

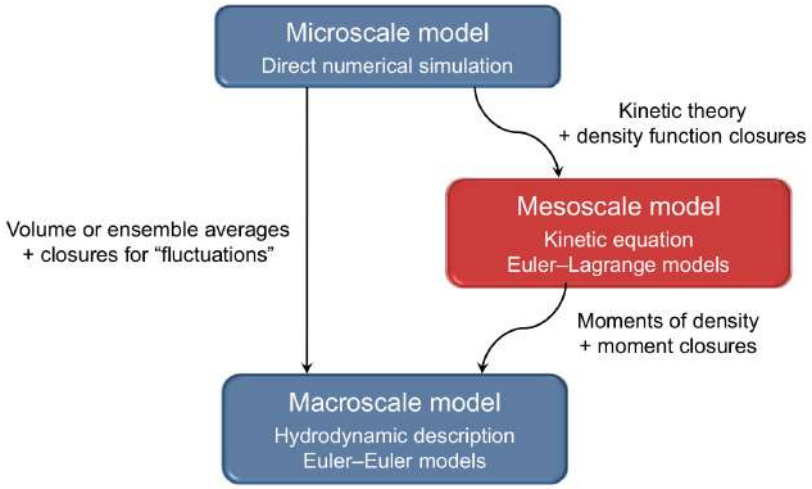

Figure 1.5: Different multi-fluid modeling approaches depending on the application scale (Fox 2018)

Depending on the requirements of each utilization, different approaches were developed to understand and predict the transportation of particles and drops by a fluid phase:

Direct Numerical Simulation

In this approach, the Navier-Stokes equations are solved around each inclusion, and the grid has to be adaptive to follow the movement of the particles. This approach requires minimal hypothesis and models the exact interactions between the fluid and the particles (Wachmann and Schwarzer 1998; Thiam et al.2019). Despite the increase of the means of calculation, the Direct Numerical Simulation is limited to a small number of particles and usually used to understand phenomenon at a micro-scale. It cannot be applied to a fluidized bed where the interaction of millions of particles with the fluid must be predicted.

Eulerian-Lagrangian approach

Know also as Discrete Element Modelling (DEM), it involves Eulerian modeling of fluid or gas phase and Lagrangian tracking of discrete particles (Dufresne et al. 2016). The Lagrangian formulation gives an accurate description of the motion of a single particle. However, computational cost of DEM numerical simulations is high because the resolution is performed for millions of particles and it is not feasible neither on the industrial nor the lab scale.

Eulerian-Eulerian approach

In this approach, all phases are modeled as inter-penetrating continuum media. In Euler-Euler approach, a statistical procedure is followed to derive basic continuum balance equations from the local instantaneous equations for each phase in a suitable way, in space, on time or ensemble. The averaging procedure introduces unknowns and thus, closure relations are necessary. These relations describe interactions between phases and physical properties of phases. The relations related to physical

properties of gas phase are defined as a single phase flow. Empirical models and the Kinetic Theory of Granular Flow (KTGF) are used for the physical properties of particulate phases such as; granular pressure, dynamic and bulk viscosity. Because of the lack of universality of empirical models, the majority of Euler-Euler studies are performed by KTGF. The first works focused on rapid dry granular flows. Jenkins and Savage 1983; Jenkins and Richman 1985 derived the momentum and granular temperature transport equations in the framework of the kinetic theory. They also provided a closed form for the collision term of the Boltzmann equation. Ding and Gidaspow 1990 extended the previous work to fluid-particle configurations. They added the influence of the drag force into the transport equations. Their work showed the modification needed in the transport laws to account for the fluid-particle interactions. After that, Simonin 1991 and Boelle et al. 1995 focused their analysis in the interaction between the particles and the surrounding fluid flow. The Eulerian approach has proven to be very useful in the last years, because of its capabilities of addressing industrial configurations where the high number of particles makes the particle-tracking methods unsuitable or unfeasible (Hamidouche et al. 2018).

1.2 Electrostatic charges in gas-solid fluidized beds

Electrostatic forces were usually neglected and their contribution to force balance considered as a second order in gas-solid fluidized beds. However, the phenomena of electrostatic charges presents a major issue in many industrial processes including wall fouling (particle accumulation on the walls), defluidization...etc. Moreover, this phenomena presents security issues: sparks, dust explosions and sometimes fires. As a results, the surrounding gas carries an electric field. This electric field results in an additional force to the momentum equation. Hendrickson 2006 reviewed electrostatic effects in polymerization fluidized-bed reactors and the causes of reactor fouling, explained the charge distribution in fluidized beds, causes of bipolar charging, electrostatic charge generation and dissipation mechanisms, and compared the effect of electrostatic forces with other forces like drag and, gravity on particle entrainment. This section presents an overview on the literature concerning electrostatic measuring techniques, effects on hydrodynamics, effects of operating conditions and numerical modeling of electrostatic charges.

1.2.1 Electrostatic charge measuring techniques

Numerous methods for measuring electrostatic charges within a fluidization column have been proposed in literature. Measuring methods can be split into intrusive and non intrusive method:

Intrusive method

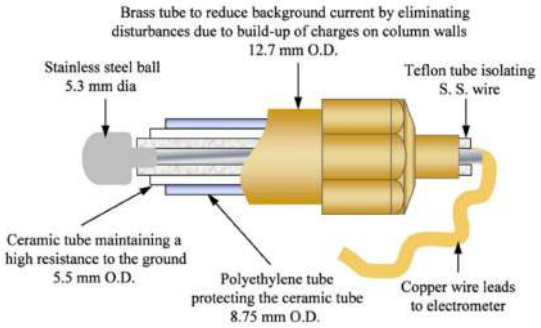

Figure 1.6: Schematic diagram of electrostatic collision ball probe (Moughrabiah et al. 2012)

The intrusive method consist of electrostatic collision ball probes. This method was used by many authors (Yao et al. 2002; Park et al. 2002b; Moughrabiah et al. 2008; Moughrabiah et al. 2012). Figure 1.6 shows a schematic description of this probe presented by Moughrabiah et al. 2012. It is composed of a glass sleeve maintaining a high resistance to the ground and a brass tube enclosing the glass tube reduced the background current by eliminating disturbances due to buildup of charges on the column walls. This method provides a direct electrostatic charge measurements, this allows to map charge distribution through the bed. However, the intrusive character of the method puts into question the extent of the influence of the probe on the local behavior of the particles near the wall.

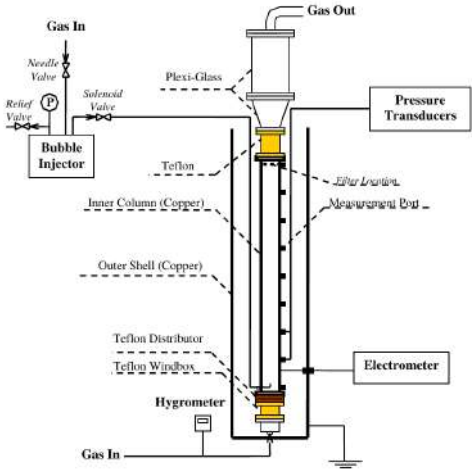

Figure 1.7: Schematic diagram of Mehrani et al. 2005 experimental setup

Non intrusive method

The non intrusive approach is based on a device known as Fraday cup. It consists of a cup made from conductive material and related to an electrometer. It provides the bulk charge of the a sample rather than a local measurement. Mehrani et al. 2005 developed an on-line measurement technique by applying the Faraday cup method to study the mechanism of charge generation inside gas-solid fluidized beds. The experimental setup is presented in Figure 1.7. The fluidization column consisted of two concentric vessels. The outer copper shell is grounded to eliminate external electrical interference. The inner column, consists of three sections of different materials. The middle section is made of copper connected at both ends with Teflon sections, Teflon being a poor electrical conductor. The top expanded section is made of Plexiglas. The middle copper section of the fluidization column is connected directly to an electrometer. Tests confirmed that the system was functioning properly as a Faraday cup.

Sowinski et al. 2009 proposed a new method of measuring electrostatic charges based on the Farday cup technique. The new method consists of a Faraday cup placed within the wind-box of a fluidization column. The distributor plate was designed in such a way that it can be automatically opened to drop the charged fluidizing particles into the Faraday cup below. An electrometer is connected to the cup to measure the total net electrostatic charge of dropped particles. The technique was proven to be suitable for measuring the total net electrostatic charges of particles in gas-solid fluidized beds. However, the total net electrostatic charges does not give an idea about charge distribution in bed and polarity.

In order to detect charge distribution, Faraday cup measurement technique mentioned above was customized by Salama et al. 2013. Figure 1.9 shows the apparatus which consisted of two copper plates situated in an angle above four Faraday cups. It plays a role of particle charge separator. A high voltage power supply was used to positively charge one of the plates up to 40 kV, whereas the other plate was grounded to act as a negatively charged plate. Four Faraday cup were placed under the separator apparatus and dropped particles were separated according to their polarity and charge magnitude.

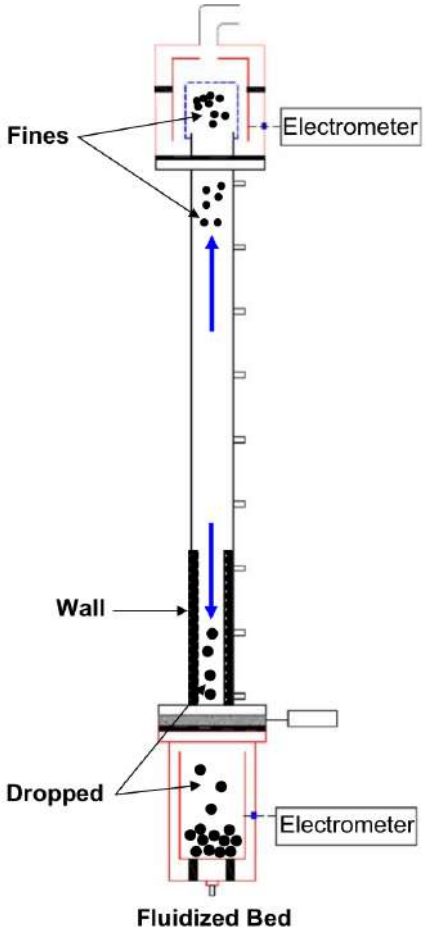

Figure 1.8: Schematic diagram of the new Faraday cup measurement technique presented by Sowinski et al. 2009

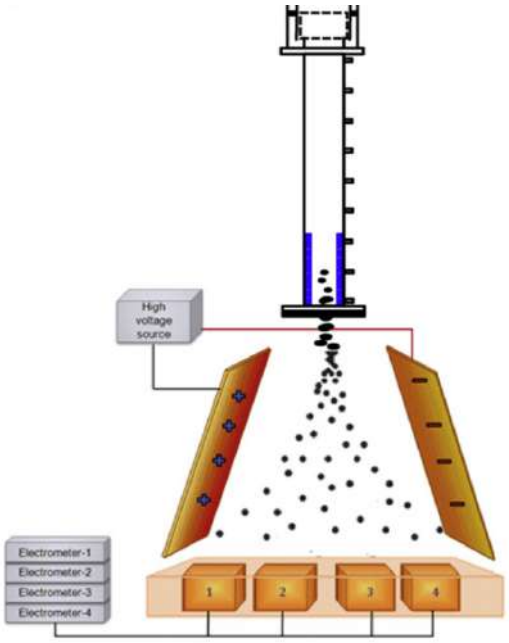

Figure 1.9: Electrostatic charge separator presented by Salama et al. 2013

Fotovat et al. 2016 measured electrostatic charges of entrained particles in a fluidized bed with a novel sampling device incorporating the Faraday cup principle (see Figure 1.10). It consists of two copper inverted cones, electrically insulated from each other. The degree of electrification of entrained particles was characterized by measuring the electrical charge induced from entrained fine particles which entered the internal inverted copper cone.

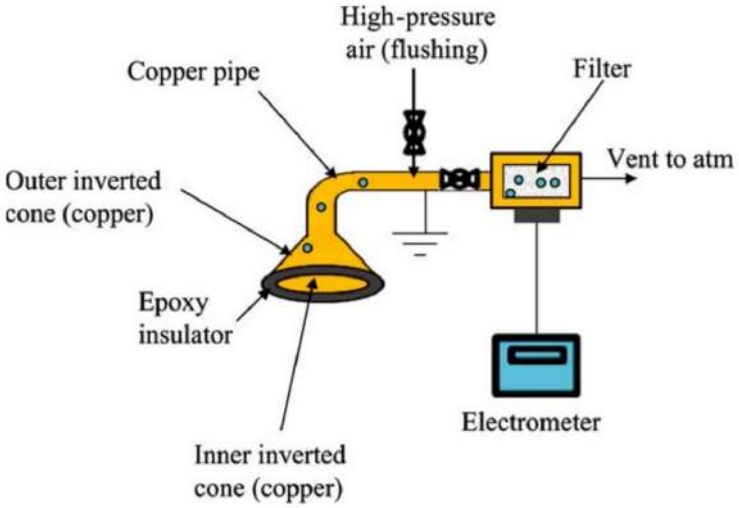

Figure 1.10: Sampling device of Fotovat et al. 2016

1.2.2 Effects of electrostatic charges on bed hydrodynamics

Effects on bubble motion

The influence of electrostatic charges on bubble interactions is an important issue. pair-wise bubble interaction and coalescence play key roles in determining not only the distribution of bubble size, but also overall bed properties. They also strongly influence how much gas rises as bubbles and passes through bubbles in the bubbling regime of gas-fluidized beds.

Park et al. 2002b studied glass beads and polyethylene fluidization by injecting bubbles into two- and three-dimensional fluidized beds. Both glass beads and they found that larger bubbles resulted in higher induction and transfer of electrostatic charges.

The effect of electrostatics on interaction of bubbles by simulating pairs of bubbles in vertical and horizontal alignment in uncharged and charged particles was investigated by Jalalinejad et al. 2015. The simulations used a two fluid model from the works of Jalalinejad et al. 2012. They compared results to experimental work of Clift and Grace 1970, for bubbles in vertical alignment. The model predicts the overall coalescence pattern, but the trailing bubble splits in simulations, unlike experiment. Comparison of uncharged and charged cases for bubbles in vertical alignment shows different bubble coalescence behavior, with greater asymmetry in the charged case, leading to larger resultant bubble. For bubbles in horizontal alignment, electric charges cause the side bubble to migrate towards the axis of the column, reversing the leading-trailing role of the two bubbles, which led to the decrease in the height of complete coalescence.

Later, Tan et al. 2018 performed experiments of bubble injection in a two dimensional fluidization bed and record bubble rises with a high speed camera. Experiments were compared to numerical simulation using Two Fluid Model coupled with electrostatic model (similar to Rokkam et al. 2010). The electrostatic force tends to push the particles at the left and right edges of the bubble outward towards the emulsion phase region, which leads to the elongation of bubble in the horizontal direction. The electrostatics also causes the particles in the middle region of the fluidized bed to have the tendency to move around, resulting in more gas accumulating from the emulsion phase to the bubble region.

Effects on particles entrainment

The particles entrainment in fluidized beds is highly influenced by electrostatic charges. Its effect is also not well understood and there is some discrepancies in literature. Baron et al. 1987 studied the effect of electrostatics on entrainment in gas-solid fluidized bed using silica sand. They found that particle entrainment was increased when the fluidizing gas humidity was increased. The gas humidity did not affect the fluidized bed behavior: the bed expansion and the flux of particles ejected from the bed surface were not affected. They attributed the increase in particle entrainment, as the humidity was increased, to a reduction of electrostatic effects. Briens et al. 1992 conducted experiments with solids ranging from 69 μm cracking catalyst to 400 μm polyethylene. Results showed that the smallest particles were not the most easily elutriated from fluidized beds of mixed size particles. Therefore, the

smallest particles cannot be removed by elutriation from a mixture of particles of various sizes. Electrostatic forces were, thus, not responsible for particle agglomeration. Electrostatic effects, on the other hand, greatly reduced the flux of elutriated particles by creating an extra electrostatic pressure drop in the fluidized bed free-board. They also changed the fluidization quality of the bed of polyethylene particles.

Elsewhere, some authors studied the behavior of binary mixture regarding entrainment by combining fine and coarse particles. Wolny and Opaliǹski 1983 studied fluidization of washed and dried polystyrene beads. Authors observed that the particles electrically charged cling together in large aggregates and adhere to the heating walls of the apparatus. However, this effect is neutralized by adding a small proportion of fines. They found that these phenomena are independent of the electric nature of the added fine material (conductor, semiconductor or dielectric). The author explained the mechanism of electric charge neutralization by the addition of fines: the fines change the contact conditions between particles of the bed, and transfer electric charge between particles, causing neutralization of the whole bed. Yet, Mehrani et al. 2007 found that adding fines to an initially charged fluidized bed carry significant, but different amounts of charges out of the column depending on gas and solid properties and therefore leaving a net charge behind.

On the other Fotovat et al. 2016 conducted experiments on binary mixture of glass beads and fine particles of different materials to see the influence of electrostatic particles on entrainment flow. An empirical correlation of Choi et al. 1999 was modified to incorporate a term for inter-particle electrostatic force to fit with experimental results. These results show that it is essential to consider electrostatic forces when predicting entrainment of fines from many gas-solid fluidized beds.

Further studies were conducted by Fotovat et al. 2017 on conductive and non-conductive fine powders. Entrainment of the conductive particles was markedly higher than for non-conductive species. This observation was attributed to the intensification of electrostatic inter-particle forces for non-conductive particles due to the non-uniform electrical charge distribution over their surfaces. Moreover, dominance of the attractive forces among the dielectric particles is likely in the free-board region, promoting formation of aggregates or clusters which reduces entrainment. Conversely, repulsive electrostatic forces between pairs of touching conductive particles causes these particles to act independently, augmenting their entrainment. Thus, using particles with decreased electrical conductivity can reduce significantly entrainment of fine particles in fluidized bed.

Effects on solid distribution - Wall fouling

With polyolefin production, electrostatic charge generation can cause the formation of larger granules, as well as reactor wall fouling (formation of layers of the particles on the reactor wall). These large agglomerations can fall and clog the distributor plate, as well as stick to the reactor wall. These disruptions cause considerable operational down time as the reactor requires proper cleaning before it can be put back on-line. Sowinski et al. 2012 studied the effect of particle size of a polyethylene resin received directly from industrial reactors on electrostatic charge generation and reactor wall fouling using a Faraday cup. The resin was sieved into five different narrowed particle size fractions and fluidized at two different gas velocities representing the bubbling and the slugging flow regimes. In the bubbling flow regime

very little reactor wall fouling was observed whereas in the slugging flow regime significant particle-wall adhesion and in other times none was obtained. Overall, it was found that the smaller particles had a higher charge and resulted in more reactor wall fouling. This study found that the measurement of the net charge-to-mass ratio inside a fluidized bed is not an indication of the amount of reactor wall fouling.

Giffin and Mehrani 2013 studied the the effect of the presence of moisture on wall fouling using for polyethylene resins for two fluidization regimes: the effect was only apparent in the bubbling flow regime and at high relative humidities of 60% and 80% where fewer particles adhered to the column wall. In the slugging flow regime, no significant and consistent decrease in particle layer was observed. Neither flow regime demonstrated a clear trend in m% with the increase in relative humidity in the bulk region. Note that the results were due to the hydrophobicity of polyethylene and the use of stainless steel column.

Charge distribution and bi-polar charging

Measuring the net charge does not give an idea about charge distribution in bed. Many authors tried to measure the charge distribution, Zhao et al. 2000 studied bipolar charging using polymer powder using a vertical array of seven Faraday pail sensors. This technique gives charge distribution in the bed upon particle size (gravity segregation) and charge (space charge repulsion). Results showed that even though the net charge may be positive or negative the fine particles show a negative charge and the coarse particles positive. Mehrani et al. 2007 found that the relatively large glass beads and polyethylene particles were charged negatively, whereas the entrained fines were charged positively. Moughrabiah et al. 2008 also found that, at higher gas velocities, the polarity in the free-board region was opposite to that in the bed. Sowinski et al. 2010 found the occurrence of bi-polar charging in bubbling and slugging flow regimes of large polyethylene distribution fluidization. Entrained fines being mainly positively charged, whereas the bed particles and those attached to the column wall carrying a net negative charge. The same results were found in simulations of Rokkam et al. 2013.

Later, Salama et al. 2013 investigated the distribution of charge within the wall fouling region and bulk of a fluidized bed reactor using Faraday cup measurement technique mentioned above. The wall particles were found to be predominantly negatively charged while those which did not adhere to the wall were predominantly positively charged. The charge distribution within each region was investigated by the system illustrated in figure 1.9. It was determined that although the net charge of the wall layer particles was negative, a significant amount of positively charged particles existed within each sample and therefore the entire wall particle layer. This suggests that the wall layer was formed through layering between positively and negatively charged particles. Particles in the bulk of the bed also consisted of bipolarity charged particles. Besides, Moughrabiah et al. 2012 observed bipolar charging in experiments where polyethylene resin particles constituted the bed materials, with large particles charging negatively, and fine particles positively. The same effect was observed by Giffin and Mehrani 2013.

1.2.3 Effects of operating conditions on electrostatic charges

The electrostatic effect in fluidized beds depends on many parameters, including the relative humidity and velocity of fluidizing gas and operating temperature and pressure. This section presents an overview on the findings in literature about these effects.

Effect of relative humidity

The relative humidity make significant changes in fluidized bed behavior. Guardiola et al. 1996 found that the effect of relative humidity is connected with the quality of fluidization- bubbling or slugging - existing in the bed. He elaborated a characteristic curve for electrification versus humidity that consists of five zones. Yao et al. 2002 found that increasing relative humidity at a given gas velocity, induced a decrease in both standard deviation of the voltage signals and the differential pressure fluctuations, indicating that the charge buildup in the vicinity of the bubble decreased as the bubble size decreased. Park et al. 2002b investigated reduction of electrostatic charge accumulation by increasing the humidity of fluidizing gas using single bubble injection in two- and three-dimensional fluidized beds. Increasing the relative humidity between about 40% and 80% reduced the electrostatic charge accumulation by increasing the surface conductivity, thereby enhancing charge dissipation. However, over-humidification led to excessive capillary forces causing defluidization. Note that all these works used hydrophilic material.

1.2.4 Numerical modeling of electrostatic charges

There was many models proposed in literature for electrostatic charge in gas-solid fluidized bed. Two models are picked up depending on the approach used for modeling: Rokkam et al. 2010 developed an electrostatic model based on basic laws describing electromagnetic phenomena within an Eulerian approach. These laws originate from the well-known Maxwell equations and Lorentz force equation. The electrostatic model was coupled with a multi-fluid computational fluid dynamic (CFD) model to understand the effect of electrostatics on the bulk polymer, polymer fines, and catalyst particles. Rokkam et al. 2013 used the model presented by Rokkam et al. 2010 to simulate the experiments conducted by Sowinski et al. 2010 in a 2D geometry with the same dimensions of experimental setup. Particle-phase segregation from CFD simulations with electrostatic forces compared well with experimental measurements and observations. Jalalinejad et al. 2012 presented an electrostatic model with two-fluid CFD model. The electrostatic force density was derived from Melcher 1981 work, who estimated this force density of dielectric material where there is a combined effect of free charge and polarization. They also investigated the sensitivity of the results to frictional models.

On the other hand, Kolehmainen et al. 2016 presented an hybrid approach to determine the electrostatic force, by combining Eulerian and Lagrangian approach. The electric field is the sum of: long-range contribution (Eulerian approach) to the electric field by solving the Poisson equation, short-range contribution (Lagrangian approach) through truncated pairwise sum and added a correction to avoid double counting.

1.2.5 Charge generation - tribocharging

Charge generation is a phenomenon occurring due to particle-particle and wall-particle contact. It induces a modification of the charges carried on particles. This contact is known as triboelectric charging or tribocharging. This phenomenon is generally considered undesirable in fluidized bed reactors and pneumatic conveying devices.

In order to complete the electrostatic models mentioned above, some authors proposed some models to take into account the phenomenon. Lindell et al. 1993 formulated a static image theory for an homogeneous dielectric sphere was recently to account for the reaction of the sphere to the field from any electrostatic charge distribution. Matsuyama and Yamamoto 1995 proposed a model for a mechanism dominating the charge generated on a particle due to impact or contact with metal plate. In this model, the impact/contact charging of a particle is determined as the remaining charge by the charge relaxation process due to gaseous discharge in atmospheric conditions. Another model based on probability density functions is presented by Matsusaka et al. 2002. Author considered three functions: the number of collisions of a particle with the wall ($f_1(q_m)$), initial particle charge ($f_2(q_m)$), and the impact electrification factor characterizing the transferred charge ($f_3(q_m)$). These functions individually affect the electrostatic charge distribution, and hence key parameters on the particle electrification can be determined from the charge distribution. Park et al. 2002 developed a mechanistic model for electrostatic charge transfer to a spherical probe due to passage of bubbles in a fluidized bed by applying the method of images. The bubble is assumed to be perfectly circular with its charge distributed

uniformly at its surface, while charge decay is assumed to be instantaneous. The model predicted that when a bubble with positively charged surface approaches the probe, a positive voltage is first induced with its maximum corresponding to the instant when the bubble nose reaches the centre of the probe. The voltage output starts to decrease and switches to negative when the bubble centre passes the probe, with a negative peak when the bubble wake reaches the probe. Charge transfer occurs when particles propelled by the bubble contact the probe. Later, Matsusaka et al. 2010 reviewed the basic concepts and theories of charge transfer between solid surfaces in literature, and described chemical factors depending on materials and environmental effects. They also analyzed the process of particle charging, and presented relevant models.

On the other hand, some authors proposed models based on surface state theory (Ali et al. 1998, Laurentie et al. 2013). This theory is presented in details in literature by Schein et al. 1992. It expresses, in the high density limit, the charge exchanged per unit between two insulating surfaces. The models links the charge σ_{ij} exchanged per unit area during the collision process between two particles i and j with surface work functions ϕ_i and ϕ_j needed to extract an electron from their surfaces. It also depends on some physical properties of the materials in contact. Kolehmainen et al. 2016b built electrostatic model presented in the previous work (Kolehmainen et al. 2016) and the triboelectric charging model of Laurentie et al. 2013 into a CFD-DEM model.

Recent work of Kolehmainen et al. 2018 proposed a more complex model. They derived a transport equation for the mean particle charge using the kinetic theory of granular flow. Assuming an uncorrelated Maxwellian (or Gaussian) probability density distributions for the velocity and the particle charge, they were able to close the collision integral and Eulerian modeling of mono-dispersed gas-particle flow with electrostatic forces to derive an electric charge collisional dispersion coefficient. However, this coefficient was not enough to account for all the particle electric charge dispersion, and therefore, they decided to add a kinetic dispersion coefficient following an analogy with the heat transfer coefficient (Hsiau and Hunt 1993). Author performed DEM simulations and validated this new formulation.

More recently, Ray et al. 2019 extended that model and computed the charge-velocity correlation in order to derive the kinetic dispersion coefficient. The authors were also able to derive the charge variance equation in order to fully close the mean charge transport equation. They implemented their model using OpenFOAM and simulated a two-dimensional fluidized bed. The results showed that they were able to successfully predict the thickness of the particle layer formed at the wall of the reactor. It is worth noting that these previous studies has been conducted with the assumption that the Coulomb's force does not modify the dynamic of the particle-particle encounters. Although, this hypothesis holds for rapid granular flows, it might be too restrictive for configurations where the electric potential energy is comparable to the kinetic energy.

Montilla et al. 2019 derived an Eulerian model for the electric charge in a gas-particle flow using the framework provided by the kinetic theory of granular flows. Authors elaborated a transport equation for mean electric charge and closed the model by a charge-velocity correlation transport equation. They used less restrictive hypotheses than previous work (Kolehmainen et al. 2018; Ray et al. 2019). The model was tested on a 3D periodic box (same as Kolehmainen et al. 2018). It was

found that the collisional dispersion coefficient is predominant in dense regimes and that the kinetic dispersion coefficient is the most important in dilute configurations. There is, nevertheless, an intermediary region where both coefficient have to taken into account in order to accurately predict the dispersion effect. For dense regimes, the triboconductivity and the dispersion are of the same order of magnitude if the characteristic dispersion length is comparable to the particle diameter. This model will be detailed in Chapter 3, section 3.3.3.

1.3 Thesis outline

To our knowledge, this thesis is the only study that combines the experimental and numerical work performed in the same lab by the same team. The experimental work aimed to get an accurate database depending on the progress of numerical modeling. An experimental setup was built during this PhD thesis, consisting of a 1 m height and 0.1 inned diameter Plexiglas column, a sintered metal distributor plate related to an actuator and a Faraday cup related to an electrometer. The setup was supplied by an air humidity controlling system. Four particles size distribution were investigated and their net charge and mass was measured depending on the gas relative humidity and velocity and fluidizing time. On the numerical side, a theoretical model based on Maxwell equation for electromagnetic field was inspired from an existing model. The model was implemented in a simulation software using the Eulerian-Eulerian approach and the full coupling with the multi-fluid model was verified. Besides, a tribocharging model is developed to take into account the charge generation due to collisions. The model was inspired from existing Lagrangian model, but transposed to an Eulerian approach. The main experimental results are presented and numerical simulations were run based on these results to highlight the effect of electrostatic charges on the bed hydrodynamics. This work outline is as follows:

Chapter 1 presented a general definition of gas-solid fluidized beds, some characteristic parameters and experimental techniques used for electrostatic charge measuring. Then, it discusses the finding in literature about electrostatic charge effects on bed hydrodynamics, including bubbles motion, entrainment flux and solid distribution. After that, a bibliography mapping about effects of operating conditions on electrostatics is performed (gas relative humidity, velocity, pressure and temperature and materials properties). Finally, it gives the numerical models proposed in literature to model electrostatic phenomenon.

Chapter 2 shows the experimental setup used in this study including fluidization column, humidity controller, Faraday cups and measuring devices. Then, it presents powder characterization devices and materials used in experiments. And ends up describing experiments procedure.

Chapter 3 introduces the Eulerian-Eulerian approach used in numerical simulations with mathematical models and closure laws. After that, an electrostatic model is elaborated combined with a tribocharging model. Lastly, some verification test cases are presented.

Chapter 4 describes experimental results obtained for different materials, discusses the effects of operating conditions on electrostatic charge and its effects on bed behavior and then draw some conclusions.

Chapter 5 presents the numerical simulations of tribocharging model in order to transcribe the charge evolution versus time of the bed observed in experiments. The second part presents a comparison between a non charged and charged bed to highlight the effect of electrostatic charge on bed hydrodynamics.

2 Experiments description

Figures

Tables

2.1 Experimental setup

Experiments are performed on a laboratory scale pilot of 0.1 m inner diameter and 1 m height Plexiglas column. Figure 2.1 illustrates the setup. A schematic design is presented in figure 2.2 with more details. This setup was conceived and manufactured during this thesis PhD in the workshop of LGC (Laboratoire de Génie Chimique de Toulouse) under the supervision of Jack Compain. Pressure taps are set through the column height at each 3 cm for the first 30 cm. Then at each 10 cm. For the first three pressure taps, additional radial taps are added at 90° at each tap to make sure there is no bypass of bubbles during fluidization. A micro grid is placed at every tap to avoid particles migration to pressure sensors. Fluidizing gas used in all experiments is air.

Figure 2.1: Experimental setup

It is important to note that the whole setup was made from Plexiglas except two parts: the distributor and a part of the supporting piece overhead the distributor. In this part, there is two Plexiglas pieces sandwiching the distributor plate. And right overhead, there is a metal piece of 3 cm height placed on the chassis. This piece is meant to bear the weight of the column and ensure a vertical position. In order to avoid a different behavior of the powder in this area, a film of PMMA is stuck on the inner surface. All the inner bottom block was sprayed with a dielectric insulator (10 kV/mm). All these modifications are meant to maintain the same effect of the walls on the particles.

2.1.1 Gas flow distributor

Gas flow distributor is made of sintered metal to ensure a good fluidization quality and to prevent small particles from falling during fluidization. This distributor was

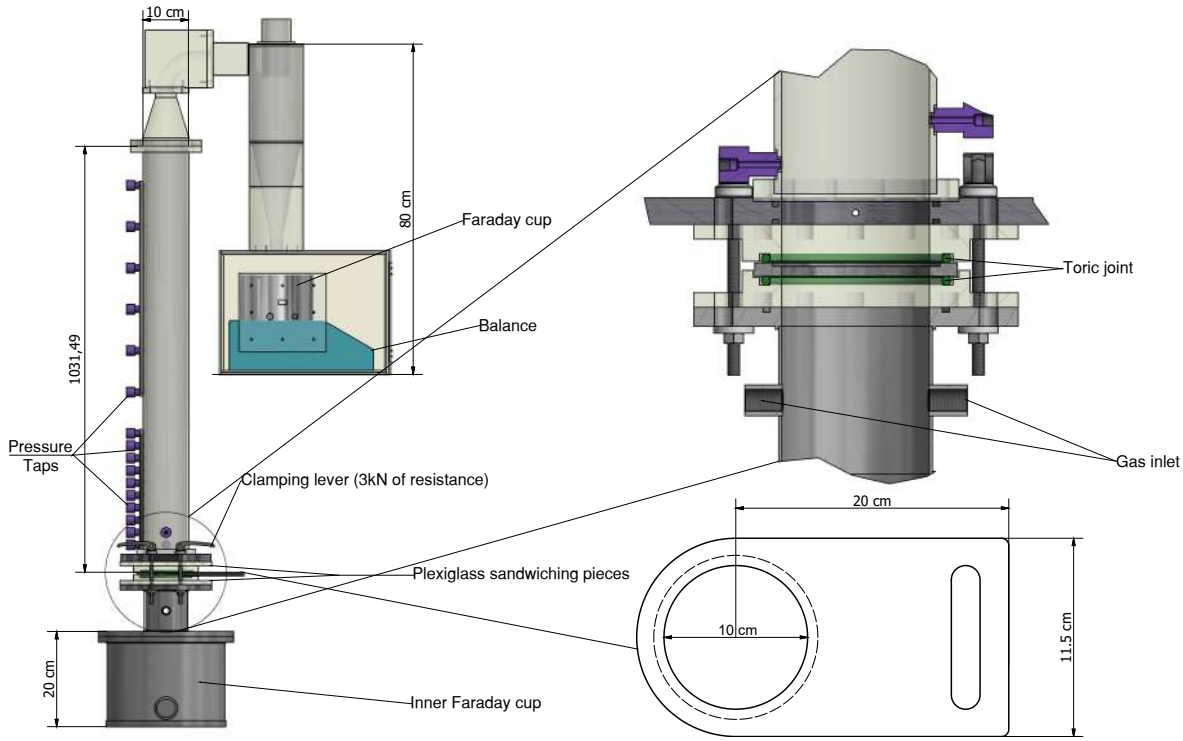

Figure 2.2: Schematic design of the experimental setup

manufactured by PORAL®. It is made by compaction and sintering of metal powders. Pore size is defined by the powder granulometry and classified as PORAL® grade. Figure 2.3 shows a picture of the distributor stuck a metal plate (see fig 2.2 for dimensions).

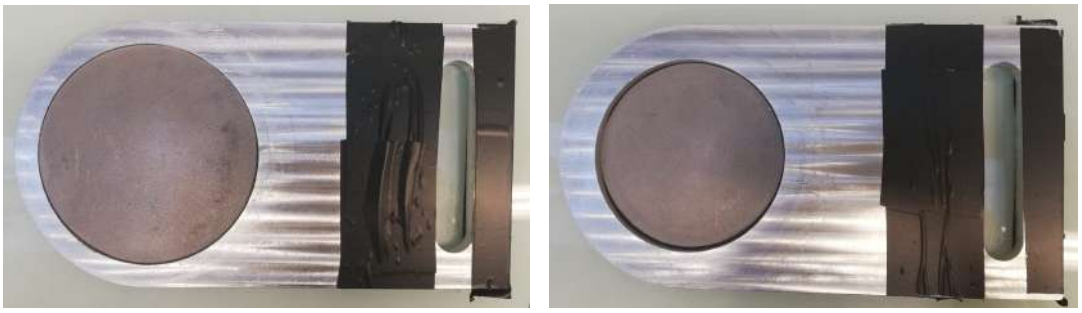

(a) Top view **(b)** Bottom view

Figure 2.3: Sintered metal gas distributor stuck on a metal plate

Two grades (03 and 07) are used for the experiments depending on the size, density of the particles and the gas velocity. The industrial criteria for a pressure drop delivered by a distributor is that it must be greater than 30% of the bed pressure drop. It is given in the product sheet by the following equation (Darcy law):

$$\Delta P = \alpha \beta e \frac{Q_v}{S} \tag{2.1}$$

Where e is the thickness of the plate (m), Q_v is the volume flow rate (m^3/s) and

S is the filtration effective surface. α and β are viscous permeability and inertia permeability coefficients respectively. These two parameters are given in data sheet document with average values depending on the "Poral grade". The choice of the grades were based on the most vulnerable situation. For low flow rates, the minimum value is 0.2 Nm^3/h. Considering the highest grade (07), the pressure drop is $\Delta P_{dist} =$ 88 mbar. The pressure drop in the bed can be estimated by $\Delta P_{bed} = \frac{mg}{S}$ assuming friction wall forces are neglected. Generally, bed wall effects appears in small diameter bed (see Vanni et al. 2015). In all experiments, the powder mass was 2 kg, which gives $\Delta P_{bed} = 25$ mbar. It is clear that the criterion of 30 % is respected in all experiments.

2.1.2 Faraday cup

(a) Copper Faraday cup **(b)** Aluminum Faraday cup

Figure 2.4: Faraday cups for net charge measuring

The electrostatic charges are measured through two Farday cups, first one is in the bottom before the distributor plate and the second one is at the end of the cyclone. The first try was making a simple stainless steel cup and connecting the measuring point (hotspot) to it, but there was a lot of perturbation in the measurements because the electrometer measures a potential difference between the hotspot and the reference. Therefore, the new Faraday cup consisted of two cups, inner and outer cup. The inner cup is connected to the measuring hotspot while the outer cup works as a reference. The space between two cups was closed by plastic media to avoid perturbation during the measurements.

Moreover, the measuring time on the stainless steel cup took too long ($\sim$ 20 min) for and the value keeps growing very slowly. The first amelioration was to made cups with copper material which is more conductive than stainless steel. This reduced the measuring time to $\sim$ 5 min. The second amelioration was in the measuring technique itself. Generally, the studied powders are insulating, for instance, the electric conductivity of glass beads (SiO_2) is about $\sim 10^{-17}$ S/m. Since the charge measured represents in some way the flux of the electrons coming from the powder to the electrometer through the metal, the measured bulk charge through the cup is not exactly the real value. The charge in the center of the cup will take too long to reach the metal because of the very low electric conductivity of the powder. Therefore,

we added metal bars randomly inside the cup to evacuate the maximum amount of the charge. The perfect solution would be adding a metal grid inside the cup. These amelioration reduced the measuring time to $\sim$ 30 s. To make sure the value is constant, the measure was left for longer time but the measured value did not change.

The first Faraday cup which is in the bottom is used to measure the charge of bed particles by opening the distributor and allowing particles to fall in. It was made of copper material (see figure 2.4a). The second one is placed on a balance at the end of the cyclone (see figure 2.4b). It is used to measure the charge of entrained particles while measuring the particle mass simultaneously. Since the sample mass is a limiting factor, this cup was made of aluminum with the same design as stated before (inner and outer cup). It weights about 1.3 kg.

2.1.3 Opening-closing mechanism

In order to allow powders to drop into the Faraday cup, an opening-closing mechanism need to be placed in the distributor plate. The first idea was inspired from the setup of [73], using a knife gate valve. The valve is the same used in closed-conduit flow. It consists of a sliding metal plate, sandwiched between two plates using joints to ensure the sealing. The sliding plate is connected to an actuator working under pressure to allow the opening-closing operation. In the previous works in literature (Sowinski et al. 2009; Giffin and Mehrani 2013), authors perforated directly the holes inside the valve. However, in these experiments, the distributor needs to be welded inside the valve. The thickness of the valve ($\approx$ 5mm) was a big issue. Since the distributor needs to be located at the end of the metal plate, it was quite impossible to weld without distorting this part of the plate due to the high welding temperature. Even if this distortion was about few degrees, it influenced the sealing of the system and the gas was bypassing the distributor.

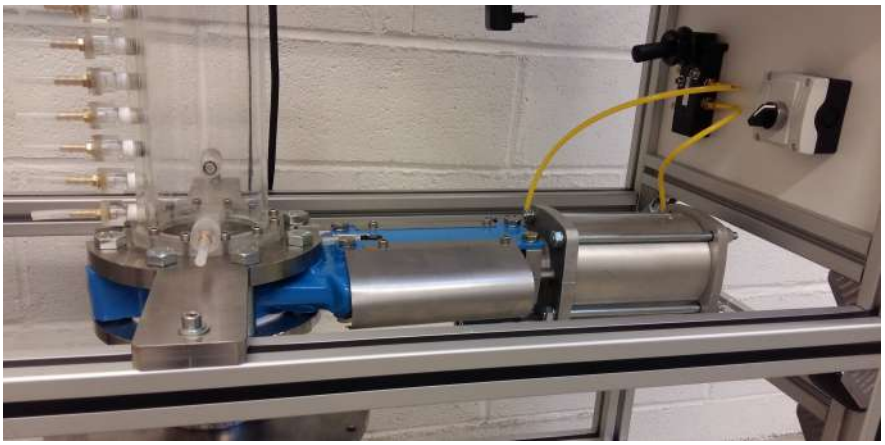

Figure 2.5: Knife gate valve used in the first trials

Therefore, the whole system was modified. The gas distributor was stuck to a thicker metal plate (9mm) using permanent glue. New pieces were designed to sandwich the plate. Figure 2.2 presents a schematic design of the pieces (on the right). The new method consists of using clamping levers between the upper and lower piece to free or tighten the sliding plate. Tight joints were place on both piece to avoid the leakage issues.

2.2 Humidity controller

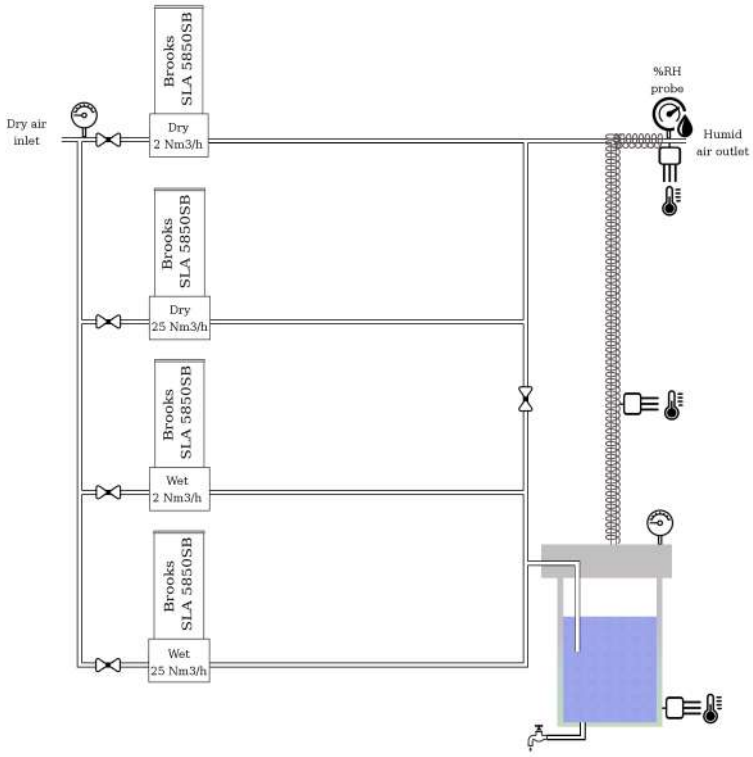

Figure 2.6: Humidity controlling system

According to findings in literature, relative humidity plays an important role in electrostatic charge generation. Thus, a humidity controller was set before the gas inlet in the bed. The main issue was to produce humidity without heating the system. Which means that the dew point needs to be below the operating temperature. This dew point is a function of the pressure drop at the inlet of the bed (before the gas flow distributor). This pressure drop is equal to the sum of linear and singular pressure loss in the circuit. Practically, the gas distributor takes the highest portion of pressure drop. Thus, the sizing of humidity controller was based on this pressure drop while

adding an extra 100 mbar as a margin of security. The air humidification device is made up of two couples of mass flow controller. Each couple includes a dry and wet way. For low ranges, the flow controllers provides up to 2 Nm^3/h and for high range provides up to 25 Nm^3/h. Flow controllers are manufactured by Brooks ®. The accuracy of flow rate is $\pm 1\%$ FS for flow below 20% FS and $\pm 0.2\%$ for flow above. The device gets an instruction and communicate the real delivered value at the same time. The settling time is less than 1 sec.

Figure 2.6 shows a picture of humidity controller system and a schematic design of the the system. The valves switch automatically between ranges to keep a good accuracy. Control board allows to set the value of flow rate, relative humidity and ambient pressure and temperature. Then the system calculates the value of absolute humidity and adjust dry and wet flows automatically to reach the set point. A tank is filled with water in order to supply wet circuit. A pressure transducer is placed on the tank to verify that the pressure drop does not reach saturation pressure. A heating coil is placed in the circuit after the tank to heat system if needed. Three heat probes are placed respectively in the tank, on the heating coil and at the outlet in order to control temperature. A constant value is achieved between 3 and 30 seconds depending on flow rate value. A humidity probe is set after the system to make sure of delivered value of humidity.

The system manages to reach 40% RH in two worst case scenarios without heating: first one is using the grade 03 at 25 Nm^3/h (highest pressure drop) and second one is using grade 05 at 0.2Nm^3/h (lowest flow rate) without reaching the dew point. Since the system does not include drying air, The lowest RH is 5% which is imposed by air compressor. This value does not change with external conditions because the air compressor dries the air before supplying the network. **Note that all the experiments in this study were preformed at ambient conditions without heating the system**.

2.3 Metrology

This section describes devices used in the experiments for pressure, charge and mass measurement. It also presents the data acquisition system

2.3.1 Pressure sensors

Pressure sensors allows to measure the pressure drop through the bed. This pressure drop allows to trace back the average bed height. It give also characteristic frequencies of the bubbles crossing and the transitions between the fluidization regimes. This analysis can be done by post-processing the standard deviation of pressure drop or performing a Fast Fourier Transformation on the pressure signal and analyzing the spectrum (He et al. 2014). Besides, the pressure drop at the bottom of the bed gives the value of the minimum fluidization velocity (see Chapter 1 subsection 1.1.2).

Sensors used in the experiments are differential bidirectional sensors. It is manufactured by BD|SENSORS ®, the reference of the product is DMD 341. It is a piezoresistive stainless steel silicon sensor, which ensure a high accuracy. There are five sensors: two sensors of $\pm$ 60 mbar used for the first two taps (3 cm and 6 cm) and three sensors of $\pm$ 40 mbar (9 cm, 12 cm and 15 cm). The accuracy of the sensors is $\leq$1% of the full scale. The output is in the form of electric signal between 4 and 20 mA and the output frequency is 10 Hz (10 samples per second). The sensor measures the pressure difference between a given point and a reference. All sensors references are connected to the highest point in the column below the bed height (93 cm).

2.3.2 Charge meter: electrometer

Charges are measured by the mean of an electrometer. Its commercial name is Kislter type 5051A. Figure 2.7 illustrates a diagram taken from the device documentation. The device is connected through a BNC cable to the Faraday cup. The measuring principle is based on capacitors, the electrons flow through the BNC to the electric circuit and stored in the capacitors. A schematic diagram illustrating the operating mode is presented in figure 2.8. The value of the charge can be obtained by the simple following equation:

$$Q = C1/U \tag{2.2}$$

Where C1 is the capacitance and U is the voltage measured at the output of the circuit. A series of capacitor are connected in parallel (Figure 2.7) in order to toggle depending on the measuring range. After each measurement, the circuit is discharged using an infinite resistance (R1 $\approx 10^{11}\Omega$).

The electrometer includes different features. The measure can be put in "DC Long" mode where it measures the accumulation of charge or can be refreshed with a given frequency. In this study, all the measurements are performed in "DC Long" mode since we measure the total net charge in the Faraday cup. The device also includes filters for the signal, which are used in other measuring modes. The measurement scale is from ± 2 pC to ± 2.2 μC. The device contains a voltage output from -10 V to +10 V and it is connected to data acquisition system. A charge attenuator is also provided with a

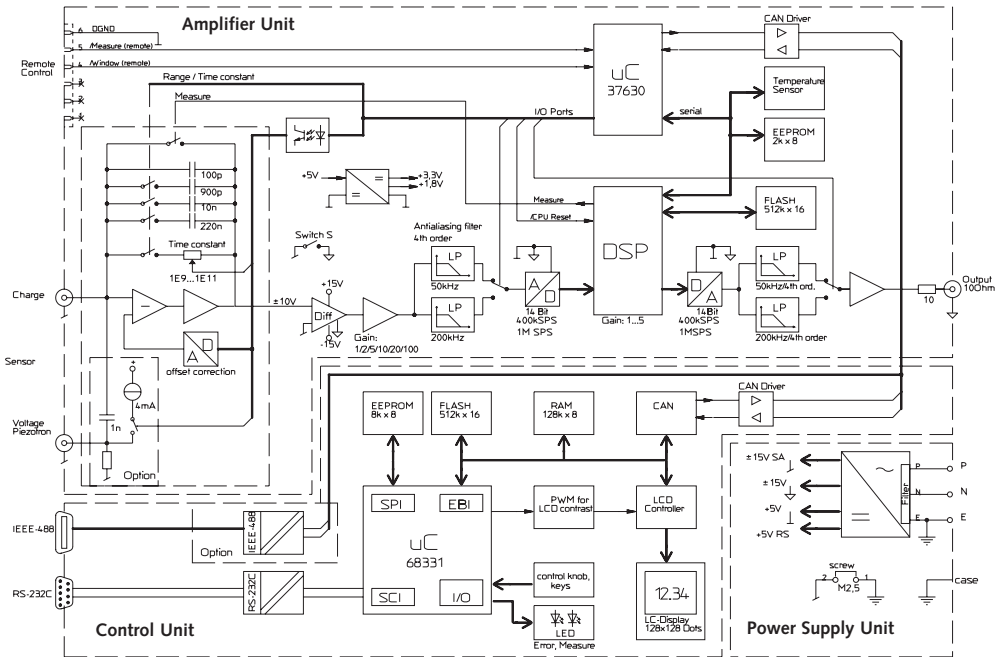

Figure 2.7: Block diagram of charge meter Type 5051A (refer to product manual)

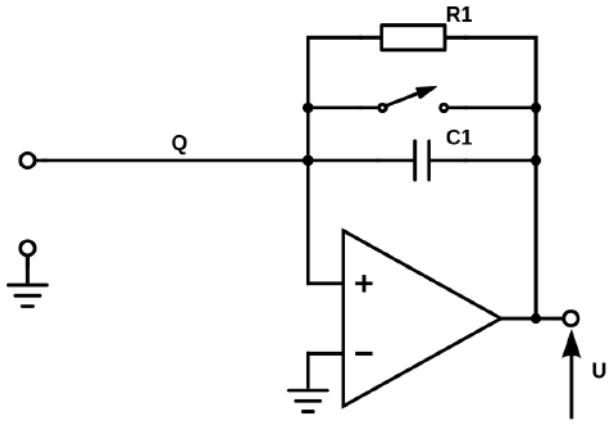

Figure 2.8: Basic electric circuit describing the operating method of charge measuring

1:1000 ratio, which gives a wider measuring scale up to $\pm 2200\ \mu C$. As a precautionary measure, the attenuator is kept connected during all the measurements. The accuracy for values greater than 100 pC (The case in our study) is ≤ 0.5 %. It is important to note that the device should be powered on at least two hours before measurements so that electric components reach the working temperature.

2.3.3 Balance

A balance is used at the end of the cyclone (see figure 2.2 and 2.9) to track the entrainment flux of particles. It can measure up to 3 kg of powder with a 0.1 g of accuracy. It also has an 4-20 mA output which allow to record the mass evolution

Figure 2.9: Balance for entrainment flux tracking

with 1 Hz frequency.

2.3.4 Data acquisition system

Data recording is performed through an 8-Channel USB data acquisition card connected to a computer. The acquisition card is manufactured by DATAQ Instruments, Inc. (model DI-1110). The input of the device is in the form of voltage from -10 V to +10 V. Since balance and pressure sensors have an output of 4-20mA, a resistance of 250 Ω is connected to each channel input to convert amperage to voltage (1-5 V). The sampling frequency can go up to 160 KHz but it was limited to 10 Hz. Data are recorded on a touchpad computer. Figure 2.10 shows a picture of the computer and the acquisition card. The software for recording data is provided with acquisition card, it allows real-time data display and record simultaneously. It also provide statistic analysis, Fast Fourrier Transform, etc. on a selected data range. The data are exported as a csv file (or other format) to post process.

Figure 2.10: Data acquisition system

2.4 Powder characterization

Since the powder was purchased from a manufacturer of blast finishing (Guyson SA), the information available on the description sheet are provided for information purposes only. Thus all material properties needs to be measured accurately.

2.4.1 Particle Size Distribution (PSD)

Table 2.1: Characteristic diameters of materials used in the experiments

Material	Acronym	d_{50}	d_{sauter}	Span
Glass beads	CGB	554	545	0.49
	MGB	267	264	0.43
	SGB	83	81	0.55
Ceramic beads	CB	100	99	0.48

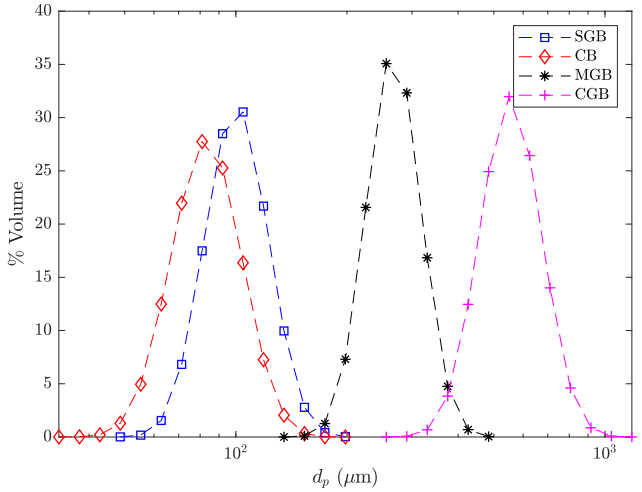

Figure 2.11: PSD for different materials

The first parameter to measure is the diameter of particles. The most used technique is called laser diffraction measurement. During this procedure, particles are passed through a focused laser beam. These particles scatter light at an angle that is inversely proportional to their size. The angular intensity of the scattered light is then measured by a series of photosensitive detectors. The device used in the experiments is the Malvern MasterSizer 3000 (MS3000). It produces a PSD of a sample in wet or dry mode, from sub-micron to millimeter (10 nm to 3 mm), driven by Standard Operation Procedures (SOPs). The number and positioning of these detectors in the Mastersizer 3000 has been optimized to achieve maximum resolution across a broad range of sizes. The map of scattering intensity versus angle is the primary source of information used to calculate the particle size (refer to Malvern MS3000 manual for more details).

SOP contains all the parameters needed for the measurements. It includes, among other parameters, optical properties of the sample and dispersion conditions. This allows to have a sens of comparing different results using the same SOP.

Figure 2.11 presents PSD and table 2.1 summarizes results of MS3000 analysis on four distributions at a dispersion differential pressure of 1 bar. d_{50} is the median

Table 2.2: Density measurements for glass and ceramic beads

	Average volume (cm^3)	Average density (kg/m^3)	Standard deviation (kg/m^3)
Glass beads	4.8664	2476.1	0.3
Ceramic beads	5.1272	3826.5	0.2

diameter. It means that 50% of sample volume have a diameter less or equal to the value. d_{sauter} is Sauter mean diameter, it is defined as the diameter of a sphere that has the same volume/surface area ratio as a particle of interest. The spreading of the PSD is given by the span=$\frac{d_{90} - d_{10}}{d_{50}}$. For a span < 1, the distribution is considered to be tight.

All the distributions are tight, which is an important advantage regarding numerical simulation, it goes with the assumption of monodisperse distribution. Besides, the Sauter mean diameter is almost equal to the mean diameter.

2.4.2 Particles density

The real density of materials is measured by a helium pycnometer. It consists of two chambers, one (with a removable gas-tight lid) to hold the sample and a second chamber of fixed, known (via calibration) internal volume. The device additionally comprises a valve to admit a gas under pressure to one of the chambers, a pressure measuring device connected to the first chamber, a valved pathway connecting the two chambers, and a valved vent from the second of the chambers. Thus, sample density is determined knowing the mass of sample. Helium is prescribed as the measurement gas, not only is it of small atomic diameter, it is also inert and the most ideal gas. The result is obtained by averaging ten measures over thirty minutes. It is important to note that this device is meant for non porous powder, which is the case of this study. Table 2.2 presents the average densities of each material.

2.4.3 Microscope images

Scanning electron microscope (SEM) is a type of electron microscope that produces images of a sample by scanning it with a focused beam of electrons. The electrons interact with atoms in the sample, producing various signals that contain information about the sample's surface topography and composition.

The SEM used for these experiments is manufactured by Hitachi, model TM3000. The specimen stage allows observing sample up to 70 mm diameter and 50 mm thick. Image magnification can go up to x10 000 with a good resolution. For non conducting samples, electrons accumulate on particle surface and prevent normal imaging. Conventionally, the sample is coated with a tin layer of metal before proceeding to the measurements. However, the coating layer can interfere while performing surface chemical analysis. In this study, the particles were not coated since the measuring time was quick and the images taken were of good quality. Figure 2.12 presents particles images of glass beads and ceramic beads. Most of particles are spherical which makes them perfect for comparison with numerical simulation.

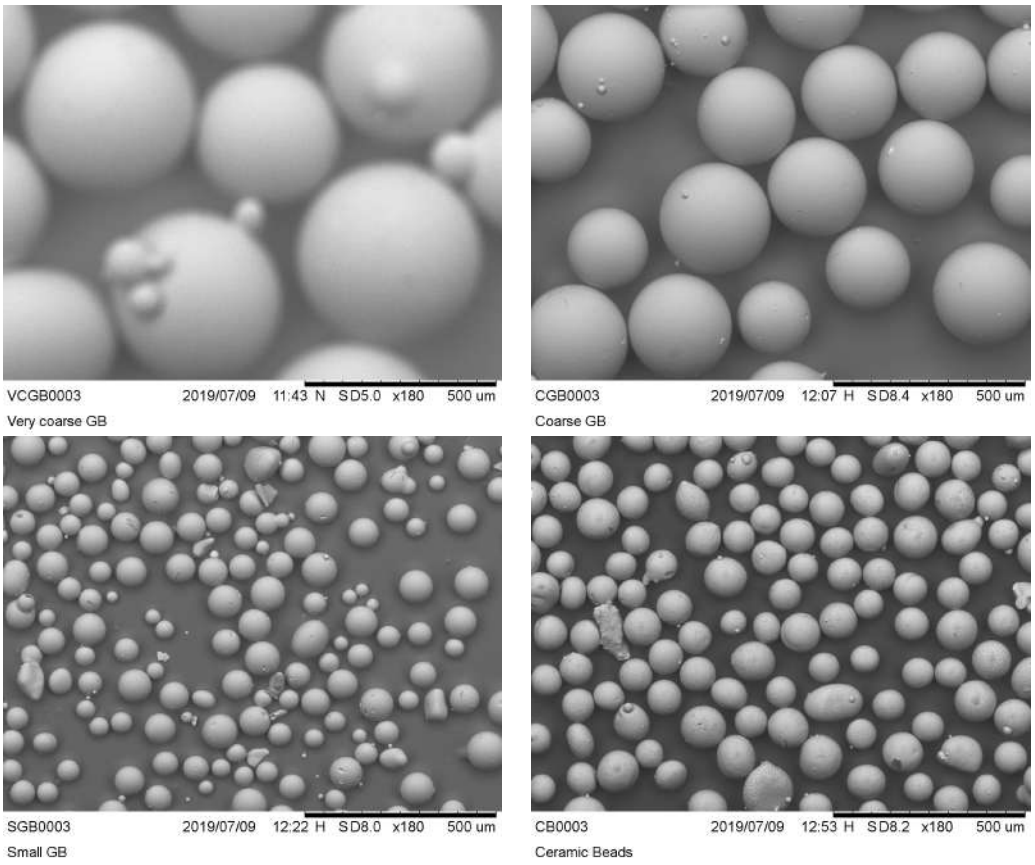

Figure 2.12: Scanning Electron Microscope results

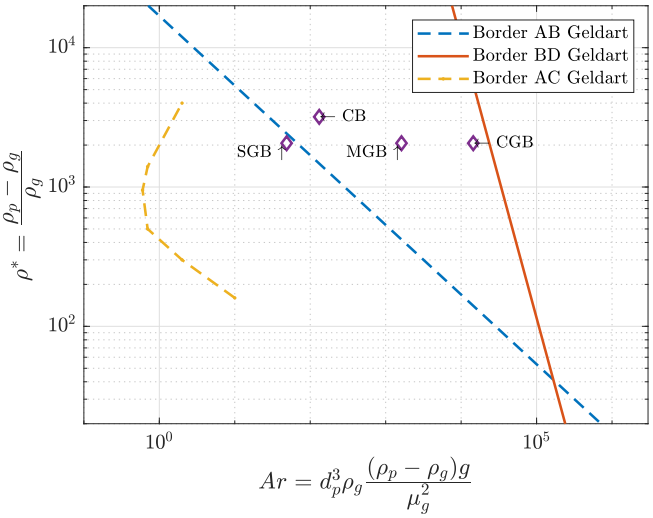

Figure 2.13: Geldart diagram of different materials

2.4.4 Geldart classification

As described before (see subsection 1.1.3), Geldart classification gives an idea of powder behavior. Figure 2.13 presents classification of powders used in experiments according to Geldart. Ceramic beads, medium and coarse glass beads, are in group B which make them easy to fluidize. Small glass beads are in the border AB, which makes their specificity near to group A in a fluidized bed.

2.5 Experiments procedure

The experiments on electrostatic charges always presents issues regarding reproducibility of results even when maintaining same operating conditions. For the first experiments, it was observed that when using two different samples from bulk powder, the measured charge in the Faraday cup were approximately the same value. However, when using the same sample in more than one experiment, there was a huge difference on the values. In order to avoid this issue, four metal cups were used to discharge the powder in order to recycle it. They were connected to the ground and the powder is left all the night. Despite the fact that glass beads cannot be grounded, this procedure gave better reporducibility in results. Besides, electrostatic charges may be generated while filling the powder. Thus, a metal funnel is used instead of plastic one. Figure 2.14 shows a picture of the cups and the metal funnel.

Figure 2.14: Metal cups and funnel used to reduce electrostatic charges

Before each experiment, the column is cleaned with a vacuum cleaner in order to remove any particles left on the wall. The powder is put in metal cup and connected to the ground all the night for discharging the sample. The sample is weighed with a balance. The only factor that can generate charges when filling is the contact with air which we consider negligible since the procedure lasts less than 1 min.

Experiments protocol can be summarized to the following steps:

1. Discharge powder before each experiment
2. Fill the bed using a metal funnel to avoid charge generation
3. Set the flow and relative humidity
4. Fluidize for a given period of time
5. Stop the air supply and let bed settle
6. Open the distributor with actuator
7. Measure the net charge for dropped particles
8. Empty the Faraday cup and weight the dropped particles
9. Put the Faraday cup again to collect the wall particles
10. Tap on column to make wall particles fall in cup and measure their charge and weight

3 Eulerian modeling of electrostatic charges

Figures

Tables

3.1 Eulerian-Eulerian modeling of gas solid monodisperse flows

3.1.1 Introduction

In this chapter, the Eulerian modeling of monodisperse flows. This approach is derived by analogy to the Kinetic Theory of Gas as mentioned in subsection 1.1.5. An electrostatic and a tribocharging model are presented and wall boundary conditions are developed. Some test cases are also run to verify the models.

3.1.2 Mean gas phase transport equation

The phase-averaged transport equation in the frame of the multiphase approach was derived by Gidaspow 1994. The transport equations of the gas phase are deduced by multiplying the instantaneous local equations of mass and momentum by the function χ_g. The phase indicator function χ_g is equal to 1 if the gas phase is present, 0 otherwise. The average mass balance equation is:

$$\frac{\partial \alpha_g \rho_g}{\partial t} + \frac{\partial}{\partial x_i}\left(\alpha_g \rho_g U_{g,i}\right) = \Gamma_g \tag{3.1}$$

where $\alpha_g = \langle \chi_g \rangle$ represents the gas-phase mean-fraction rate. $U_{g,i}$ is the gas phase mean velocity and Γ_g represents the mass transfer between phases.

The averaged momentum balance equation for gas phase is:

$$\begin{aligned}\alpha_g \rho_g \left(\frac{\partial U_{g,i}}{\partial t} + U_{g,j}\frac{\partial U_{g,i}}{\partial x_j}\right) = &- \alpha_g \frac{\partial P_g}{\partial x_i} + \alpha_g \rho_g g_i + \frac{\partial \Sigma_{g,ij}}{\partial x_j} \\ &+ I_{p\to g,i} + [U_{\sigma,i} - U_{g,i}]\Gamma_g\end{aligned} \tag{3.2}$$

P_g is the mean pressure and g_i is the gravity. The third term on the right hand side (r.h.s) in the momentum equation is due to the velocity fluctuations and viscous stresses. It is expressed as:

$$\Sigma_{g,ij} = -\alpha_g \rho_g \left\langle u'_{g,i} u'_{g,j} \right\rangle_g + S_{g,ij} \tag{3.3}$$

The first term refers to the pseudo turbulent-Reynolds stress tensor. $S_{g,ij}$ is the viscous stress tensors, it is written as:

$$S_{g,ij} = \nu_g \left(\frac{\partial U_{g,i}}{\partial x_j}\frac{\partial U_{g,j}}{\partial x_i} - \frac{2}{3}\frac{\partial U_{g,m}}{\partial x_m}\delta_{i,j}\right) \tag{3.4}$$

$I_{p\to g,i}$ represents the force exerted at the particle surface by the continuous phase due to viscous stress and pressure gradient fluctuations. $U_{\sigma,i}$ is the averaged velocity of the mass flux through the interface.

The term $\left\langle u'_{g,i}u'_{g,i}\right\rangle_g$ is unknown and thus the momentum equation of the gas phase need closure laws to be closed. In this study, the turbulent model used is $k-\varepsilon$ complemented by additional terms accounting for the interactions with the dispersed phase (Boelle et al. 1995; Gobin et al. 2003). The turbulent Reynolds stress tensor is modeled based on the Boussinesq concept of turbulent viscosity. It is written as a function of the stresses and of the kinetic energy k:

$$\left\langle u'_{g,i}u'_{g,j}\right\rangle = -\nu_g^t\left[\frac{\partial U_{g,i}}{\partial x_j}+\frac{\partial U_{g,j}}{\partial x_i}\right]+\frac{2}{3}\left[k+\nu_g^t\frac{\partial U_{g,m}}{\partial x_m}\right]\delta_{ij} \tag{3.5}$$

In this equation, ν_g^t is the turbulent viscosity which is modeled as follows (Vermorel et al. 2003):

$$\nu_g^t = \frac{2}{3}k\tau_g^t\left[1+C_{12}\frac{\alpha_p\rho_p}{\alpha_g\rho_g}\frac{\tau_{gp}^t}{\tau_{gp}^F}(1-\frac{q_{gp}}{2k})\right]^{-1} \tag{3.6}$$

where $\tau_g^t = C_\mu\frac{2}{3}\frac{k}{\varepsilon}$ is the characteristic timescale of the turbulence. τ_{gp}^t and τ_{gp}^F are respectively timescale related to the interaction between the continuous and the dispersed phases and q_{gp} is the fluid-particle velocity covariance.

Equations 3.5 and 3.6 are closed by modeling the turbulent kinetic energy k and the dissipation rate ε by a transport equation:

$$\begin{aligned}\alpha_g\rho_g\left(\frac{\partial}{\partial t}+U_{g,i}\frac{\partial}{\partial x_j}\right)k = &\underbrace{\frac{\partial}{\partial x_j}\left(\alpha_g\rho_g\frac{\nu_g^t}{\sigma_k}\frac{\partial k}{\partial x_j}\right)}_{\text{Diffusion}}\\ &\underbrace{-\alpha_g\rho_g\left\langle u'_{g,i}u'_{g,j}\right\rangle_g\frac{\partial U_{g,i}}{\partial x_j}}_{\text{Production}}\\ &-\underbrace{\alpha_g\rho_g\varepsilon}_{\text{Dissipation}}\\ &+\underbrace{\Pi_{p\to g}^k}_{\text{Two-way coupling}}\end{aligned} \tag{3.7}$$

$$\begin{aligned}\alpha_g\rho_g\left(\frac{\partial}{\partial t}+U_{g,i}\frac{\partial}{\partial x_j}\right)\varepsilon = &\underbrace{\frac{\partial}{\partial x_j}\left(\alpha_g\rho_g\frac{\nu_g^t}{\sigma_\varepsilon}\frac{\partial\varepsilon}{\partial x_j}\right)}_{\text{Diffusion}}\\ &\underbrace{-\alpha_g\rho_g\frac{\varepsilon}{k}\left\langle u'_{g,i}u'_{g,j}\right\rangle_g\frac{\partial U_{g,i}}{\partial x_j}}_{\text{Production}}\\ &\underbrace{-\alpha_g\rho_g C_{\varepsilon 2}\frac{\varepsilon^2}{k}}_{\text{Dissipation}}\\ &+\underbrace{\Pi^\varepsilon_{p\to g}}_{\text{Two-way coupling}}\end{aligned} \tag{3.8}$$

Terms "Two-way coupling" account for the effect of the particles on the gas. They are written assuming small particle size with respect to fluid turbulent energetic scales:

$$\Pi^k_{p\to g}=\frac{\alpha_p\rho_p}{\tau^F_{gp}}\left(-2k+q_{pg}+V_{d,i}V_{r,i}\right) \tag{3.9}$$

$$\Pi^\varepsilon_{p\to g}=C_{\varepsilon 3}\frac{\varepsilon}{k}\Pi^k_{p\to g} \tag{3.10}$$

where $V_{r,i}$ and $V_{d,i}$ are respectively the mean relative velocity and the drift velocity (see equations 3.27 and 3.28). Constants required for the turbulence modeling are presented in table 3.1.

Table 3.1: Constants for gas phase turbulence $k-\varepsilon$ model

C_{12}	C_μ	σ_k	σ_ε	$C_{\varepsilon 1}$	$C_{\varepsilon 2}$	$C_{\varepsilon 3}$
0.34	0.09	1	1.3	1.44	1.92	1.2

3.1.3 Eulerian dispersed phase transport equations

In this section, the motion of particles in monodisperse solid phase is described. In order to derive a continuum model for the solid phase, it is assumed that the motion of particles in a rapid granular flow is very similar to the motion of molecules in a gas. This allows to use the kinetic theory to obtain the governing equation of the solid phase (Gidaspow 1994).

From now on, the electric charge per mass unit is considered instead of electric charge and **the word "charge" means implicitly electric charge per mass unit**. It will be refered as $\chi_p^c = \dfrac{\langle q_p \rangle}{m_p}$. ζ_p' refers to the fluctuation around the mean value:

$$\zeta_p' = \zeta_p - \chi_p^c \tag{3.11}$$

Let $f\left(\mathbf{x}, \mathbf{c_p}, \zeta_p, t\right) \delta\mathbf{x}\delta\mathbf{c_p}\delta\zeta_p$ be the probable number of particles with the center of mass in the volume element $[\mathbf{x}, \mathbf{x} + \delta\mathbf{x}]$ at time t, with a velocity in the range $[\mathbf{c_p}, \mathbf{c_p} + \delta\mathbf{c_p}]$ and an electric charge in the range $[\zeta_p, \zeta_p + \delta\zeta_p]$. Using this function we have the definition for the particle number density (n_p) and the mean value for any property ϕ:

$$n_p = \int_{\mathbb{R}^3} \int_{\mathbb{R}} f_p d\zeta_p d\mathbf{c}_p \tag{3.12}$$

$$\langle \psi_p \rangle = \frac{1}{n_p} \int_{\mathbb{R}^3} \int_{\mathbb{R}} \psi f_p d\zeta_p d\mathbf{c}_p \tag{3.13}$$

This allows us to define some useful quantities such as the particle mean velocity:

$$U_{p,i} = \langle u_{p,i} \rangle = \frac{1}{n_p} \int_{\mathbb{R}^3} \int_{\mathbb{R}} c_{p,i} f_p d\zeta_p d\mathbf{c}_p \tag{3.14}$$

The particle velocity fluctuation:

$$u'_{p,i} = u_{p,i} - U_{p,i} \tag{3.15}$$

The particle kinetic stress tensor:

$$S_{p,ij} = \left\langle u'_{p,i} u'_{p,j} \right\rangle = \frac{1}{n_p} \int_{\mathbb{R}^3} \int_{\mathbb{R}} c'_{p,i} c'_{p,j} f_p d\zeta_p d\mathbf{c}_p \tag{3.16}$$

The particle mean electric charge:

$$\chi_p^c = \langle \zeta_p \rangle = \frac{1}{n_p} \int_{\mathbb{R}^3} \int_{\mathbb{R}} \zeta_p f_p d\zeta_p d\mathbf{c}_p \tag{3.17}$$

The electric charge variance:

$$\left\langle \zeta_p' \zeta_p' \right\rangle = \frac{1}{n_p} \int_{\mathbb{R}^3} \int_{\mathbb{R}} \zeta_p' \zeta_p' f_p d\zeta_p d\mathbf{c}_p \tag{3.18}$$

The dynamic evolution of f_p is given by the Boltzmann equation:

$$\begin{aligned} \frac{\partial f_p}{\partial t} + \frac{\partial}{\partial x_i}\left[c_{p,i} f_p\right] + \frac{\partial}{\partial c_{p,i}}\left[\left\langle \frac{du_{p,i}}{dt} \left| \mathbf{x},\ \mathbf{c_p}, \xi_p \right. \right\rangle f_p\right] + \\ \frac{\partial}{\partial \xi_p}\left[\left\langle \frac{dq_p}{dt} \left| \mathbf{x},\ \mathbf{c_p}, \xi_p \right. \right\rangle f_p\right] = \left(\frac{\partial f_p}{\partial t}\right)_{coll} \end{aligned} \tag{3.19}$$

The notation $\left\langle G \left| \mathbf{x}, \mathbf{c_p}, \zeta_p \right. \right\rangle$ is a short form for the conditional expectation G at the position $\mathbf{x_p} = \mathbf{x}$, with a velocity $\mathbf{u_p} = \mathbf{c_p}$ and a charge $q_p = \zeta_p$ at a given time t: $\left\langle G \left| \mathbf{x_p} = \mathbf{x}, \mathbf{u_p} = \mathbf{c_p}, q_p = \zeta_p; t \right. \right\rangle$.

The right hand side (r.h.s) of the Boltzmann equation accounts for the variation due to particle-particle collisions. We will consider that the particle charge only changes due to the collisions with other particles, hence:

$$\frac{dq_p}{dt} = 0 \tag{3.20}$$

Multiplying equation 3.19 by the property ψ_p and integrating over the whole velocity and charge domain gives a general equation governing ψ_p:

$$\begin{aligned} \frac{Dn_p \left\langle \psi_p \right\rangle}{Dt} + n_p \left\langle \psi_p \right\rangle \frac{\partial U_{p,i}}{\partial x_i} + \frac{\partial n_p \left\langle \psi_p c_{p,i}' \right\rangle}{\partial x_i} - n_p \left\langle \frac{D\psi_p}{Dt} \right\rangle - n_p \left\langle c_{p,i}' \frac{\partial \psi_p}{\partial x_i} \right\rangle \\ - n_p \left\langle \frac{F_i}{m_p} \frac{\partial \psi_p}{\partial c_{p,i}'} \right\rangle + n_p \frac{DU_{p,i}}{Dt} \left\langle \frac{\partial \psi_p}{\partial c_{p,i}'} \right\rangle + n_p \left\langle c_{p,j}' \frac{\partial \psi_p}{\partial c_{p,i}'} \right\rangle \frac{\partial U_{p,i}}{\partial x_j} = \mathcal{C}\left(\psi_p\right) \end{aligned} \tag{3.21}$$

The right hand side of the equation accounts for the mean transfer rate of the property ψ_p due to collisions. Following formulation proposed by Jenkins and Savage 1983 the term can be written as the contribution of a source term and a flux term.

Particle mass transport equation

Substituting ψ_p by m_p give the transport equation of the mass of the particle p:

$$\frac{\partial \alpha_p \rho_p}{\partial t} + \frac{\partial \alpha_p \rho_p U_{p,i}}{\partial x_i} = 0 \tag{3.22}$$

During any collision, there is no loss of mass. Then, the collision term is null. In the frame of the Eulerian approach, the solid volume fraction is defined as $\alpha_p = \dfrac{n_p m_p}{\rho_p}$ where n_p is the mean number of particles per unit volume and $\{m_p\}_p$ the mean solid mass. The operators $\{\cdot\}_p$ and $\langle\cdot\rangle_p$ represent, respectively, the average and the mass-weighted average over the particle property space (Simonin 2000). Hence, gas and particle volume fractions, α_g and α_p have to satisfy:

$$\alpha_g + \alpha_p = 1 \tag{3.23}$$

Particle momentum transport equation

Substituting ψ_p by $m_p u_{p,i}$ leads to a transport equation of the momentum of the particle p:

$$\frac{\partial}{\partial t}\left[\alpha_p \rho_p U_{p,i}\right] + \frac{\partial}{\partial x_j}\left[\alpha_p \rho_p U_{p,i} U_{p,j}\right] = \frac{\partial \Sigma_{p,ij}}{\partial x_j} + \alpha_p \frac{\partial P_g}{\partial x_i} + \alpha_p \rho_p g_i + \alpha_p \rho_p \left\langle \frac{F_{r,i}}{m_p} \right\rangle_p + \alpha_p \rho_p \chi_p^c E_i + U_{\sigma,i} \Gamma_p \tag{3.24}$$

The first r.h.s term is the collisional stress tensor. E_i is the electric field, solved trough the Poisson equation 3.66.

Mean interphase transfer

The mean interphase gas-to-particle momentum transfer is:

$$I_{g\to p,i} = \alpha_p \rho_p \left\langle \frac{F_{r,i}}{m_p} \right\rangle_p \tag{3.25}$$

it satisfies the condition $I_{g\to p,i} + I_{p\to g,i} = 0$. Assuming particles are hard spheres and move by translation in a nonuniform flow, it is written as:

$$I_{g\to p,i} = -\frac{\alpha_p \rho_p}{\tau_{gp}^F} V_{r,i} \tag{3.26}$$

where where $V_{r,i}$ is the mean relative velocity, written as a function of mean phase velocities and fluid-particle turbulence drift velocity ($V_{d,i}$) due to the turbulent correlation between the instantaneous particle distribution and the fluid velocity field. It is expressed as:

$$V_{r,i} = (U_{p,i} - U_{g,i}) - V_{d,i} \tag{3.27}$$

The drift velocity accounts for the turbulence transport of the dispersed phase by the fluid turbulence. It is written as (Fotovat et al. 2015):

$$V_{d,i} = -D_{gp}^{t}\left(\frac{1}{\alpha_p}\frac{\partial \alpha_p}{\partial x_i} - \frac{1}{\alpha_g}\frac{\partial \alpha_g}{\partial x_i}\right) \tag{3.28}$$

where D_{gp}^{t} is the dispersion coefficient. It is proportional to the fluid-particle velocity covariance (q_{pg}) and to an eddy-particle interaction time τ_{gp}^{t} characterizing the fluid turbulence viewed by the particles:

$$D_{gp}^{t} = \tau_{gp}^{t}\frac{1}{3}q_{gp} \tag{3.29}$$

The relaxation time τ_{gp}^{F} refers to a mean particle dynamic relaxation time due to interaction with the fluid turbulence. It is defined with correlations depending on the value of α_p:

$$\frac{1}{\tau_{gp}^{F}} = \frac{3}{4}\frac{\rho_g}{\rho_p}\frac{\langle|\vec{v}_r|\rangle_p}{d_p}C_d(Re_p) \tag{3.30}$$

$$I_{g\to p,i} = -\frac{\alpha_p\rho_p}{\tau_{gp}^{F}}V_{rp,i} \tag{3.31}$$

$$\frac{1}{\tau_{gp}^{F}} = \frac{3}{4}\frac{\rho_g}{\rho_p}\frac{\langle|\vec{v}_r|\rangle_p}{d_p}C_d(Re_p) \tag{3.32}$$

$$C_d(Re_p) = \begin{cases} C_{d,WY} & \text{if} \quad \alpha_g \geq 0.7 \\ \min\left[C_{d,WY}, C_{d,Erg}\right] & \text{else} \quad \alpha_g < 0.7 \end{cases} \tag{3.33}$$

$$C_{d,WY} = \begin{cases} \frac{24}{Re_p}\left(1 + 0.15Re_p^{0.687}\right)\alpha_g^{-1.7} & Re_p < 1000 \\ 0.44\alpha_g^{-1.7} & Re_p \geq 1000 \end{cases} \tag{3.34}$$

$$C_{d,Erg} = 200\frac{(1-\alpha_g)}{Re_p} + \frac{7}{3}, \quad Re_p = \alpha_g\frac{\rho_g\langle|\vec{v}_r|\rangle_p d_p}{\mu_g} \tag{3.35}$$

Particle stress tensor

In the same way defined for gas (equation 3.3), the effective particle stress tensor is written as:

$$\Sigma_{p,ij} = -\alpha_p\rho_p\left\langle u'_{p,i}u'_{p,j}\right\rangle_p + S_{p,ij} \tag{3.36}$$

The first term is the mean collisional rate of change of the transported particle property and represents the integral of all possible collisions of the change in $m_p u_{pi}$. The second term accounts for the momentum transport by the fluctuations. The modeling of those terms is derived in the frame of the KTGF (Jenkins and Richman 1986), accounting for the effect of the interstitial fluid (Simonin 2000). So, both the

kinetic and the collisional parts of the effective stress will be functions of the particle agitation and the fluid-particle correlation. The kinetic part is found to be dominant in dilute flows, whereas the collisional part is dominant in dense flows.

Using Boussinesq approximation, the particle kinetic stress tensor is expressed as:

$$\left\langle u'_{p,i}u'_{p,j}\right\rangle = -\nu_p^{kin}\left[\frac{\partial U_{p,i}}{\partial x_j}+\frac{\partial U_{p,j}}{\partial x_i}\right]+\frac{2}{3}\left[\frac{3}{2}\Theta_p+\nu_p^{kin}\frac{\partial U_{p,m}}{\partial x_m}\right]\delta_{ij} \tag{3.37}$$

where Θ_p is the granular temperature. The particle kinetic viscosity ν_p^{kin} accounts directly for the combined effects of different mechanisms, such as the transport of the particle momentum by the fluid turbulence and by the random motion of the particles:

$$\nu_p^{kin} = \left[\nu_{gp}^t+\frac{1}{2}\tau_{gp}^F\Theta_p\left(1+\alpha_p g_0\Phi_c\right)\right]\left(1+\frac{\tau_{gp}^F}{2}\frac{\sigma_c}{\tau_p^c}\right)^{-1} \tag{3.38}$$

the collisional part of the effective particle stress tensor is written as (Boelle et al. 1995; Jenkins and Richman 1986):

$$\begin{aligned} S_{p,ij} = &\left[\alpha_p\rho_p 2\alpha_p g_0(1+e_c)\Theta_p - -\Lambda_p\frac{\partial U_{p,m}}{\partial x_m}\right]\delta_{ij} \\ &+\alpha_p\rho_p\nu_p^{col}\left(\frac{\partial U_{p,i}}{\partial x_j}+\frac{\partial U_{p,j}}{\partial x_i}-\frac{2}{3}\delta_{ij}\frac{\partial U_{p,m}}{\partial x_m}\right) \end{aligned} \tag{3.39}$$

where ν_p^{col} is the collisional viscosity:

$$\nu_p^{col} = \frac{4}{5}\alpha_p g_0(1+e_c)\left(\nu_p^{kin}+d_p\sqrt{\frac{\Theta_p}{\pi}}\right) \tag{3.40}$$

$$g_0 = \left[1-\frac{\alpha_p}{\alpha_{p,max}}\right]^{-2.5\alpha_{p,max}}, \quad e_c = 0.9, \quad \alpha_{p,max} = 0.64 \tag{3.41}$$

$$\Phi_c = \frac{2}{5}(1+e_c)(3e_c-1), \quad \sigma_c = \frac{1}{5}(1+e_c)(3-e_c) \tag{3.42}$$

$$\Lambda_p = \alpha_p\rho_p\frac{4}{3}\alpha_p g_0(1+e_c)d_p\sqrt{\frac{\Theta_p}{\pi}} \tag{3.43}$$

$$\frac{1}{\tau_p^c} = 24\frac{\alpha_p g_0}{d_p}\sqrt{\frac{16}{\pi}\frac{\Theta_p}{\pi}} \tag{3.44}$$

The function g_0 is the radial distribution function. In the KTFG, it takes into account the increased probability of collisions in dense gases compared to dilute gases, for which the function g_0 is equal to unity.

A transport equation is derived from equation 3.21 for the particle fluctuant kinetic energy, $q_p^2 = \left\langle u'_{p,i} u'_{p,i} \right\rangle /2$. In order to avoid any confusion with the electric charge q_p, the granular temperature is used instead, which verifies $\Theta_p = \frac{1}{3} \left\langle u'_{p,i} u'_{p,i} \right\rangle$:

$$\begin{aligned} \alpha_p \rho_p \left[\frac{\partial \Theta_p}{\partial t} + U_{p,j} \frac{\partial \Theta_p}{\partial x_j} \right] = \frac{\partial}{\partial x_j} \left[\alpha_p \rho_p \left(K_p^{kin} + K_p^{col} \right) \frac{\partial \Theta_p}{\partial x_j} \right] \\ + \frac{2}{3} \Sigma_{p,ij} \frac{\partial U_{p,i}}{\partial x_j} - \alpha_p \rho_p \epsilon_p + \Pi_{\Theta_p} \end{aligned} \tag{3.45}$$

where:

$$K_p^{kin} = \left[\frac{1}{3} \tau_{gp}^t q_{gp} + \frac{5}{9} \tau_{gp}^F \Theta_p \left(1 + \alpha_p g_0 \varphi_c \right) \right] \left[1 + \frac{5}{9} \tau_{gp}^F \frac{\xi_c}{\tau_p^c} \right]^{-1} \tag{3.46}$$

$$K_p^{col} = \alpha_p g_0 (1 + e_c) \left[\frac{6}{5} K_p^{kin} + \frac{4}{3} d_p \sqrt{\frac{\Theta_p}{\pi}} \right] \tag{3.47}$$

ϵ_p is the particle kinetic energy dissipation rate due to inelastic collisions:

$$\epsilon_p = \frac{1}{3} \left(1 - e_c^2 \right) \frac{\Theta_p}{\tau_c} \tag{3.48}$$

The interphase turbulent kinetic energy transfer rate Θ_p is:

$$\Pi_{\Theta_p} = \frac{2}{3} \alpha_p \rho_p \frac{1}{\tau_{gp}^F} \left(3\Theta_p - q_{gp} \right) \tag{3.49}$$

The transport equation for the fluid-particle velocity correlation $q_{gp} = \left\langle u'_{g,i} u'_{p,i} \right\rangle$ is written as (Fevrier and Simonin 1998; Simonin et al. 1993):

$$\begin{aligned} \alpha_p \rho_p \left[\frac{\partial q_{gp}}{\partial t} + U_{p,j} \frac{\partial q_{gp}}{\partial x_j} \right] = \frac{\partial}{\partial x_j} \left(\alpha_p \rho_p \frac{\nu_{gp}^t}{\sigma_k} \frac{\partial q_{gp}}{\partial x_j} \right) - \alpha_p \rho_p \epsilon_{gp} + \Pi_{q_{gp}} \\ - \alpha_p \rho_p \left[\left\langle u'_{g,i} u'_{p,j} \right\rangle_p \frac{\partial U_{p,i}}{\partial x_j} + \left\langle u'_{g,j} u'_{p,i} \right\rangle_p \frac{\partial U_{p,j}}{\partial x_i} \right] \end{aligned} \tag{3.50}$$

where ϵ_{gp} is the fluid-particle covariance dissipation rate due to viscous dissipation and crossing trajectory effects:

$$\epsilon_{gp} = \frac{q_{gp}}{\tau_{gp}^t} \tag{3.51}$$

The interphase interaction term is written as:

$$\Pi_{q_{gp}} = -\alpha_p \rho_p \frac{1}{\tau_{gp}^F} \left[(q_{gp} - 2k) + \frac{\alpha_p \rho_p}{\alpha_g \rho_g} (q_{gp} - 3\Theta_p) \right] \tag{3.52}$$

The fluid-particle velocity correlation tensor $\left\langle u'_{g,i}u'_{p,j}\right\rangle_p$ is written using Boussinesq approximation (Fevrier and Simonin 1998; Gobin et al. 2003; Simonin 2000):

$$\begin{aligned}\left\langle u'_{g,i}u'_{p,j}\right\rangle_p = &\frac{1}{3}q_{gp}\delta_{ij} + \frac{\eta_r}{1+\eta_r}\left[\left\langle u'_{g,i}u'_{g,j}\right\rangle_g - \frac{2}{3}k\delta_{ij}\right] \\ &- \frac{\nu^t_{gp}}{1+\eta_r}\left[\frac{\partial U_{g,i}}{\partial x_j} + \frac{\partial U_{p,j}}{\partial x_i} - \frac{1}{3}\delta_{ij}\left(\frac{\partial U_{g,m}}{\partial x_m} + \frac{\partial U_{p,m}}{\partial x_m}\right)\right]\end{aligned} \tag{3.53}$$

3.2 Electrostatic force

This section aims to model the electrostatic force in solid phase momentum balance equation 3.24. The electrostatic model chosen is the one presented by Rokkam et al. 2010. Model starts with the well known Maxwell equations used to describe electromagnetic phenomenon. Author reported that Lorentz force coupled with these equations are sufficient to describe the force acting on a point charge in the presence of electromagnetic fields. The Four Maxwell equations are:

- The Gauss's law:

$$\nabla \cdot \mathbf{D} = q_v \tag{3.54}$$

- Gauss's law for magnetism:

$$\nabla \cdot \mathbf{B} = 0 \tag{3.55}$$

- Faraday's law:

$$\nabla \times \mathbf{E} = -\frac{\partial \mathbf{B}}{\partial t} \tag{3.56}$$

- Ampere's law with Maxwell's displacement current correction

$$\nabla \times \mathbf{H} = \mathbf{J} + \frac{\partial \mathbf{D}}{\partial t} \tag{3.57}$$

where ∇, $\mathbf{D}$, q_v, $\mathbf{B}$, $\mathbf{E}$, $\mathbf{H}$ and $\mathbf{J}$ are respectively the gradient operator, electric displacement (C/m^2), charge density (C/m^3), magnetic field (Teslas), electric field (V/m), magnetic field strength (A/m) and current density (A/m^2).

Lorentz force is expressed as:

$$F = q(\mathbf{E} + \mathbf{V} \times \mathbf{B}) \tag{3.58}$$

where q is the electric charge (C), $\mathbf{E}$ is the electric field (V/m), $\mathbf{V}$ is the particle velocity vector of the particle (m/s) and $\mathbf{B}$ is the magnetic field (Teslas). Since the velocity of particles in this study is much less than the speed of light, the magnetic part of the equation will be neglected.

The relation between the electric displacement and the electric field is:

$$\mathbf{D} = \varepsilon_0 \mathbf{E} + \mathbf{P} \tag{3.59}$$

where ε_0 is the permittivity of vacuum (Farads/m) and $\mathbf{P}$ is the polarization vector (C/m^2). Under the assumption of isotropic medium, polarization is written as:

$$\mathbf{P} = \varepsilon_0 \chi_e \mathbf{E} \tag{3.60}$$

where χ_e is is the electric susceptibility of the medium and $\varepsilon_m = 1 + \chi_e$ is the relative permittivity. The Gauss equation 3.54 is then written as:

$$\nabla \cdot (\varepsilon_m \varepsilon_0 \mathbf{E}) = q_v \tag{3.61}$$

The main issue is calculating the relative permittivity of the medium ε_m. Some authors calculated it based on the Bruggeman equation (Rokkam et al. 2010; Tan et al. 2018) which calculates the permittivity of the gas-solid mixture if the relative permittivities of pure gas and solid are known as follows:

$$\alpha_g = \left(\frac{\varepsilon_p - \varepsilon_m}{\varepsilon_p - \varepsilon_g}\right)\left(\frac{\varepsilon_g}{\varepsilon_m}\right)^{\frac{1}{3}} \tag{3.62}$$

where α_g is the volume fraction of the gas, ε_g is the relative permittivity of the gas phase, ε_p is the relative permittivity of the solid phase, and ε_m is the relative permittivity of the mixture. Tan et al. 2018 used a linear fitting method to give a linear relation between particle volume fraction α_p and the relative permittivity of the mixture for glass beads:

$$\varepsilon_m = 4.2264\alpha_p + 0.7976 \tag{3.63}$$

Going back to the electric field, and since the electromagnetic field is neglected, Faraday's law 3.56 will be:

$$\nabla \times \mathbf{E} = 0 \tag{3.64}$$

The curl of electric field is zero, a scalar is then defined as the electric potential:

$$\mathbf{E} = -\nabla \varphi \tag{3.65}$$

Substituting equations 3.65 and 3.63 into equation 3.61 gives the following Poisson equation:

$$\nabla \cdot \left(\left(4.2264\alpha_p + 0.7976\right) \nabla \varphi\right) = -\frac{q_v}{\varepsilon_0} \tag{3.66}$$

Under the assumption that, for a given mixture of solid, every solid phase carries a fixed charge (Rokkam et al. 2010), the charge density is calculated as:

$$q_v = \sum_{s=1}^{N_{solids}} q_{p,s}\alpha_{p,s} \tag{3.67}$$

where $\alpha_{p,s}$ and $q_{p,s}$ are the volume fraction and the charge per volume unit (C/m^3) on the s^{th} solid phase. N_{solids} is the total of solid phases. Then, the Lorentz force acting on each solid phase is:

$$\mathbf{F}_{qp,s} = -q_{p,s}\alpha_{p,s}\nabla\varphi \tag{3.68}$$

The algorithm for the coupling between the multi-fluid CFD model and the electrostatic model (Rokkam et al. 2010) is as follow:

1. Solve the multi-fluid model equations at every grid point and deduce the volume fraction of the gas and solid phases.

2. Solve the Poisson equation 3.66 for the electric potential using the volume fractions of the gas and solid phases from the previous step and the user-defined specified charges.

3. Evaluate the electrostatic force using the gradient of the electric potential.

4. Add electrostatic force to each of the solid phase momentum equation and repeat the algorithm for the next iteration.

3.3 Triboelectric charging model

3.3.1 Introduction

The particles charges were prescribed in the models presented above. However, particle-particle and wall-particle contact induce a modification of the charges carried on particles. This contact is known as triboelectric charging or tribocharging. Kolehmainen et al. 2016b built electrostatic model presented in the previous work (Kolehmainen et al. 2016) and the triboelectric charging model of Laurentie et al. 2013 into a CFD-DEM model. This section describe the transposing procedure from Lagrangian to Eulerian approach of tribocharging model.

3.3.2 Contact surface

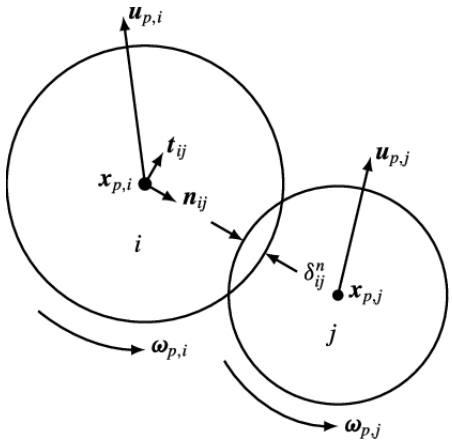

Figure 3.1: Soft sphere collision scheme by Finn et al. 2016

The rate of change of charge q_p carried by particle i is written as (Laurentie et al. 2013; Kolehmainen et al. 2016b):

$$\frac{dq_{pi}}{dt} = -\sum_j \dot{Q}_{ij} \tag{3.69}$$

where $\dot{Q}_{ij}$ denotes the rate of charge transfer from particle i to particle j which is engaged in a collision with particle i at the time instant of interest (t_0):

$$\dot{Q}_{ij} = \begin{cases} \sigma H\left(\frac{dA_{ij}}{dt}\right)\frac{dA_{ij}}{dt}\frac{\varepsilon}{\delta e}\left(\varphi_i - \varphi_j - \mathbf{E}_{i,j}.\frac{\mathbf{d}_{i,j}}{||\mathbf{d}_{i,j}||}\delta.e\right) & \text{if } \left|\mathbf{E}_{i,j}.\frac{\mathbf{d}_{i,j}}{||\mathbf{d}_{i,j}||}\right| < E_b \\ \frac{q_j - q_i}{2}\delta(t - t_0) & \text{otherwise} \end{cases} \tag{3.70}$$

where ε is the permittivity of the medium; H(.) is the Heaviside function; $\delta(t - t_0)$ is Dirac's delta function. E_b is a threshold electric field at which dielectric breakdown would occur in the medium. The Heaviside function is used to stop charge transfer from occurring as particles separate from one another. σ is a correction coefficient which represents the ratio between charge transfer of a real and simulated soft particle. Figure 3.1 gives a schematic draw of the collision between the two particles i and j.

In an Euler-Euler approach, collisions are considered to be instantaneous. Thus, The variation of the collision surface $H(\frac{dA_{ij}}{dt}) * \frac{dA_{ij}}{dt}$ during contact is equal to $\frac{A_{max}}{\tau_o^c}$. where A_{max} is the maximal section of contact during collision and τ_o^c is the collision duration. In this section, the notation is changed: subscript p and q are adopted instead of i and j.

First, a general model is established for bi-disperse case by considering two solid phases p and q and a particle from each. Thus, equations obtained is this section are valid for both monodisperse and bi-disperse case. The expression of the collision section can be written as:

$$A_{max} = 2\pi R^* \delta_{max} \tag{3.71}$$

where $R^* = \frac{R_p R_q}{R_p + R_p}$ and δ^{max} are, respectively, the interpolated radius and the maximum overlap between a particle from the p^{th} solid phase and a particle from the q^{th} solid phase.

By considering the system "particle p + particle q", the force balance acting on a particle from the p^{th} solid phase during collision can be written as:

$$m_p \frac{d^2 \mathbf{r}_p}{dt^2} = \mathbf{F}_{q \to p} \tag{3.72}$$

In order to simplify the notation, subscripts p and q refers to a particle from the p^{th} solid phase and a particle from the q^{th} solid phase respectively.

The overlap between the two colliding particles is expressed by :

$$\delta(t) = R_p + R_q - (\mathbf{r}_q - \mathbf{r}_p) \cdot \mathbf{n}_{pq} \tag{3.73}$$

where $\mathbf{r}_p$ and $\mathbf{r}_q$ are the displacement vectors of particle p and q respectively. $\mathbf{n}_{pq}$ is the normal vector to the collision surface in the direction $p \to q$.

Assuming that the normal $\mathbf{n}_{pq}$ does not change during collision, the overlap is derived twice and substituted in the force balance equation 3.72. Which gives:

$$\frac{d^2\delta}{dt^2} = \left(\frac{d^2 \mathbf{r_p}}{dt^2} - \frac{d^2 \mathbf{r_q}}{dt^2} \right) \cdot \mathbf{n_{pq}} \tag{3.74}$$

Then:

$$\frac{d^2\delta}{dt^2} = \left(\frac{\mathbf{F}_{q \to p}}{m_p} - \frac{\mathbf{F}_{p \to q}}{m_q} \right) \cdot \mathbf{n}_{pq} \tag{3.75}$$

The inter-particle force can be modeled through a spring model; the linear model is expressed as:

$$\mathbf{F}_{q\to p}\cdot\mathbf{n_{pq}} = \underbrace{-k\delta}_{\text{elastic deformation}} \underbrace{-\eta\frac{d\delta}{dt}}_{\text{plastic deformation}} \tag{3.76}$$

By substituting in equation 3.75 and adding initial conditions, the overlap variation versus time is then described by the following differential equation:

$$\begin{cases} \dfrac{d^2\delta}{dt^2}+\dfrac{\eta}{m_p^*}\dfrac{d\delta}{dt}+\dfrac{k}{m_p^*}\delta &= 0 \\ \delta(0) &= 0 \\ \dfrac{d\delta}{dt}(0) &= V_{r0,pq} \end{cases}$$

where $\frac{1}{m_p^*}=\left(\frac{1}{m_p}+\frac{1}{m_q}\right)$ is the so-called reduced mass, k is the spring stiffness and η is the damping coefficient. The initial conditions of the o.d.e. indicates that the contact occurs at t=0 and the relative velocity between the particle p and q at the contact is $V_{r0,pq}$. As a first approximation, the contact between particles is considered to be elastic ($\eta = 0$). The solution of the differential equation can be written in the form:

$$\delta(t) = Acos(\omega t) + Bsin(\omega t) \tag{3.77}$$

where $\omega=\sqrt{\frac{k}{m_p^*}}$. Considering the initial conditions, the final solution is:

$$\delta(t) = \frac{V_{r0,pq}}{\omega}sin(\omega t) \tag{3.78}$$

δ_{max}^{linear} is then:

$$\delta_{max}^{linear} = V_{r0,pq}\sqrt{\frac{m_p^*}{k}} \tag{3.79}$$

In order to be more accurate, the collision is modeled trough a Hertzian contact (Johnson 1985). Equation 3.76 becomes:

$$\mathbf{F}_{q\to p}\cdot\mathbf{n_{pq}} = -k\delta^{3/2}-\eta\frac{d\delta}{dt} \tag{3.80}$$

where k the spring stiffness is expressed as a function of effective diameterR^* and effective Young modulus Y^*:

$$k = \frac{4}{3}\sqrt{R^*}Y^* \tag{3.81}$$

$$\frac{1}{Y^*} = \frac{1-\nu_p^2}{Y_p^*} + \frac{1-\nu_q^2}{Y_q^*} \tag{3.82}$$

where ν is the Poisson coefficient. The o.d.e. 3.3.2 becomes a non linear differential equation. By considering elastic collisions, it is written as:

$$\begin{cases} \dfrac{d^2\delta}{dt^2} + \dfrac{k}{m_p^*}\delta^{3/2} &= 0 \\ \delta(0) &= 0 \\ \dfrac{d\delta}{dt}(0) &= V_{r0,pq} \end{cases}$$

This differential equation does not have an analytical solution. Still, the maximum overlap can be found by considering:

$$v = \frac{d\delta}{dt} \tag{3.83}$$

$$\frac{d^2\delta}{dt^2} = v\frac{dv}{d\delta} \tag{3.84}$$

$$vdv = -\frac{k}{m_p^*}\delta^{3/2}d\delta \tag{3.85}$$

$$\frac{1}{2}\left(v^2 - V_{r0,pq}^2\right) = -\frac{2}{5}\frac{k}{m_p^*}\delta^{5/2} \tag{3.86}$$

when $\delta = \delta_{max}$, $v = 0$. Which gives:

$$\delta_{max} = \left(\frac{5}{4}\frac{m_p^*}{k}\right)^{2/5} V_{r0,pq}^{4/5} \tag{3.87}$$

Substituting with equation 3.81, the final expression of surface contact is:

$$A_{max} = 2\pi r^* \left(\frac{15m_p^*}{16Y^*\sqrt{r^*}}\right)^{2/5} \left|\mathbf{V_r}\cdot\mathbf{n_{pq}}\right|^{4/5} \tag{3.88}$$

It is important to note that this work was done before the paper of Kolehmainen et al. 2018. The expression found by authors is:

$$A_{max,kolehmainen} = 2\pi r^* \left(\frac{15m_p^*}{32Y^*\sqrt{r^*}}\right)^{2/5} \left|\mathbf{V_r}\cdot\mathbf{n_{pq}}\right|^{4/5} \tag{3.89}$$

where $\left|\mathbf{V_r}\cdot\mathbf{n_{pq}}\right|$ is the relative velocity projected on the normal vector of the surface contact between the colliding particles.

3.3.3 Mean charge transport equation

Based on Chapman-Enskog equation (Chapman and Cowling 1970), a transport equation of the mean charge on the solid phase p is deduced:

$$n_p m_p \frac{\partial \chi_p^c}{\partial t} + n_p m_p U_{p,i} \frac{\partial \chi_p^c}{\partial x_i} + \frac{\partial n_p m_p \left\langle \zeta_p' c_{p,i}' \right\rangle}{\partial x_i} = \mathcal{C}\left(\zeta_p\right) \tag{3.90}$$

where $\chi_p^c = \dfrac{\left\langle q_p \right\rangle}{m_p}$ is the average charge per mass unit. α_p, ρ_p, n_p, m_p are respectively volume fraction, density, number of particles per mass unit and mass of a particle of the p^{th} solid phase. $U_{p,i}$ is the i^{th} component of the p^{th} phase velocity. From this equation, two terms need to be closed: the last term on the left hand side accounts for the correlation between the charge and the velocity $\left\langle \zeta_p' c_{p,i}' \right\rangle$ and the right hand side represents the mean rate of change for the charge due to collisions $\mathcal{C}\left(\zeta_p\right)$.

Montilla et al. 2019 calculated the term $\mathcal{C}\left(\zeta_p\right)$ based on the formulation proposed by Jenkins and Savage 1983. They also modeled the charge velocity correlation assuming the following hypothesis:

- Steady state.
- The third order moment $\left\langle \zeta_p' c_{p,i}' c_{p,j}' \right\rangle$ is neglected.
- The charge variance $\left\langle \zeta_p' \zeta_p' \right\rangle$ is neglected.
- No particle velocity gradient.

Leading to a closed mean electric charge equation:

$$\begin{aligned} n_p m_p \frac{\partial \chi_p^c}{\partial t} + n_p m_p U_{pi} \frac{\partial \chi_p^c}{\partial x_i} = &- \frac{\partial}{\partial x_i}\left[m_p \left(\sigma_p^{\text{coll}} + \left(1+\eta_{\text{coll}}\right) \sigma_p^{\text{kin}} \right) E_i \right] \\ &+ \frac{\partial}{\partial x_i}\left[n_p m_p \left(D_p^{\text{coll}} + \left(1+\eta_{\text{coll}}\right) D_p^{\text{kin}} \right) \frac{\partial \chi_p^c}{\partial x_i} \right] \end{aligned} \tag{3.91}$$

$$D_p^{\text{coll}} = d_p^4 \frac{\beta}{\gamma} g_0 n_p \left(\Theta_p\right)^{9/10} \Upsilon^{(1.1)} \tag{3.92}$$

$$\sigma_p^{\text{coll}} = d_p^3 \beta g_0 n_p^2 \left(\Theta_p\right)^{9/10} \Upsilon^{(1.2)} \tag{3.93}$$

$$D_p^{\text{kin}} = \frac{\Theta_p + \Upsilon^{(2.1)} \tau_\zeta^{-1} d_p \Theta_p}{\frac{1}{3}\left(1+e_c\right)\tau_c^{-1} + \overline{\tau_{gp}^F}^{-1} + \frac{2}{5}\left(3-e_c\right)\tau_\zeta^{-1}} \tag{3.94}$$

$$\sigma_p^{\text{kin}} = \frac{e_c \Upsilon^{(2.2)} d_p^2 \beta g_0 \left(\Theta_p\right)^{7/5} n_p}{\frac{1}{3}\left(1+e_c\right)\tau_c^{-1} + \overline{\tau_{gp}^F}^{-1} + \frac{2}{5}\left(3-e_c\right)\tau_\xi^{-1}} \tag{3.95}$$

$$\eta_{\text{coll}} = \frac{3}{2} d_p^3 \frac{\beta}{\gamma} g_0 n_p \left(\Theta_p\right)^{2/5} \Upsilon^{(2.2)} \tag{3.96}$$

$$\beta = \varepsilon_0 \pi d_p \left(\frac{15 m_p}{16 Y \sqrt{\frac{d_p}{2}}} \right)^{2/5} \tag{3.97}$$

$$\gamma = \pi \varepsilon_0 d_p^2 \tag{3.98}$$

Where $\overline{\tau_{gp}^F}$ is the drag force characteristic time:

$$\overline{\tau_{gp}^F} = \left\langle \frac{1}{\tau_{gp}^F} \right\rangle^{-1} \tag{3.99}$$

Where τ_c is the particle collision time:

$$\tau_c = \left(n_p g_0 \pi d_p^2 \sqrt{\frac{16}{\pi} \Theta_p} \right)^{-1} \tag{3.100}$$

And τ_ξ is the charge covariance destruction by collision characteristic time:

$$\tau_\xi = \left(\Upsilon^{(3.1)} d_p^2 \frac{\beta}{\gamma} n_p g_0 \Theta_p^{9/10} \right)^{-1} \tag{3.101}$$

$\Upsilon^{(\cdot)}$ are numerical constant presented as below, where $\Gamma(\cdot)$ is the Gamma function:

$$\Upsilon^{(1.1)} = \frac{2^{57/10} 5}{3^{19/10} 7} \Gamma\left(\frac{12}{5}\right) \Gamma\left(\frac{3}{2}\right) \tag{3.102}$$

$$\Upsilon^{(1.2)} = \frac{2^{57/10} 5}{3^{19/10} 7} \Gamma\left(\frac{3}{2}\right) \Gamma\left(\frac{12}{5}\right) \tag{3.103}$$

$$\Upsilon^{(2.2)} = \frac{2^{14/5} 5}{3 \cdot 19} \Gamma\left(\frac{29}{10}\right) \Gamma\left(\frac{3}{2}\right) \tag{3.104}$$

$$\Upsilon^{(3.1)} = \frac{2^{24/5}}{7} \Gamma\left(\frac{24}{10}\right) \Gamma\left(\frac{3}{2}\right) \tag{3.105}$$

$$\Upsilon^{(2.1)} = \frac{\Upsilon^{(2.2)}}{\Upsilon^{(3.1)}} \tag{3.106}$$

The first term in the r.h.s. of equation 3.91 represents the triboconductivity effect, it indicates that, when two particles are in contact, the global electric field will force a redistribution of their electric charge that follows the global electric field. It is characterized by the parameter σ_p and has two contributions: a collisional part σ_p^{coll} and a kinetic part σ_p^{kin}. It originates from the charge-velocity correlation. The second term accounts for the dispersion phenomenon: D_p^{coll} is the collisional dispersion coefficient accounting for the particle charge redistribution due to particle-particle collisions. D_p^{kin} is the kinetic dispersion coefficient, it accounts for the dispersion of the electric charge due to the random motion of particles. This coefficient originates from the charge-velocity correlation. σ_p^{coll} and σ_p^{kin} are the triboconductivity coefficient and representing the charge transport generated by the electric field when two particles are in contact.

Equation 3.94 reveals three main limiting mechanisms for the kinetic dispersion: the particle-particle collision, the drag force and the particle charge transfer (Montilla et al. 2019). When there are many collisions (small values of τ_c) the mean free path of particles is very short which prevents the particles from traveling long distances, diminishing the particles dispersion. The second mechanism is the drag force ($\overline{\tau_p}$). Indeed, the presence of a surrounding fluid slows down the particles. This imposes a characteristic distance that a single particle can travel before being stopped due to the drag force. While increasing the effect of the drag force this distance will be smaller, therefore, reducing the electric charge dispersion. Finally, the third term limiting the dispersion phenomenon is due to the electric charge transfer. During its random motion, a single particle will encounter other particles and will transfer some of its electric charge to them. Therefore, the particle will gradually lose the information about its initial electric charge value. Hence, the electric charge dispersion will be impacted negatively. This effect can be characterized by the characteristic time scale of the destruction of the electric charge covariance ($\tau_{\tilde{\xi}}$). Indeed, the destruction of the charge covariance and the decorrelation of the charge measured along the particle trajectory are both due to the same mechanism of exchange of charge between particles during collisions. This extra term is a new contribution that has not been remarked in previous works. In conclusion, the dispersion coefficient might be limited by three different factors: particle-particle collisions, drag force and charge transfer during a collision. And the phenomenon with the smallest characteristic time will be the limiting factor.

In this study, the triboconductivity effect is not taken into account and its effect is not discussed.

3.3.4 Wall boundary conditions

Electric potential

In several simulations in literature, the boundary condition used is zero for the electric potential. The walls are assumed to be grounded. This assumption is available for the conducting walls (metal). However, in this study, the walls are made up from Plexiglas. Due to the numerous collisions, the walls acquire a charge with opposite sign comparing to the particles. Since the material is not conductive, the charge is not uniformly distributed on the wall surface. A dynamic boundary condition could be used, which is a function of local collisions between particles and the wall. Sippola et al. 2018 proposed a formula in a CFD-DEM simulation of polyethylene particles in soda-lime column by discretizing the Poisson equation. Authors simulated a rectangular canal (fluidization domain) inside a cylindrical geometry. The boundary condition between at the canal wall was given by :

$$\varphi_f \left(\frac{\varepsilon_B}{d_B} + \frac{\varepsilon_A}{d_A} \right) = \varepsilon_B \frac{\phi_B}{d_B} + \varepsilon_A \frac{\phi_A}{d_A} + \sigma_f \tag{3.107}$$

where φ_f is the potential at the boundary face, φ_A and φ_B are the potentials at the respective cell centers, d_A and d_B are the perpendicular distances from the face to the respective cell centers and σ_f is the free surface charge density on the face (see figure 3.2). ε_A and ε_B are the electric permittivities in medium A and B in the immediate vicinity to the point considered. The potential outside the canal is set to zero.

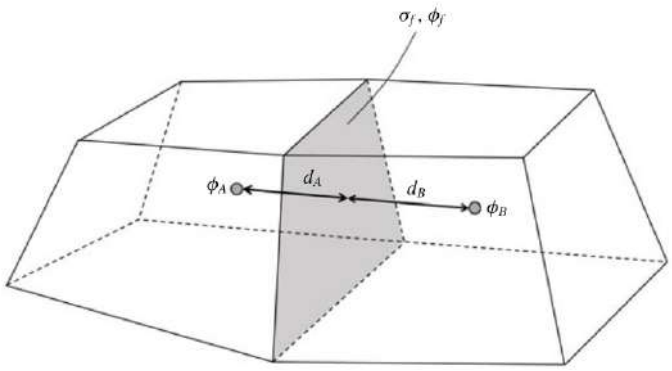

Figure 3.2: Common face of cells A and B at a region interface
(Sippola et al. 2018)

In this study, simulated particles are glass beads. The work function of SiO_2, the main chemical component of glass beads, is $\approx$ 5eV and the one of Plexiglas is $\approx$ 3.5 eV (Gupta et al. 1993). So, the column walls are positively charged and the particles are negatively charged. Negative charges were also measured experimentally, except for small particles (refer to chapter 4). Since the electrostatic force is calculated from the electric potential gradient (equation 3.68), using zero potential boundary condition reduces the magnitude of the electrostatic force but does not change the segregation pattern. Therefore, in all simulations, zero potential condition is used. However, this condition remains valid only for negatively charged particles.

Electric charge

In order to set boundary conditions, the charge velocity flux need to be calculated. The general expression of the charge flux at the wall is:

$$n_p \left\langle \chi_p u_p \right\rangle = \iint_{D^+} f_p^+ \zeta_p^+ |\mathbf{c}_p^+ \cdot \mathbf{n}| dc_p^+ d\zeta_p^+ - \iint_{D^-} f_p^- \zeta_p^- |\mathbf{c}_\mathbf{p}^- \cdot \mathbf{n}| d\mathbf{c}_\mathbf{p}^- d\zeta_p^- \tag{3.108}$$

where: $f_p = f_p\left(\mathbf{x_p}, \mathbf{c_p}, \zeta_p, t\right)$. Superscripts $^-$ and $^+$ refers to the value before and the value after wall collision respectively (see figure 3.3). The relationship between f_p^- and f_p^+ can be modeled through Sakiz and Simonin 1999 formulation:

$$\begin{aligned} &f_p^+\left(\mathbf{x_p}, \mathbf{c}_\mathbf{p}^+, \zeta_p^+, t\right) \zeta_p^+ |\mathbf{c}_\mathbf{p}^+ \cdot \mathbf{n}| = \\ &\iint_{D^-} f_p^-\left(\mathbf{x_p}, \mathbf{c}_\mathbf{p}^-, \zeta_p^-, t\right) \zeta_p^- |\mathbf{c}_\mathbf{p}^- \cdot \mathbf{n}| R(\zeta_p^- \to \zeta_p^+, \mathbf{c}_\mathbf{p}^- \to \mathbf{c}_\mathbf{p}^+) d\mathbf{c}_\mathbf{p}^- d\zeta_p^- \end{aligned} \tag{3.109}$$

where $R(\zeta_p^- \to \zeta_p^+, \mathbf{c}_\mathbf{p}^- \to \mathbf{c}_\mathbf{p}^+)$ refers to the probability for an incident particle with a velocity $\mathbf{c}_\mathbf{p}^-$ and charge ζ_p^- to be reflected with a velocity $\mathbf{c}_\mathbf{p}^+$ and charge ζ_p^+ in the range $c_p^+ d\zeta_p^+$.

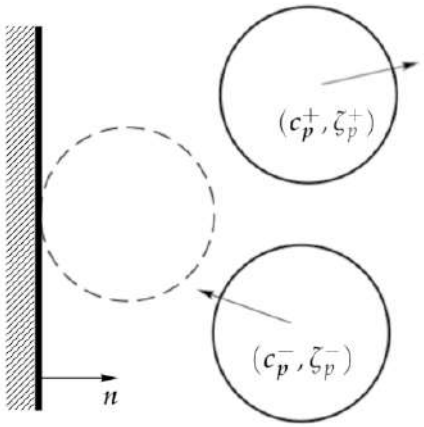

Figure 3.3: Schematic design of wall-particle collision

In all this study, it is assumed that there is no particle deposit on the wall. By considering an isomorphism relating the quantities after to collision to those before:

$$\phi : \begin{cases} \mathcal{D}^- \to \mathcal{D}^+ \\ (\mathbf{c}_\mathbf{p}^-, \zeta_p^-) \mapsto (\mathbf{c}_\mathbf{p}^+, \zeta_p^+) = \phi(\mathbf{c}_\mathbf{p}^-, \zeta_p^-) \end{cases} \tag{3.110}$$

Then:

$$R(\zeta_p^- \to \zeta_p^+, \mathbf{c}_\mathbf{p}^- \to \mathbf{c}_\mathbf{p}^+) = \delta\left(\phi(\mathbf{c}_\mathbf{p}^-, \zeta_p^-) - (\mathbf{c}_\mathbf{p}^+, \zeta_p^+)\right) \tag{3.111}$$

where $\delta(\cdot)$ is Dirac function.

The next step is to express $\mathbf{c}_\mathbf{p}^+$ and ζ_p^+ as function of $\mathbf{c}_\mathbf{p}^-$ and ζ_p^-. For velocities, it will be assumed that the bouncing is linear in the wall-normal direction, which gives:

$$\mathbf{c}_\mathbf{p}^+ \cdot \mathbf{n} = -e_w \mathbf{c}_\mathbf{p}^- \cdot \mathbf{n} \tag{3.112}$$

where e_w refers to the restitution coefficient after a particle-wall collision. This leads to a relation between f_p^+ and f_p^- (Sakiz and Simonin 1999):

$$f_p^+ \left(\mathbf{c}_\mathbf{p}^+, \zeta_p^+\right) = \frac{1}{e_w J_\phi} f_p^- \left(\phi^{-1}(\mathbf{c}_\mathbf{p}^+, \zeta_p^+)\right) \tag{3.113}$$

where J_ϕ is the Jacobian of the function ϕ. In next the remaining parts of this work, unless otherwise stated, wall-particle collision are considered to be elastic and restitution coefficient is $e_w = 1$.

For charge variation, the relationship between ζ_p^+ and ζ_p^- can be written as:

$$\zeta_p^+ = \zeta_p^- + \Delta\zeta_p \tag{3.114}$$

where $\Delta\zeta_p$ is the charge variation during collision. This variation is derived by analogy with equation 3.70:

$$\Delta\zeta_p = \zeta_p^+ - \zeta_p^- = \frac{1}{m_p} A_{max} \varepsilon_0 \left(\frac{\Delta\varphi_{w,p}}{\delta_c} - \mathbf{E}_{wall} \cdot \mathbf{n}\right) \tag{3.115}$$

where $\Delta\varphi_{w,p}$ is the difference of work function between the wall and the particle expressed in eV (electron-Volt). It refers to the energy needed to extract an electron from the upper electron layer of the atom. δ_c is a cut-off distance beyond which the charge transfer stops. Its value is taken from literature $\delta_c = 10^{-7}$ m. $\mathbf{E}_{wall} \cdot \mathbf{n}$ is the projection of the local electric field at the wall on the normal vector from the wall to the particle. It can be calculated as the sum of the electric field created by the wall and the one created by the particle. The wall can be considered as an infinite plane, carrying a charge per surface unit (σ_{wall}). The particle is considered as a point charge (ζ_p^-) located at the center of the particle and the electric field is calculated at the surface of particle. This leads to:

$$\mathbf{E}_{wall} \cdot \mathbf{n} = \frac{\zeta_p^- m_p}{\pi \varepsilon_0 d_p^2} - \frac{\sigma_{wall}}{2\varepsilon_0} \tag{3.116}$$

By substituting in equation 3.115:

$$\zeta_p^+ = K_{1|c_p^-} \zeta_p^- + K_{2|c_p^-} \tag{3.117}$$

$$K_{1|c_p^-} = \left(1 - \frac{A_{max|c_p^-}}{\pi d_p^2}\right) \tag{3.118}$$

$$K_{2|c_p^-} = \frac{\varepsilon_0 A_{max|c_p^-}}{m_p}\left(\frac{\Delta\varphi_{w,p}}{\delta_c} + \frac{\sigma_{wall}}{2\varepsilon_0}\right) \tag{3.119}$$

The surface contact area is calculated by analogy to the equation 3.89. The wall is considered as a particle with infinite diameter, infinite mass and zero velocity. Which leads to:

$$A_{max} = \pi d_p \left(\frac{15 m_p}{16 Y^* \sqrt{\frac{d_p}{2}}}\right)^{2/5} |\mathbf{c_p^-} \cdot \mathbf{n}|^{4/5} \tag{3.120}$$

where Y^* is the effective Young modulus between wall and particles. It is calculated as follows:

$$\frac{1}{Y^*} = \frac{1-\nu_p^2}{Y_p} + \frac{1-\nu_{wall}^2}{Y_{wall}} \tag{3.121}$$

where ν and Y are Poisson coefficient and Young modulus respectively. In order to simplify notation, A_{max} and $K_{2|c_p^-}$ are written as:

$$A_{max} = \pi d_p \beta' |\mathbf{c_p^-} \cdot \mathbf{n}|^{4/5} \tag{3.122}$$

$$\beta' = \left(\frac{15 m_p}{16 Y^* \sqrt{\frac{d_p}{2}}}\right)^{2/5} \tag{3.123}$$

$$\begin{aligned} K_{2|c_p^-} &= \frac{\varepsilon_0 \pi d_p \beta'}{m_p} |\mathbf{c_p^-} \cdot \mathbf{n}|^{4/5} \left(\frac{\Delta\varphi_{w,p}}{\delta_c} + \frac{\sigma_{wall}}{2\varepsilon_0}\right) \\ &= \gamma' \beta' |\mathbf{c_p^-} \cdot \mathbf{n}|^{4/5} \end{aligned} \tag{3.124}$$

By substituting equations 3.113, 3.112 and 3.114 in the expression of the flux at wall (equation 3.108):

$$\begin{aligned} n_p \langle \chi_p u_p \rangle = &\iint_{\mathbf{c_p^-}, \zeta_p^- \in D^-} \left(K_{1|c_p^-} \zeta_p^- + K_{2|c_p^-}\right) |\mathbf{c_p^-} \cdot \mathbf{n}| f_p^- d\mathbf{c_p^-} d\zeta_p^- \\ &- \iint_{\mathbf{c_p^-}, \zeta_p^- \in D^-} \zeta_p^- |\mathbf{c_p^-} \cdot \mathbf{n}| f_p^- d\mathbf{c_p^-} d\zeta_p^- \end{aligned} \tag{3.125}$$

Then:

$$\begin{aligned} n_p \left\langle \chi_p u_p \right\rangle = & \iint_{\mathbf{c}_\mathbf{p}^-, \zeta_p^- \in D^-} \left(K_{1|c_p^-} - 1 \right) \zeta_p^- |\mathbf{c}_\mathbf{p}^- \cdot \mathbf{n}| f_p^- d\mathbf{c}_\mathbf{p}^- d\zeta_p^- \\ & + \iint_{\mathbf{c}_\mathbf{p}^-, \zeta_p^- \in D^-} K_{2|c_p^-} |\mathbf{c}_\mathbf{p}^- \cdot \mathbf{n}| f_p^- d\mathbf{c}_\mathbf{p}^- d\zeta_p^- \end{aligned} \tag{3.126}$$

Substituting $K_{1|c_p^-}$ and $K_{2|c_p^-}$ gives:

$$\begin{aligned} n_p \left\langle \chi_p u_p \right\rangle = & \iint_{\mathbf{c}_\mathbf{p}^-, \zeta_p^- \in D^-} -\frac{\beta'}{d_p} \zeta_p^- |\mathbf{c}_\mathbf{p}^- \cdot \mathbf{n}|^{9/5} f_p^- d\mathbf{c}_\mathbf{p}^- d\zeta_p^- \\ & + \iint_{\mathbf{c}_\mathbf{p}^-, \zeta_p^- \in D^-} \gamma' \beta' |\mathbf{c}_\mathbf{p}^- \cdot \mathbf{n}|^{9/5} f_p^- d\mathbf{c}_\mathbf{p}^- d\zeta_p^- \end{aligned} \tag{3.127}$$

The probability density f_p^- can be written as:

$$f_p^- = f_{p|\zeta_p^-}^{-*} \left(\mathbf{x}_p, \mathbf{c}_p^-, t \right) g_p^- \left(\mathbf{x}_p, \zeta_p^-, t \right) \tag{3.128}$$

where $f_{p|\zeta_p^-}^*$ is the velocity distribution function conditioned by ζ_p^- and g_p^- is the probability density of charge.

Assuming that ζ_p^- and $\mathbf{c}_p^-$ are uncorrelated, equation 3.128 becomes:

$$f_p^- = f_p^{-*} \left(\mathbf{x}_p, \mathbf{c}_p^-, t \right) g_p^- \left(\mathbf{x}_p, \zeta_p^-, t \right) \tag{3.129}$$

It is important to note that this assmption is done only on the distribution of incident particles. Equation 3.127 becomes:

$$\begin{aligned} n_p \left\langle \chi_p u_p \right\rangle = & -\frac{\beta'}{d_p} \iiint |\mathbf{c}_\mathbf{p}^- \cdot \mathbf{n}|^{9/5} f_p^{-*} \underbrace{\left[\int_{-\infty}^{\infty} \zeta_p^- g_p^-(\zeta_p^-) d\zeta_p^- \right]}_{= \left\langle \chi_p^c \right\rangle^-} d\mathbf{c}_\mathbf{p}^- \\ & + \gamma' \beta' \iiint |\mathbf{c}_\mathbf{p}^- \cdot \mathbf{n}|^{9/5} f_p^{-*} \underbrace{\left[\int_{-\infty}^{\infty} g(\zeta_p^-) d\zeta_p^- \right]}_{=1} d\mathbf{c}_\mathbf{p}^- \end{aligned} \tag{3.130}$$

Besides, the particle velocity distribution is assumed to be a Maxwellian (Gaussian) distribution (Sakiz and Simonin 1999):

$$f_p^{-*}(\mathbf{c}_\mathbf{p}) = \frac{n_p^-}{\left(2\pi\Theta_p\right)^{3/2}} e^{-\frac{(c_p)^2}{\Theta_p}} = \Pi_{i=1}^3 \frac{n_p^-}{\sqrt{2\pi\Theta_p}} e^{-\frac{(c_{p,i})^2}{\Theta_p}} \tag{3.131}$$

Let the axis of the integration be in a reference where one of the axis is parallel to the normal vector $\mathbf{n}$, for example y. The integrals over the component x and z are equal to 1. Thus, the probability density is considered to be:

$$f_{p,n}^{-}(\mathbf{c}_{\mathbf{p}}^{-} \cdot \mathbf{n}) = \frac{n_p^{-}}{\sqrt{2\pi\Theta_p}} e^{-\frac{\left(\mathbf{c}_{\mathbf{p}}^{-} \cdot \mathbf{n}\right)^2}{\Theta_p}} \tag{3.132}$$

The integrals are performed from $-\infty$ to 0 (all possible values $\mathbf{c}_{\mathbf{p}}^{-} \cdot \mathbf{n}$). Since the function $t \mapsto t^{9/5} e^{\frac{-t^2}{\Theta_p}}$ is an odd function, the following equality is obtained:

$$\int_{-\infty}^{0} t^{9/5} e^{\frac{-t^2}{\Theta_p}} dt = \int_{0}^{\infty} t^{9/5} e^{\frac{-t^2}{\Theta_p}} dt \tag{3.133}$$

By substituting in equation 3.130:

$$n_p \left\langle \chi_p u_p \right\rangle = \frac{\beta'}{d_p} \left(- \left\langle \chi_p^c \right\rangle^{-} + \gamma' d_p \right) \frac{n_p^{-}}{\sqrt{2\pi\Theta_p}} \int_{0}^{\infty} t^{9/5} e^{\frac{-t^2}{\Theta_p}} dt \tag{3.134}$$

By performing integrals, the final expression of charge flux at the wall is:

$$n_p \left\langle \chi_p u_p \right\rangle = n_p^{-} \frac{\beta'}{d_p} \frac{\Gamma\left(\frac{2}{5}\right) \Theta^{\frac{9}{10}}}{5\sqrt{2}\sqrt{\pi}} \left(- \left\langle \zeta_p \right\rangle^{-} + \gamma' d_p \right) \tag{3.135}$$

where $\Gamma(\cdot)$ is the gamma function. Since wall-particle collisions are assumed to be elastic, $n_p = 2n_p^{-}$. Now, replacing A_1 and A_2:

$$n_p \left\langle \chi_p u_p \right\rangle = \frac{n_p}{2} \Upsilon^{bc} \left(\frac{\rho_p}{Y^*} \right)^{\frac{2}{5}} \Theta^{\frac{9}{10}} \left(\frac{\pi d_p^2}{m_p} \varepsilon_0 \left(\frac{\Delta\varphi_{w,p}}{\delta_c} + \frac{\sigma_{wall}}{2\varepsilon_0} \right) - \left\langle \zeta_p \right\rangle^{-} \right) \tag{3.136}$$

$$\Upsilon^{bc} = \frac{\Gamma\left(\frac{2}{5}\right)}{5\sqrt{2}\sqrt{\pi}} \left(\frac{5\pi}{16\sqrt{2}} \right)^{2/5} \tag{3.137}$$

3.3.5 Equilibrium charge

In the Lagrangian approach, Kolehmainen et al. 2016b considered that the maximum charge that a particle can acquire is estimated by considering the interaction of an isolated particle with the wall and setting the local electric field term equal to the work function difference term. We refer to this charge as the equilibrium charge:

$$q_{eq,Kolehmainen} = \frac{1}{2}\frac{\pi\varepsilon_0}{\delta_c}\Delta\varphi_{w,p}d_p^2 \tag{3.138}$$

this equilibrium charge is obtained for conducting walls ($\sigma_{wall} = 0$). In the case of non conducting walls, the charge of the wall need to be taken into account.

In the Eulerian approach mentioned above, the charge flux obtained in equation 3.136 is a form of relaxation, where the flux tends to bring the charge back to an equilibrium value, with a given velocity:

$$n_p \left\langle \chi_p u_p \right\rangle = n_p \underbrace{\frac{\Upsilon^{bc}}{2}\left(\frac{\rho_p}{Y^*}\right)^{\frac{2}{5}}\Theta^{\frac{9}{10}}}_{\text{charging velocity}} \left(\underbrace{\frac{\pi d_p^2}{m_p}\varepsilon_0\left(\frac{\Delta\varphi_{w,p}}{\delta_c} + \frac{\sigma_{wall}}{2\varepsilon_0}\right)}_{\text{equilibrium charge}} - \left\langle \zeta_p \right\rangle^- \right) \tag{3.139}$$

Since this work presents also experimental results of the total charge per mass unit of gas-solid fluidized bed, this experimental measure will be considered as the equilibrium charge.

3.4 Orders of magnitude of characteristic times

In order to have an idea on the time needed for the bed charge to reach the equilibrium charge, a characteristic time is deduced from equation 3.139. In fact, the charge flux characterizes the charge per mass unit transfered to from the wall to the bed per surface unit per second ($C \cdot kg^{-1} \cdot m^{-2} \cdot s^{-1}$). Now, the characteristic time can be estimated by:

$$\frac{1}{\tau_{Q,wall}} = \alpha_p \frac{S_{wall}}{V_{bed}} \frac{\mathrm{Y}^{bc}}{2} \left(\frac{\rho_p}{Y^*}\right)^{\frac{2}{5}} \Theta^{\frac{9}{10}} \tag{3.140}$$

where S_{wall} is the wall surface and V_{bed} is the bed volume.

On the other hand, the diffusion characteristic time is given by:

$$\frac{1}{\tau_D} = \frac{D_p^{\mathrm{coll}} + (1 + \eta_{\mathrm{coll}})\, D_p^{\mathrm{kin}}}{L^2} \tag{3.141}$$

where L is the characteristic length of the domain. An estimation of this two characteristic times is performed for the experimental setup dimension and the medium glass beads materials. The values of Young modulus and Poisson coefficient for glass beads were determined by Tang et al. 2019. The parameters are presented in table 3.2. Figure 3.4a presents the estimation of the two characteristic times versus the volume fraction. The figure shows that the time needed to reach equilibrium charge using the model presented above is very high $\approx 10^7$ seconds. Besides, the diffusion phenomenon also slow ($\approx 10^5$ seconds). This indicates that the model presented above cannot represent the charge transfer in fluidized bed.

Table 3.2: Parameters for characteristic times estimation

Description	Value
Particle density (kg/m^3)	2476
Granular temperature (m^2/s^2)	1×10^{-5}
Particle diameter (μm)	267
Young Modulus (GPa)	46.2
Poisson coefficient	0.245
Characteristic length (m)	0.05

In CFD DEM simulations, authors use the soft spheres for simulations then add a corrective coefficient (Kolehmainen et al. 2016b; Kolehmainen et al. 2018; Sippola et al. 2018). Figure 3.4b shows an estimation of the characteristic times for soft sphere using the simulation parameters of Kolehmainen et al. 2018 presented in table 3.3. The figure shows that, even for this value of Young modulus, the model still not representing the real case ($\approx$ 20 min) found in experimental results. An alternative model is discussed in Chapter 5 to match with the experimental results.

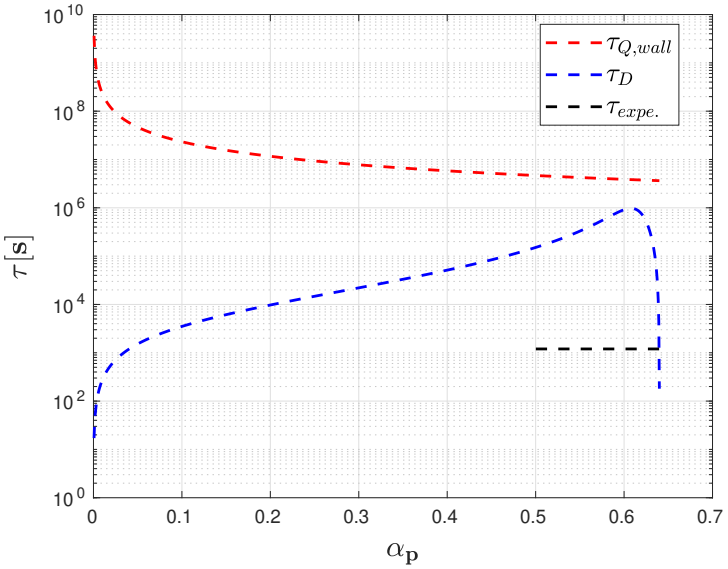

(a) Hard sphere

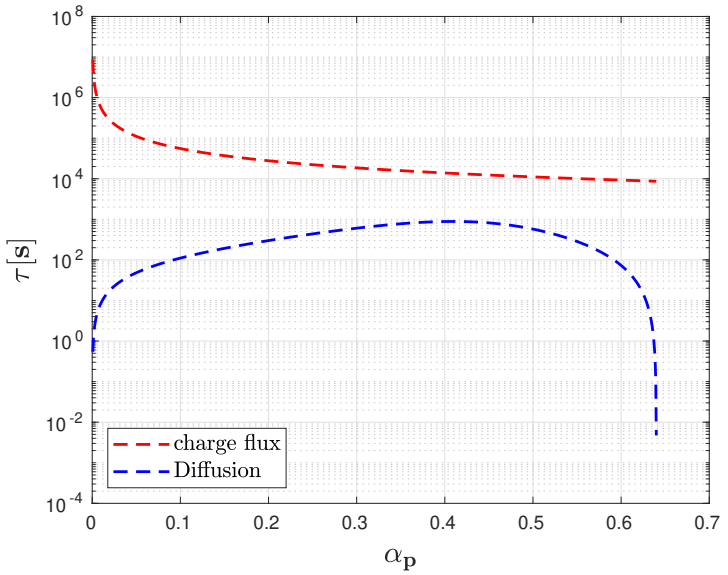

(b) Soft sphere

Figure 3.4: Estimation of characteristic times for diffusion and charge flux

Table 3.3: Parameters for characteristic times estimation for Kolehmainen et al. 2018 case

Description	Value
Particle density (kg/m^3)	1500
Granular temperature (m^2/s^2)	1×10^{-2}
Particle diameter (μm)	250
Young Modulus (MPa)	0.5
Poisson coefficient	0.42
Characteristic length (m)	$192 d_p$

3.5 Simulation software: NEPTUNE_CFD

3.5.1 Code presentation

The simulation software used in simulation is called NEPTUNE_CFD. It is a computational multiphase flow software developed in the framework of the NEPTUNE project, financially supported by CEA (Commissariat à l'Énergie Atomique), EDF (Electricité e de France), IRSN (Institut de Radioprotection et de Sûreté Nucléaire) and Framatome (ex-Areva NP). The main numerical characteristics of NEPTUNE_CFD V4.01 are unstructured meshes with all types of cell, nonconforming connections, cell-center type finite volume method, calculation of co-localized gradients with reconstruction methods and distributed-memory parallelism by domain decomposition (MPI parallelization). The numerical solver is written in C/C++ language. The code allows to take into account complex phenomena: particle mixture, particle-fluid interaction, particle-particle and particle wall collisions, heat and mass transfers and chemical reactions. It is dedicated for calculating multiphase or multi-field flows, at the local scale and in geometries that may be complex. A brief description is presented in this section. Refer to Neau et al. 2010 for more details. Recently, the code performances were tested on an industrial-scale polydispersed reactive pressurized fluidized bed with a mesh cells of one billion cells (Neau et al. 2019).

3.5.2 Numerical schemes

The partial differential equations are discretized with a second-order centered scheme and the solution is time-advanced by a first-order scheme. The model and the numerical method are adapted to the handling of n-phases (in fact n-fields), including the single phase frame. The algorithm, based on original elliptic fractional step method (see Méchitoua et al. 2003) that leads either to use linear solvers or direct nphas x nphas matrix inversion. The main interest of the method is the so-called "alpha-pressure-energy" step that ensures conservativeness of mass and energy and allows strong interface source term coupling. Mass, momentum and energy equations are coupled with the help of a pressure correction equation, within the iterative "alpha-pressure-energy" step. The algorithm allows density variation according to pressure and enthalpy during the computation.

The momentum balance equations are solved with a semi-implicit method. They are split in fractional steps: explicit balance, velocity implicit increment prediction, "alpha-pressure-energy" implicit increment prediction, final velocity correction. The "alpha-pressure-energy" step stops after the mass conservation sub-step, when the volume conservation holds. The user can adapt the criterion parameter ε_{vol}, but this one remains very severe as it is applied to a maximum value over the whole domain. The standard value of ε_{vol} is 10^{-5}. Because of implicit formulation and three dimensional unstructured meshes, iterative solvers are used: conjugated gradient or bi-conjugate gradient stabilized (bi-cgstab) for the pressure, bi-conjugate gradient stabilized or Jacobi for volume fraction and Jacobi for velocity.

A time-dependent time step is used (computed from Courant and Fourier criteria). The following iterative solvers have been selected: Jacobi for the velocity, conjugated gradient for the pressure and bi-cgstab for the volume fraction. The criterion parameter ε of "Alpha-Pressure" step is fixed to 10^{-6} and the maximum number of cycles into "Alpha-Pressure" step is 50.

For the electrostatic and tribocharging model, the electric potential and the charge are considered as passive scalars. Since the code does not have a direct Poisson solver for equation 3.66, a transport equation is solved for the electric potential by setting the unsteady and the convective term to zero. The diffusion coefficient is set to the relative permittivity of the medium (equation 3.63) and the source term is the right hand of the equation 3.66:

$$\underbrace{\rho_g \frac{\partial \varphi}{\partial t}}_{=0} + \underbrace{\frac{\boldsymbol{\nabla} \cdot (\alpha_g \rho_g U_g \varphi) - \varphi \boldsymbol{\nabla} \cdot (\alpha_g \rho_g U_g)}{\alpha_g}}_{=0} = \frac{\sum_{i=1}^{N_{solids}} q_{pi} \alpha_{pi}}{\varepsilon_0 \alpha_g} + \frac{\boldsymbol{\nabla} \cdot (\alpha_g \rho_g D \boldsymbol{\nabla} \varphi)}{\alpha_g} \tag{3.142}$$

With regards to the tribocharging model, a charge per mass unit is carried as a passive scalar by the solid phase. The solver for scalars is chosen to be Jacobi.

3.5.3 Time averaging

Excluding the pressure and volume fraction variables, all the time-averages are phase-averages, weighted by the volume fraction α_k. For example, the l component of the mean velocity of phase k is calculated for each cell as follows:

$$\overline{U_{k,l}} = \frac{\sum_{i=1}^{ndt} \alpha_k^i U_{k,l}^i \Delta t^i}{\sum_{i=1}^{ndt} \alpha_k^i \Delta t^i} \tag{3.143}$$

where Δt^i is the time step at the iteration i.

3.5.4 Calculation informations

Most of the simulations presented in this work were performed on the HPC resources of the national computational centers of CALMIP under the allocation P11032 and CINES under the allocation gct6938 made by GENCI.

3.5.5 Boundary conditions

Inlet

The inlet conditions are the Dirichlet conditions on the velocities, the volume fractions and the energies. For the gas phase, an inlet mass flux is imposed. For the particles, it is considered as a smooth wall. Therefore, a slip condition for particle velocity and a zero flux for random kinetic energy and flux-particle covariance are imposed. For the electric potential and charge, it is a zero flux condition.

Outlet

The outlet of the fluidized bed is a free outlet. For the electric potential and charge, it is a zero flux condition.

Wall

Wall friction functions are used for the velocities and the turbulence properties of the gas phase. A no-slip condition (adherence) for the velocity and zero flux for particle random kinetic energy are imposed on the dispersed phases, corresponding to elastic bouncing of spherical particle on smooth wall without friction. The electric potential is set to zero at the wall (grounded walls). In the case when tribocharging is taken into account, a flux charge is imposed at the wall (equation 3.136). The value of the facet $\chi_p^{c,fac}$ is calculated as follows:

$$\chi_p^{c,fac} = \frac{\langle \chi_p u_p \rangle_{wall}}{D/\Delta n} + \chi_p^{c,int} \tag{3.144}$$

where $\langle \chi_p u_p \rangle_{wall}$ is the charge flux, D is the diffusion coefficient and Δn is the space step near at the wall (thickness of the neighboring cell). $\chi_p^{c,int}$ is the charge in the neighboring cell.

3.6 Test cases for electrostatic model

Test cases aims to verify the implementation of electrostatic model in NEPTUNE_CFD and the coupling with the multi-fluid model. These test were driven and compared to the works of Rokkam et al. 2010 and Rokkam et al. 2013. This section presents only test cases with prescribed charges. The tribocharging model simulations are presented in chapter 5.

3.6.1 Poisson solver

A test was first carried out on a 0.1 m 2D square domain to verify the Poisson equation solver. A simple equation of the following form is solved:

$$\nabla^2 \varphi = 1 \tag{3.145}$$

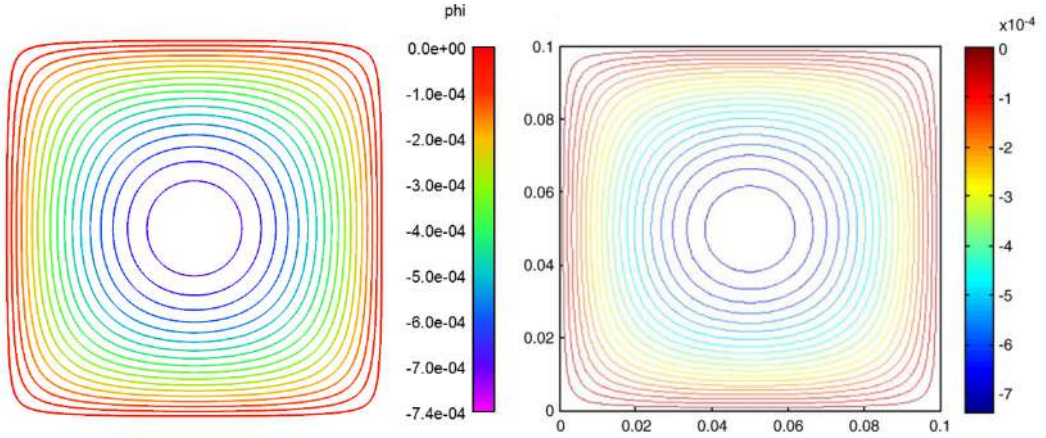

(a) NEPTUNE_CFD solver **(b)** Rokkam et al. 2010 solution

Figure 3.5: Contours of electric potential in volts

Figure 3.5 shows the electric potential contours solved by NEPTUNE_CFD (figure 3.5a) versus Rokkam et al. 2010 solution (figure 3.5b). The contour plots compared well and thus the NEPTUNE_CFD solver can be used to solve for the electric potential.

3.6.2 Coupling algorithm with multi-fluid model

This simulation aims to verify the coupling algorithm mentioned in section 3.2. Simulation was run with a gas phase ($\rho_g = 22.1 \text{kg/m}^3$, $\mu_g = 1.427 \times 10^{-5} \text{Pa} \cdot \text{s}$) and three solid phases with the same density ($\rho_p = 843 \text{kg/m}^3$). Table 3.4 gives diameter, charge and volume fraction of each solid phase. There are no inlets or outlets and no gravitational forces in this test case. The electric potential at the walls is zero. The mesh is a 0.4 m 2D square domain. Simulation was run for 10s.

Figure 3.6 shows instantaneous electric potential and solid volume fraction after t=1s of simulation. The electric potential is zero at the wall and negative in the center. Which means that electric field points from high potential (wall) toward low potential (center). Particles with positive charge will move toward center and negative ones will segregate near the wall. Large particles (solid 3) forms a layer near the wall

Table 3.4: Simulation parameters for coupling algorithm verification

	Small	Medium	Large
Diameter (μm)	523	1176	1751
Volume fraction	0.00453	0.1943	0.31
Charge (C/m3)	0.1081	-0.001	-0.00115

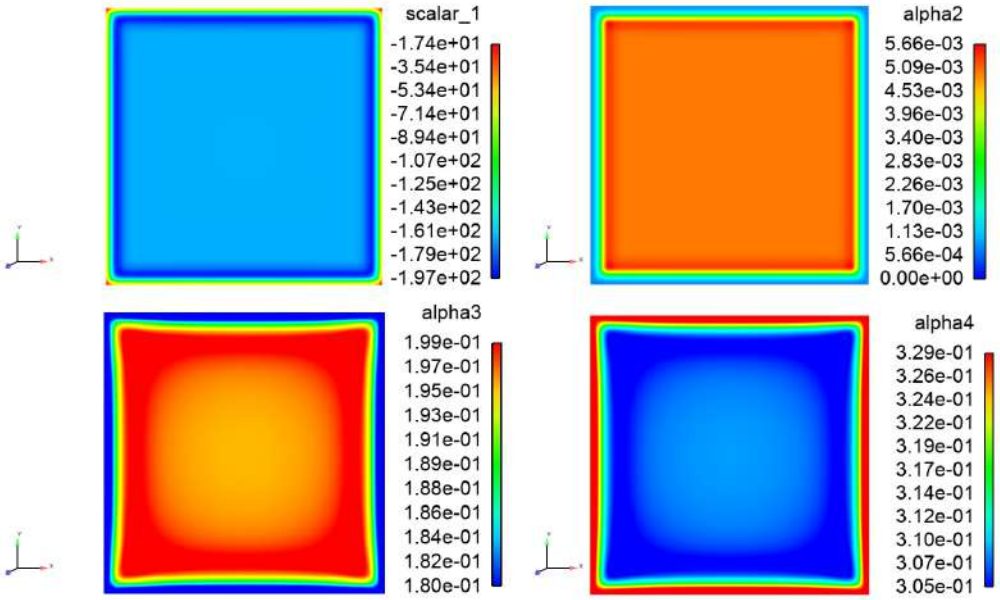

Figure 3.6: Electric potential (scalar_1) and solid volume fraction of solid 1 (alpha2), solid 2 (alpha3) and solid 3 (alpha4) fields at t = 1 s

due to their negative charge and small particles (solid 1) are gathered in the center. Medium particles are sandwiched between small and large ones. Note that the only force acting here is the electrostatic force, thus no segregation happens in the case of zero charge. This simulation shows that electrostatic model is able to capture segregation effects due to electrostatic charge. Thus, the electrostatic model is fully coupled with the multi-fluid one.

3.6.3 Basic electrostatic laws

These tests aims to verify the basic laws of electrostatics: repulsion between particles of the same polarity and attraction between particles of opposite polarity. The multi-fluid CFD model solves for one gas and two solid phases in a square domain. The left half of the square domain is filled with a volume fraction of 0.25 of solid phase 1, and the right half of the square domain with volume fraction of 0.25 of solid phase 2. The density and particle size of both solid phases are the same ($d_p = 500\mu m$, $\rho_p = 843\text{kg/m}^3$). Simulations are run in a 0.4 m 2D square domain with a prescribed charge of $\pm 0.1\text{C/m}^3$. The electric potential at the walls is zero. There are no inlets or outlets and no gravitational forces in this test case.

Figure 3.8 shows the instantaneous volume fraction of solid phases 1 and 2 for the first case. The solid phases are attracted to each other along the centerline. In the second case presented in figure 3.7, the solid phases repel each other since they have the same polarity. These simulations verify that the fully coupled multi-fluid model

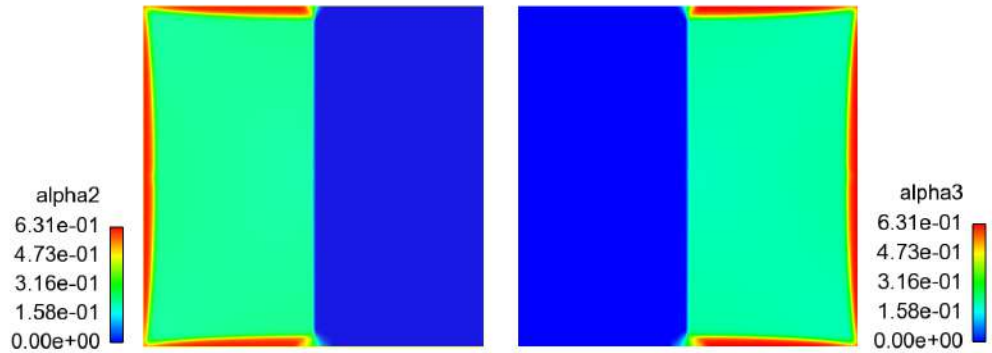

Figure 3.7: Solid volume fraction of solid 1 and solid 2 with same charge polarity ($q_{v,1} = q_{v,2} = 0.1\mathrm{C/m^3}$)

Figure 3.8: Solid volume fraction of solid 1 and solid 2 with opposite charge polarity ($q_{v,1} = -q_{v,2} = -0.1\mathrm{C/m^3}$)

coupled with electrostatic model is able to capture the basic phenomena observed in electrostatics.

3.6.4 Simulation of a lab-scale gas-solid fluidized bed

In this section, a part of Rokkam et al. 2013 work is simulated. Authors simulated experiments of Sowinski et al. 2010 with polyethylene resin. There were two fludization regimes (bubbling and slugging) and three stages simulated. The first one is the fluidized bed. The second one is the settling phase when air is stopped and particles are allowed to settle. And the third one is when the distributor valve is opened and an amount of particles remains adhering to the wall. In this work, simulation were only run for the first stage in bubbling regimes since the goal is only to verify that the model result matches with literature findings. Another objective was to evaluate the computational cost of electrostatic model in a fluidized bed simulation. The mesh geometry was identical to Rokkam et al. 2013 one (height = 1.27 m and diameter = 0.086 m). However, simulation were run in a 3D geometry instead of 2D one.

The simulation consisted of three solid phase: dropped particles which drops after opening the valve gate, wall particles which adhere to the column and fine particles which are entrained. Table 3.5 shows solid phases properties. The gas properties are shown in table 3.6. Simulations were run for 80s and the averaged on the last 70s.

Table 3.5: Solid phases properties of Rokkam et al. 2013 simulation

	Dropped	Wall	Fines
Density (kg/m^3)	843	843	843
Diameter (μm)	712,3	364,4	69,2
Volume fraction	0,6158	0,0137	0,00039
Charge (C/m3)	-0,0005636	-0,0461	0,0175

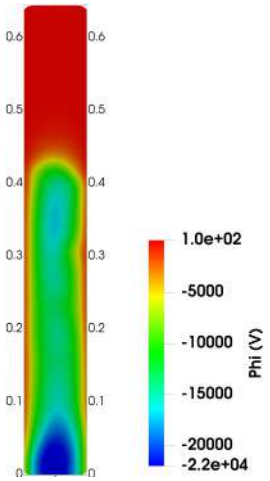

Figure 3.9: Electric potential contours of Rokkam et al. 2013 simulation performed by NEPTUNE_CFD

Table 3.6: Gas phase properties of Rokkam et al. 2013 simulation

Description	Value
Density (kg/m^3)	4.93
Viscosity ($Pa \cdot s$)	1.8×10^{-5}
Velocity (m/s)	$1.5U_{mf} = 0.1965$

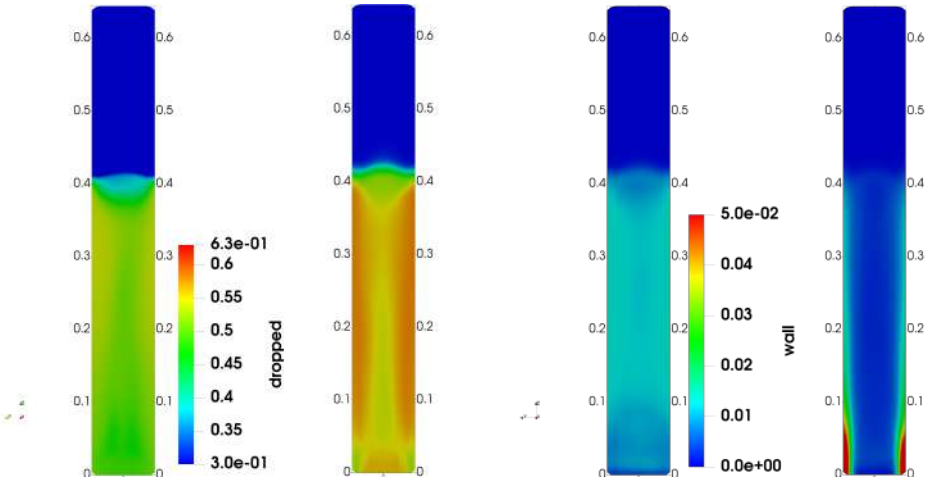

(a) Zero charge **(b)** Charged **(c)** Zero charge **(d)** Charged

Figure 3.10: Volume fraction contours of dropped and wall particles for Rokkam et al. 2013 simulation performed by NEPTUNE_CFD

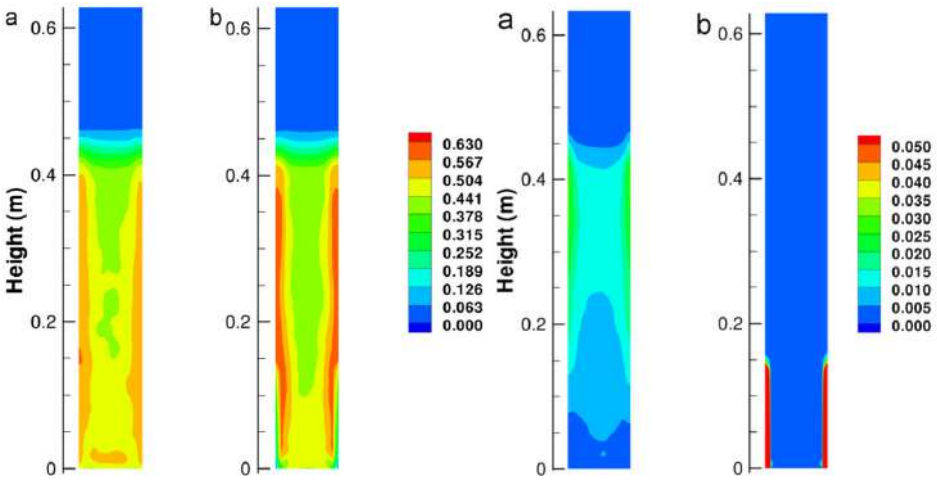

(a) Dropped (a: Zero charge, b:charged) **(b)** Wall (a: Zero charge, b:charged)

Figure 3.11: Results given by Rokkam et al. 2013 for volume fraction contours of dropped and wall particles

Figure 3.9 shows the instantaneous electric potential contours after 80s of simulation. The electric potential in negative below and positive above the bed height. Besides, a strong electric field gradient points from the center to the walls, which makes negatively charged particles moves towards the wall and positively charged particles towards the center (see equation 3.68). Figures 3.10b and 3.10a show the mean volume fraction contours of dropped particles for uncharged and charged case respectively. There is a slight segregation of dropped charged particles towards the wall comparing to the uncharged ones due to the small value of the charge. Figures 3.10c and 3.10d show the mean volume fraction contours of wall particles without and with the charge respectively. The wall particles are more negatively charged than dropped particles, which makes them segregate faster towards the reactor wall. The layer near the wall is thicker at the bottom near the distributor due to lower gas-particle drag and the gravitational force. The same behaviors were reported by Rokkam et al. 2013. shown in figure 3.11. The differences in the contours between the current simulation and the one of the authors are due to two main reasons: the first one is that the simulation software is not the same and does not use exactly the same laws (NEPTUNE_CFD versus ANSYS Fluent). The second one is the geometry, the geometry used here is a 3D mesh whereas the authors geometry is 2D.

To sum up, the electrostatic model was proven to be fully coupled with the multi-fluid model and able to predict the particle segregation due to the presence of electrostatic charges in a lab-scale geometry.

Regarding the calculation cost, the presence of the electrostatic model does not affect it significantly since there is a Poisson equation to be solved and the electrostatic force is encoded in the explicit form.

4 Experimental investigation of electrostatic charges effects

Figures

Tables

4.1 Introduction

This chapter presents experimental results of electrostatic charge effects on hydrodynamics of the fluidized bed depending on operating conditions (gas relative humidity and fluidization velocity) and powder properties. Experiments were performed in the framework of a research master internship by Mohammad Abou Hamoud. Three PSDs of glass beads: small (SGB), medium (MGB) and coarse (CGB) and one of ceramic beads (CB) are used in these experiments. All experiments are performed with 2 kg of mass powder. The first experiments for each PSD were performed to determine the minimum fluidization velocity (refer to subsection 1.1.2 for definition). The next step is estimating the time needed to reach an equilibrium charge depending on gas relative humidity and velocity. It is important to note that the air in the lab network is dried at 5% of relative humidity. Thus, experiments at 5% of RH are performed by setting the RH at 0% in the humidity generator, but it is actually 5%. All experiments are performed at least two or three times in order to verify reproducibility of results. Characteristic diameters of PSDs used in experiments are reported in table 4.1.

Table 4.1: Characteristic diameters of materials used in the experiments

Material	density (kg/m^3)	d_{50} (μm)	d_{sauter} (μm)	Span
CGB	2476	554	545	0.49
MGB	2476	267	264	0.43
SGB	2476	83	81	0.55
CB	3827	100	99	0.48

4.2 Visual effects of electrostatic charges

In the first place, some experiments were performed in order to investigate visually the effects of electrostatics and see how it varies depending on the relative humidity and gas velocity near the walls of column. Fluidized particles were medium glass beads ($d_{50} = 267\mu m$) at different RH and different gas velocity. This study aimed only to have qualitative results and guide the next experiments. Figures 4.1, 4.2 and 4.3 show a preview of the column after stopping the air flow for 2.2, 3.65 and 5.85 U_{mf} respectively. The fluidization lasted for 30 min. The choice of these air flows was based on an estimation of U_{mf} according to Wen and Yu correlation $U_{mf,WY}$ (see equation 1.1) then corrected according to the experimental value found later. From now on, U_{mf} refers to the value found in experiments. Since pictures were only taken by phone camera, the camera position was not exactly the same. The comparison can be done by referring to pressure taps positions. An indicator is put on pictures at 15 cm counting from distributor plate.

The effect of relative humidity for all flows is visible. The amount of particles adhering to wall in the free-board region decreases by increasing RH. Now, comparing the three flow rates at 60% for example, it shows that increasing gas velocity induces an increase of the amount of particles adhering to the wall. One would say that it is trivial that increasing velocity implicates greater Transport Disengagement Height (the height of the projected particles) and then greater amount of wall particles. However, at 75%, where the electrostatic charges are expected to be insignificant,

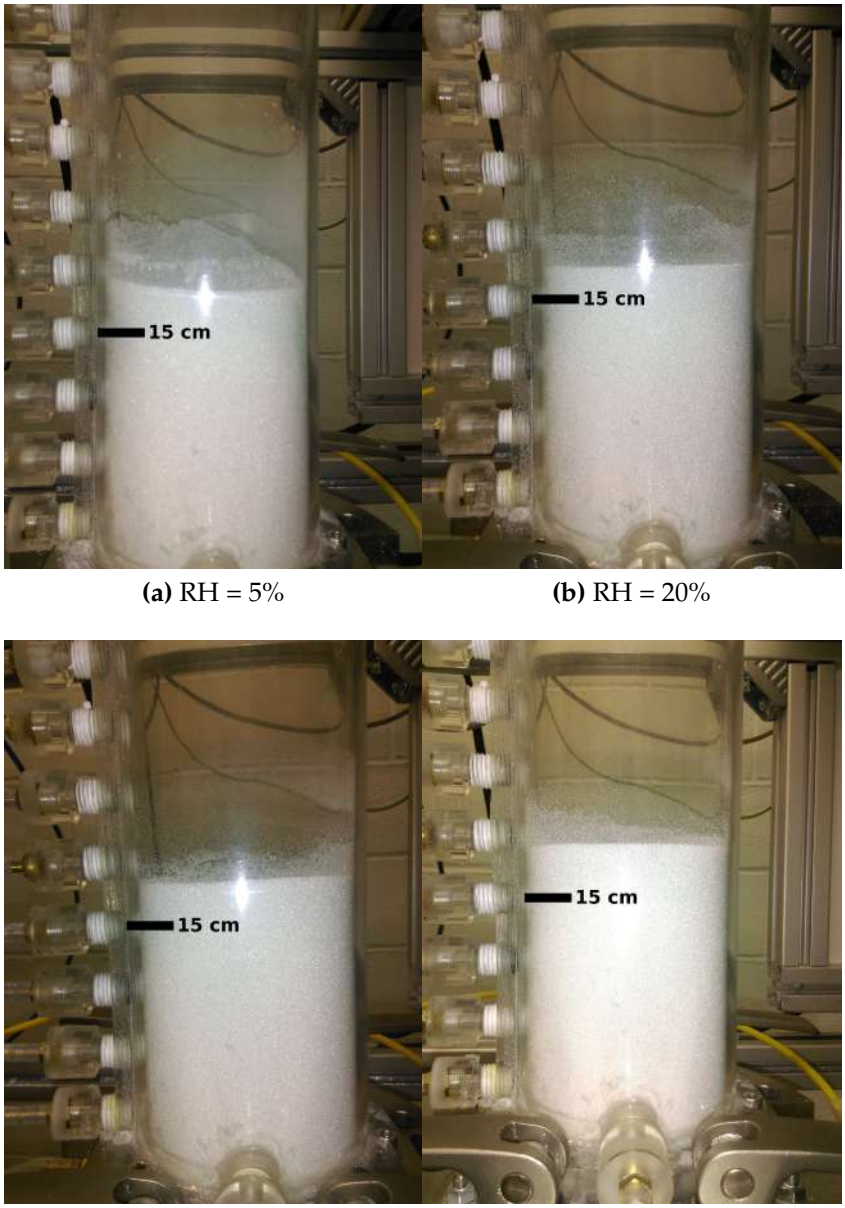

(a) RH = 5% **(b)** RH = 20%

(c) RH = 40% **(d)** RH = 60%

Figure 4.1: Bed preview after stopping fluidization of medium glass beads ($d_{50} = 267\mu m$) at 4.3 Nm^3/h (2.2 U_{mf}) for different relative himidity values (RH)

there are still some particles adhering to the wall for 5.85 U_{mf} comparing to 3.65 U_{mf}.

Although this description have a qualitative character, it shows two main phenomena: the first one is that the charge particles decreases by increasing RH. The second one is that at a given RH, increasing gas velocity induces more charge. Thus, it cannot be assume that the effect of electrostatic charges are non significant at a given RH unless it is related to a range of gas velocity. Later in this chapter, the effect of this two main parameters will be studied quantitatively.

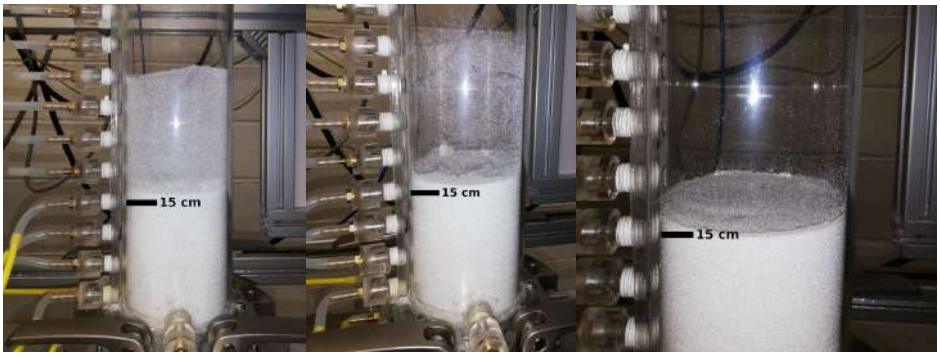

(a) RH = 40% **(b)** RH = 60% **(c)** RH = 75%

Figure 4.2: Bed preview after stopping fluidization of medium glass beads ($d_{50} = 267\mu m$) at 7.1 Nm^3/h (3.65 U_{mf}) for different relative himidity values (RH)

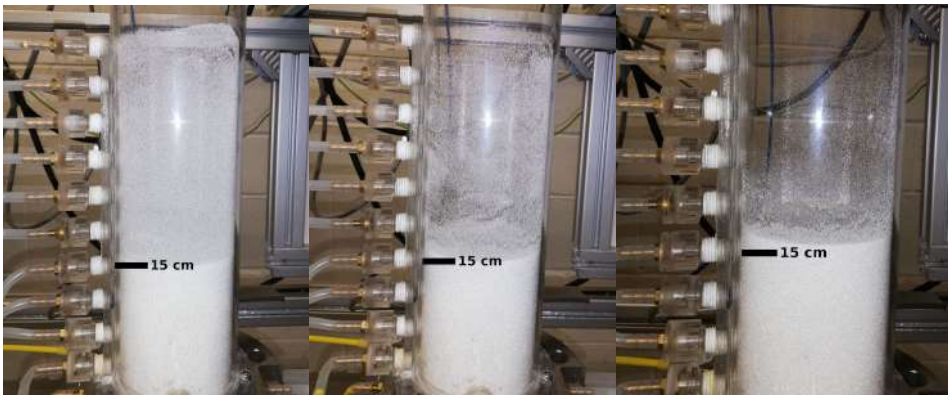

(a) RH = 40% **(b)** RH = 60% **(c)** RH = 75%

Figure 4.3: Bed preview after stopping fluidization of medium glass beads ($d_{50} = 267\mu m$) at 11.4 Nm^3/h (5.85 U_{mf}) for different relative himidity values (RH)

4.3 Minimum fluidization velocity

The experiments in fluidized beds are performed at a given multiple of minimum fluidization velocity U_{mf}. In order to determine this velocity, a first value is estimated through Wen and Yu correlation (Chapter 1, equation 1.1). After that, the air flow is set to a value above the correlation value. Then, flow rate is decreased progressively (Richardson method). For each flow rate, the fluidization is set for three minutes and the result is averaged on the last two minutes. The advantage of performing in a decreasing flow rate is that the bed is already fluidized, so the pressure overshoot does not occur when the fixed bed becomes fluidized (cf. Chapter 1, figure 1.1). All results in this section are presented are plots of normalized pressure $\frac{\Delta P}{\Delta P_{max}}$ versus gas velocity. In general cases, ΔP_{max} refers to the bed weight (see Chapter 1, subsection 1.1.2). However, this pressure corresponds to the average pressure drop located at the bottom of the bed (z = 0 cm). Due to technical details, the first pressure tap is located at 3 cm in the experimental setup. Thus, the average pressure drop at this height is referred as $\Delta P_{max} = \Delta P(z = 3cm)$ in all results.

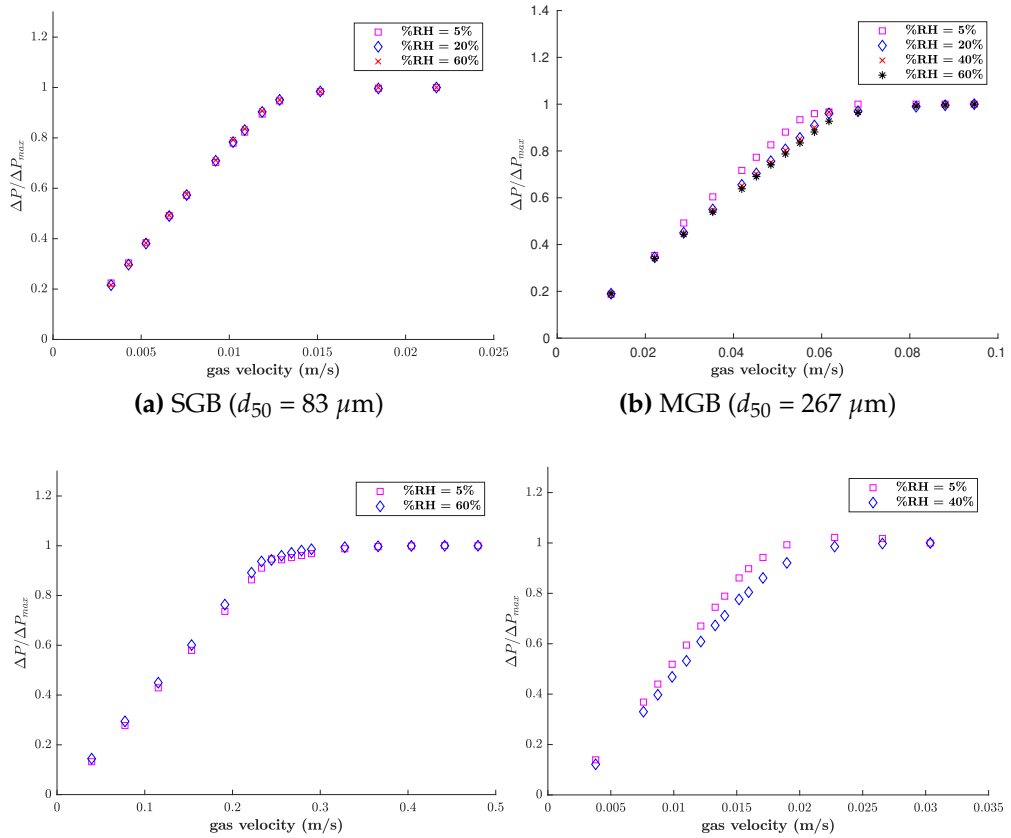

(a) SGB (d_{50} = 83 μm) **(b)** MGB (d_{50} = 267 μm)

(c) CGB (d_{50} = 554μm) **(d)** CB (d_{50} = 100 μm)

Figure 4.4: Normalized pressure drop versus gas velocity for different PSDs at different RH

Experiments are performed for each PSD at different relative humidity rates. Figure 4.4 presents normalized pressure versus gas velocity for all studied PSD. Table 4.2 recapitulate all the values found of U_{mf} for each PSD at different RHs and a comparison to the correlations in literature. Correlations always underestimate the experimental value. The correlations were only available for Geldart group B, that is why the estimation is not calculated of small glass beads. There is a slight effect for RH=5%, the minimum fluidization velocity is reached before the one at higher RHs. At higher RH, U_{mf} is not sensitive to RH. The slight difference can be attributed to the accuracy of sensors.

Table 4.2: Experimental minimum fluidization velocity for different materials versus gas relative humidity

Material	d_{50}	Minimum fluidization velocity				Wen & Yu	Thonglimp
		5%	20%	40%	60%		
GB	554 μm	0.2913	-	-	0.2947	0.2174	0.2376
	267 μm	-	0.0643	0.0648	0.0665	0.0554	0.06139
	83 μm	0.0128	0.0124	-	0.0123	-	-
CB	100 μm	0.0155	-	0.0171	-	0.01284	0.01419

4.4 Bed total net charge evolution

After U_{mf} determination, net charge of the bed is investigated. These experiments aims to determine if the total net charge reaches an equilibrium value (if there is one). Then, investigating the effect of relative humidity and gas velocity for different PSDs. In the following sections, by misuse of language, the charge evolution, increasing or decreasing, is analyzed according to its absolute value. For instance, the sentence "charge decreases at increasing RH" means implicitly "absolute value of the charge decreases at increasing RH" even it the charge is negative.

Experiments are preformed according to the protocol described in subsection 2.5. Bed is filled with a total mass of m_{total} = 2 kg of powder and fluidized at given velocity and relative humidity for a given time duration. For each time duration, experiments are performed more than once in order to verify reproducibility. Dropped particles charge is measured in the Faraday cup and the sample mass is weighed with the balance. Then the charge to mass ratio is calculated. The same thing goes for wall particles. It is important to note that emptying Faraday cup and weighing sample take about 5min. Then the Faraday cup is put again under the column to measure wall particles charge. Meanwhile, some wall particles may fall due to gravity. Unfortunately, limitation of experimental device (only one electrometer and faraday cup) does not allow to perform experiments differently. Thus, it will be assumed that the falling particles do not affect measures since the charge is reported to the mass. Moreover, some particles still stuck to the wall even after taping. This particles are not included in the analysis of the wall particles.

The accuracy of electrometer is $\leq$ 0.5% FS. In all experiments, the FS was set to 2000 nC, which means that maximum error due to electrometer measure is = 10 nC. The accuracy of the balance is $\pm$ 0.1 g. Thus, error bars due to measure accuracy for charge-to-mass ratio is calculated as follows:

$$\Delta Q_m = max\left(\frac{Q \pm 10}{m \pm 0.1}\right) \tag{4.1}$$

Where Q is the total net charge (nC) and m is the sample mass. The charge-to-mass ratio is then expressed in μC/kg.

4.5 Equilibrium charge

First experiments are performed with medium glass beads (d_{50} = 267μm) at 4.3 Nm^3/h and RH = 5%. Figure 4.5a and 4.5b shows net charge-to-mass ratio versus fluidization time for dropped and wall particles respectively. Both curves follow an exponential trend, charge grows progressively and reach an equilibrium value Q_m^{eq}. Data can be fitted according to the following model:

$$Q_m = Q_m^{eq}\left(1 - exp\left(-\frac{t}{\tau}\right)\right) \tag{4.2}$$

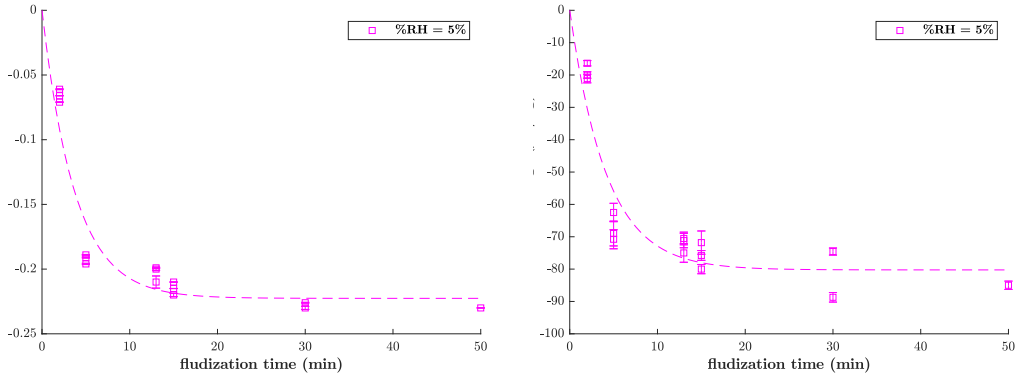

(a) Dropped particles **(b)** Wall particles

Figure 4.5: Charge-to-mass ratio evolution for MGB (d_{50} = 267μm) versus fludization time at $U_f = 2.2U_{mf}$ and RH = 5%

Where t is the fluidization time and τ is the characteristic time. Generally, exponential is considered to be near to zero for $t^{eq} = 5\ \tau$ ($exp(-5) \approx 0.0067$). Equilibrium time is then calculated to be at 5 τ.

Table 4.3 gives the parameters of fitting model with 95% confidence bounds (Curve Fitting Tool, MATLAB). Fitting model is the dashed line plotted on the figures. The R-square coefficient is good enough for both curves. It is lower for wall particles, since the gathered mass is so low (several grams) and the accuracy of the balance is $\pm$ 0.1 g. Thus, error bars are much important.

Table 4.3: Fitting model parameters for dropped and wall particles: Glass beads (d_{50} = 267μm), $U_f = 2.2U_{mf}$ and RH = 5%

	Q_m^{eq} (μC/kg)	t^{eq} (min)	R^2
dropped	-0.2226	18.72	0.8993
wall	-80.25	20.96	0.8648

Dropped particles represent 98 to 99% of the total mass. Their net charge is much lower than wall particles ($\approx$ 400 times). The same effect was observed in literature for polyethylene resin (Sowinski et al. 2010; Sowinski et al. 2012; Giffin and Mehrani 2013). One may ask why this high charge on wall particles does not diffuse to the center and the total bed charge becomes uniform? Since the column is in Plexiglas, observing visually the phenomenon give an explanation. There are two combined mechanism: the first one is the electric field. It is strong near the wall which make the particles go back to the wall even if they were torn off by the crossing bubbles. The second explanation is that the charge is not uniformly distributed on the particle surface since it is non-conductive material. This makes the particle to align with the electric field in parallel with the charged part of the surface and stick to the wall. Thus, the other side of surface does not acquire the charge (conductivity $\approx 10^{-17}$ S/m).

4.6 Effects of relative humidity

Effect of gas relative humidity (RH) was investigated by many authors (refer to subsection 1.2.3). This section presents results of charge measurements for different RH.

4.6.1 Dropped particles

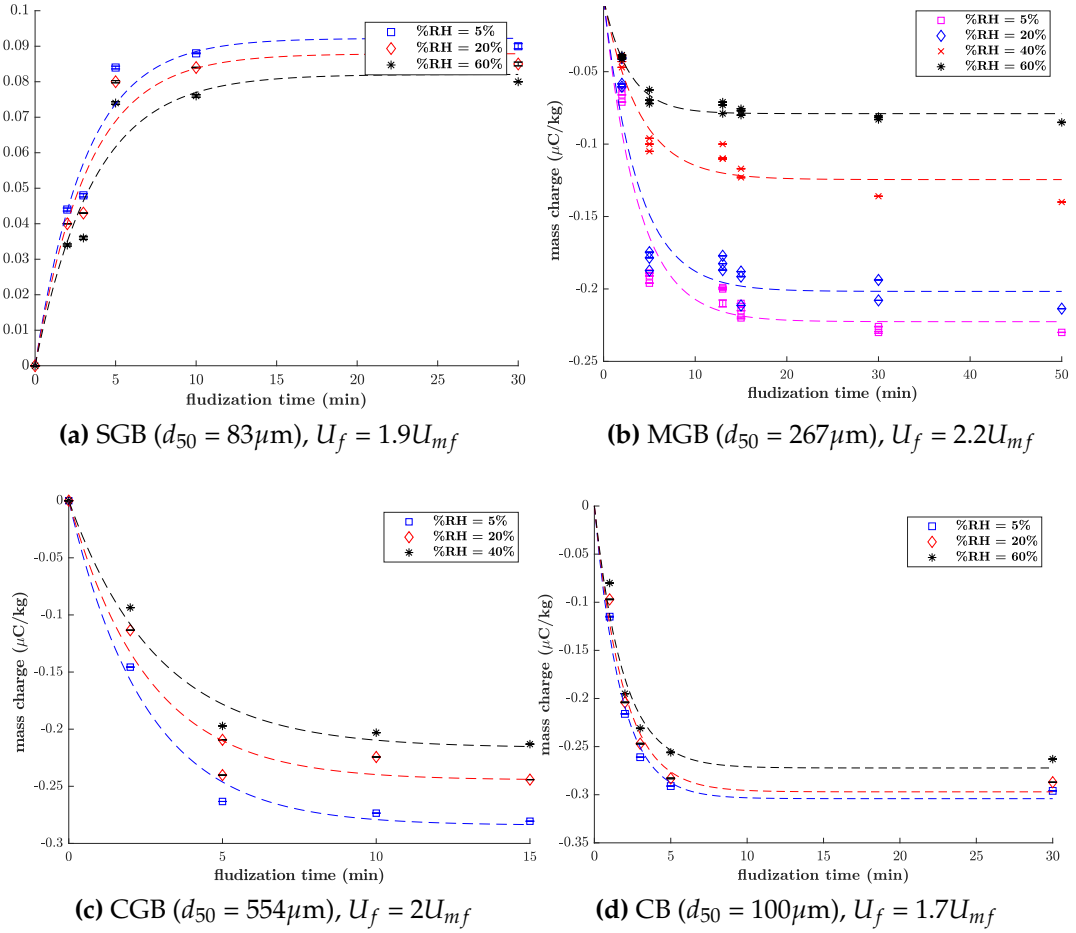

(a) SGB (d_{50} = 83μm), U_f = 1.9U_{mf}

(b) MGB (d_{50} = 267μm), U_f = 2.2U_{mf}

(c) CGB (d_{50} = 554μm), U_f = 2U_{mf}

(d) CB (d_{50} = 100μm), U_f = 1.7U_{mf}

Figure 4.6: Charge-to-mass ratio evolution of dropped particles for different PSDs versus fludization time

Figure 4.6 shows the total net charge-to-mass ratio evolution versus fluidization time of dropped particles for different PSDs. The multiplying coefficient of U_{mf} was calculated based on the values found in experiments. Table 4.4 presents the parameters of fitting model at different RH for dropped particles for all studied PSDs. All data were fitted by the Curve Fitting Tool with MATLAB software. Time needed to reach equilibrium will be referred as 'time saturation' in this study (t^{eq}).

Medium glass beads

The equilibrium charge is reduced by increasing the relative humidity which was the same effect in literature (Yao et al. 2002; Park et al. 2002b). Dry medium tends to be more charged than humid one. At a molecular scale, the presence of water molecule in the air leads to the formation of water films around the particles.

Table 4.4: Fitting model parameters for dropped particles for different PSDs at different RH

	RH	5%	20%	40%	60%
SGB ($1.9U_{mf}$)	Q_m^{eq} (μC/kg)	0.09223	0.08789	-	0.08207
	t^{eq} (min)	15.56	16.32	-	17.99
	R^2	0.9072	0.9603	-	0.9475
MGB ($2.2U_{mf}$)	Q_m^{eq} (μC/kg)	-0.2226	-0.2017	-0.1245	-0.07897
	t^{eq} (min)	18.72	18.7	19.58	13.7
	R^2	0.8993	0.8496	0.8869	0.9387
CGB ($2U_{mf}$)	Q_m^{eq} (μC/kg)	-0.2842	-0.2446	-0.2164	-
	t^{eq} (min)	12.42	12.77	14.43	-
	R^2	0.9921	0.9676	0.9818	-
CB ($1.7U_{mf}$)	Q_m^{eq} (μC/kg)	-0.3041	-0.297	-	-0.2722
	t^{eq} (min)	8.60	9.39	-	9.30
	R^2	0.9735	0.9595	-	0.9281

The saturation time shows no significant difference from 5% to 40% RH. It becomes lower for 60% RH, because the air is relatively moist which prevent charge generation and equilibrium is reached faster.

Coarse glass beads

The same effects are found for coarse glass beads (d_{50} = 554μm) in figure 4.6c. It shows a decrease of equilibrium charge by increasing RH. For this case, the time saturation is not affected by RH.

Small glass beads and ceramic beads

The same experiments were performed on smaller particles. Figures 4.6a and 4.6d shows the total net charge-to-mass ratio evolution versus fluidization time for glass and ceramic beads respectively. The RH seems not having a big effect on equilibrium charge (Q_m^{eq}) comparing to coarse one. For ceramic beads, Q_m^{eq} has the same order of magnitude as the one for medium and coarse glass beads. However, small glass beads (SGB) is much lower (about a half). Note that these particles are in the border AB of Geldart classification (see subsection 1.1.3), which means that the inter-particle forces are more significant and this may explain the behavior regarding RH.

Overall comparison

In order to quantify the way how the charge decreases at increasing relative humidity, a decreasing rate is calculated with respect to the equilibrium charge at RH = 5% following the formula:

$$\Delta_{x\%}Q_{eq} = \frac{Q_{eq}(RH = 5\%) - Q_{eq}(RH = x\%)}{Q_{eq}(RH = 5\%)} * 100 \tag{4.3}$$

This rate is reported in table 4.5. Since the data are not available for all RHs, the comparison will be done first for values at 60%, which means the both extreme cases (dry and very humid). The rate for small glass beads (SGB) and ceramic

beads (CB) is relatively low than medium glass beads (MGB). The case of SGB can be attributed to the unknown effect of inter-particle force. For ceramic beads, the effect can be attributed, with retrospect, whether to the surface state of the chemical composition. In fact, while glass beads are basically made up of SiO_2, ceramic beads are composed of ZrO_2 ($\approx 70\%$) and SiO_2 ($\approx 30\%$). This data were provided by the supplier and verified in the laboratory by means of the chemical analysis of the surface give by the Scanning Electron Microscope. Moreover, a closer look to the form of the surface is presented in figure 4.7a (CB) and 4.7b (SGB). The surface of ceramic beads looks smoother. The analysis can go no further than this due to the lack of accurate knowledge on how exactly the electrons are transferred on the surface during collisions in dense flows depending on the chemical composition.

Table 4.5: Decreasing rate of equilibrium charge versus RH for dropped particles

	$\Delta_{20\%}Q_{eq}$	$\Delta_{40\%}Q_{eq}$	$\Delta_{60\%}Q_{eq}$
CB	2.33	-	10.49
SGB	4.71	-	11.02
MGB	9.39	44.07	64.52
CGB	13.93	23.86	-

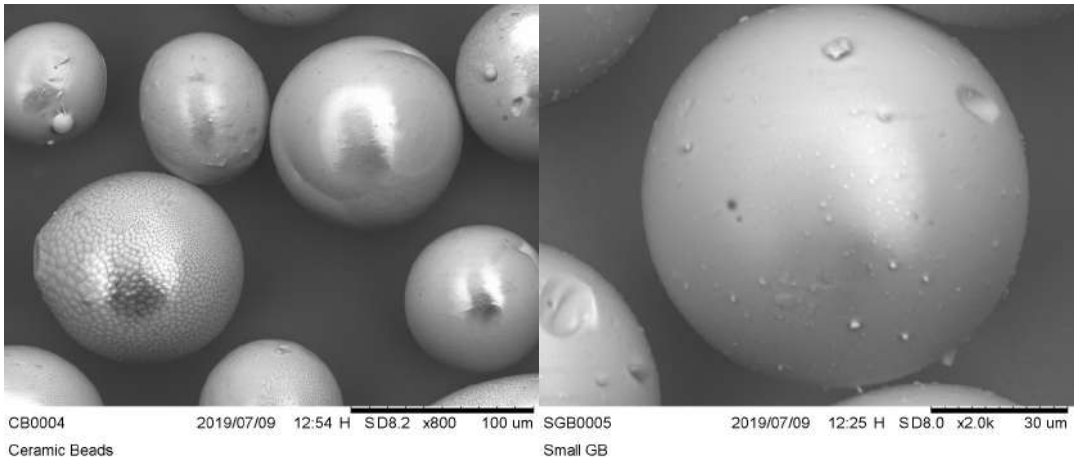

(a) Ceramic beads **(b)** Small glass beads

Figure 4.7: Closer look to the surface state of ceramic beads and small glass beads (Powered by Hitachi TM3000)

4.6.2 Wall particles

Table 4.6: Fitting model parameters for dropped particles for different PSDs at different RH

	RH	5%	20%	40%	60%
SGB	Q_m^{eq} (μC/kg)	33.44	31.35	-	23.12
	t^{eq} (min)	19.98	22.26	-	18.53
	R^2	0.9643	0.9674	-	0.9513
MGB	Q_m^{eq} (μC/kg)	-80.25	-62.31	-40.83	-18.97
	t^{eq} (min)	20.96	21.95	26.06	20.75
	R^2	0.8648	0.8252	0.8356	0.8545
CGB	Q_m^{eq} (μC/kg)	-60.76	-41.18	-36.16	-
	t^{eq} (min)	11.36	14.24	12.65	-
	R^2	0.9806	0.993	0.9005	-
CB	Q_m^{eq} (μC/kg)	-75.03	-72.11	-	-59
	t^{eq} (min)	7.96	10.32	-	11.68
	R^2	0.999	0.9728	-	0.9918

Table 4.7: Wall particles mass gathered by taping on column after 30 min of fluidization at $2.2U_{mf}$ for different relative humidity values (RH)

	Fluidization time	collected mass (g)			
		RH=5%	RH=20%	RH=40%	RH=60%
CGB	15 min	2.1	3	2	-
MGB	30 min	3.5	6.1	3.5	2.1
SGB	30 min	1.6	1	-	1.7
CB	30 min	2.6	2.1	-	2.8

Figure 4.6 shows the total net charge-to-mass ratio evolution versus fluidization time of dropped particles for different PSDs. Table 4.6 presents the parameters of fitting model at different RH for wall particles for all studied PSDs. Results of gathered mass after fluidization is presented in table 4.7. Wall particles are collected by taping the column as mentioned in Chapter 2 section 2.5.

Medium glass beads

Table 4.8: Equilibrium charge (μC/kg) of dropped and wall particles of medium glass beads (d_{50} = 267μm) for different RH at Uf = $2.2U_{mf}$

	5%	20%	40%	60%
Dropped	-0.2226	-0.2017	-0.1245	-0.07897
Wall	-80.25	-62.31	-40.83	-18.97
Ratio	361	309	328	240

The same effect of RH goes for wall particles. Figure 4.8b shows evolution of the total net charge-to-mass ratio evolution versus fluidization time for medium glass beads ($d_{50} = 267\mu m$).

Experiments were performed twice except for the case 40% and results are reproducible. Except the value of RH=5%, gathered mass decreases at increasing RH. This goes with the results for charge in figure 4.8b. The result disparity in the case of 5% is

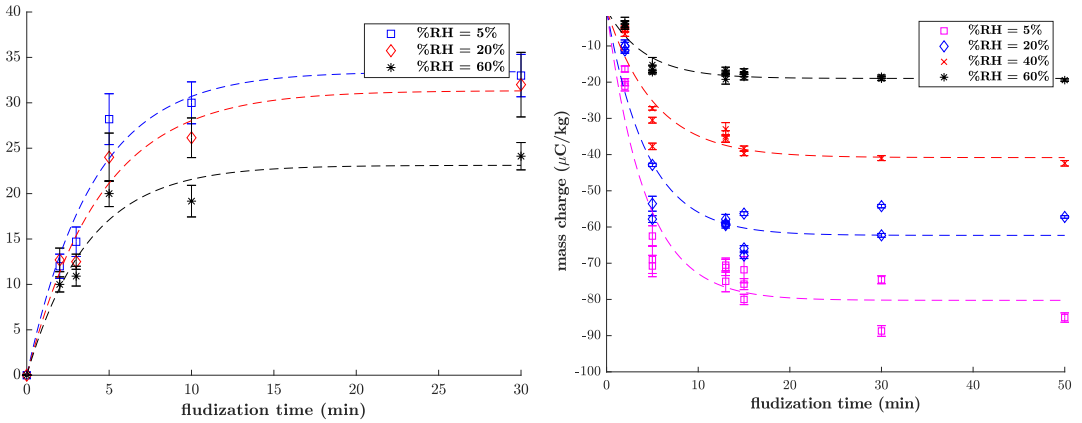

(a) SGB ($d_{50} = 83\mu$m), $U_f = 1.9U_{mf}$ **(b)** MGB ($d_{50} = 267\mu$m), $U_f = 2.2U_{mf}$

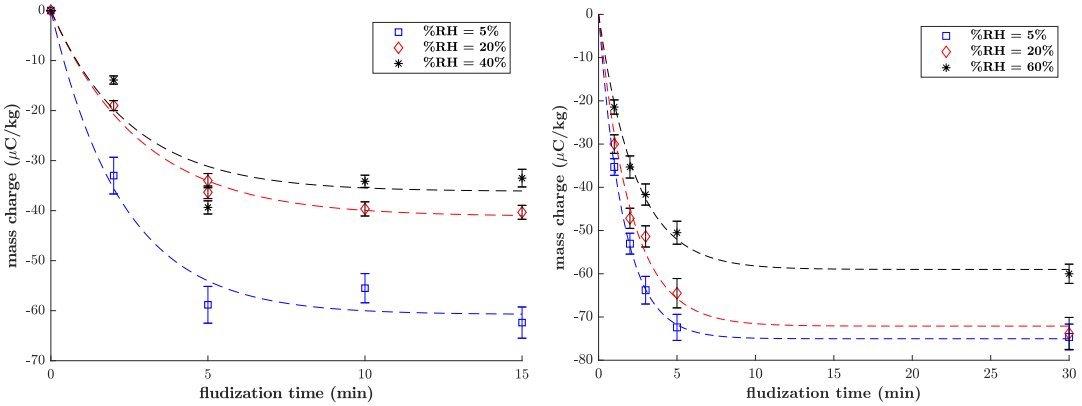

(c) CGB ($d_{50} = 554\mu$m), $U_f = 2U_{mf}$ **(d)** CB ($d_{50} = 100\mu$m), $U_f = 1.7U_{mf}$

Figure 4.8: Charge-to-mass ratio evolution of wall particles for different PSDs versus fludization time

explained by the fact that the particles are highly charged, which makes it difficult to separate them from the wall. In order to see things more clearly, pictures of the column after dropping particles are taken for different RH at 2.2 U_{mf} gas velocity shown in figure 4.9. The particles are all adhering all along the bed height for RH=5%. Table 4.8 reports the wall to dropped charge ratio. It show that wall particles are highly charged compared to the dropped one. Except the value at RH = 20%, this ratio decrease at increasing RH. A logical explanation cannot be provided for this single exception since all results show the same expected behavior (see next subsections).

Coarse glass beads

Table 4.9: Equilibrium charge (μC/kg) of dropped and wall particles of coarse glass beads ($d_{50} = 554\mu$m) for different RH at $U_f = 2U_{mf}$

	5%	20%	40%
Dropped	-0.2842	-0.2446	-0.2164
Wall	-60.76	-41.18	-36.16
Ratio	214	168	167

Coarse glass beads presented the same behavior (Figure 4.8c). Experiments were performed only up to RH=40% because of the limitation on the humidity controller.

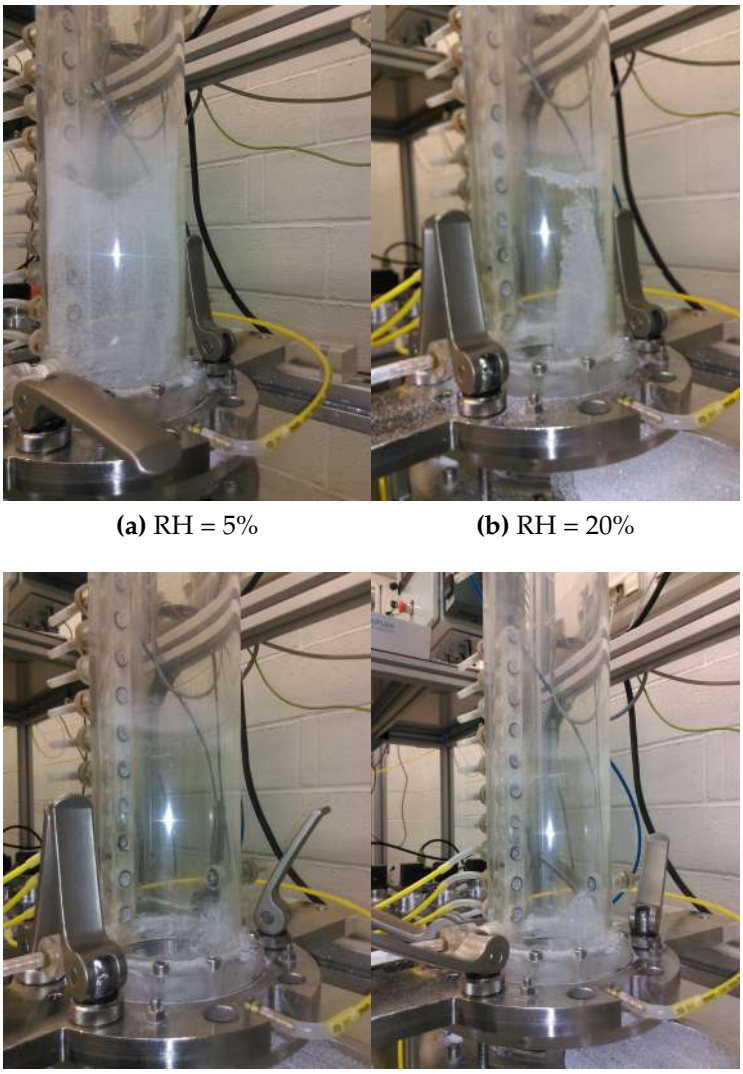

(a) RH = 5% **(b)** RH = 20%

(c) RH = 40% **(d)** RH = 60%

Figure 4.9: Bed preview of wall particles for medium glass beads ($d_{50} = 267\mu m$) at 4.3 Nm^3/h (2.2 U_{mf}) for different relative humidity values (RH)

This PSD was a bit hard to handle regarding wall particles. Actually, meanwhile the Faraday cup is being emptied ($\approx$ 5 min), wall particles start to fall down since they are heavier than medium ones. Thus, particles measured are those who were still remaining on the column wall. Experiments were performed only up to 15 min because previous results showed that saturation is reached for 30 min and 50 min. Table 4.9 reports the wall to dropped charge ratio. This ratio decreases at increasing RH. However, it is lower than the one for medium glass beads.

Small glass beads

Small glass beads presents a different behavior. Figures 4.6a and 4.8a shows the evolution of the total net charge versus fluidization time at 1.95 U_{mf} and different RHs for dropped and wall particles respectively. The first remark is the polarity of the charge, unlike other powders, small glass beads have a positive charge. The same behavior of small particles for polyethylene was reported by Sowinski et al. 2012;

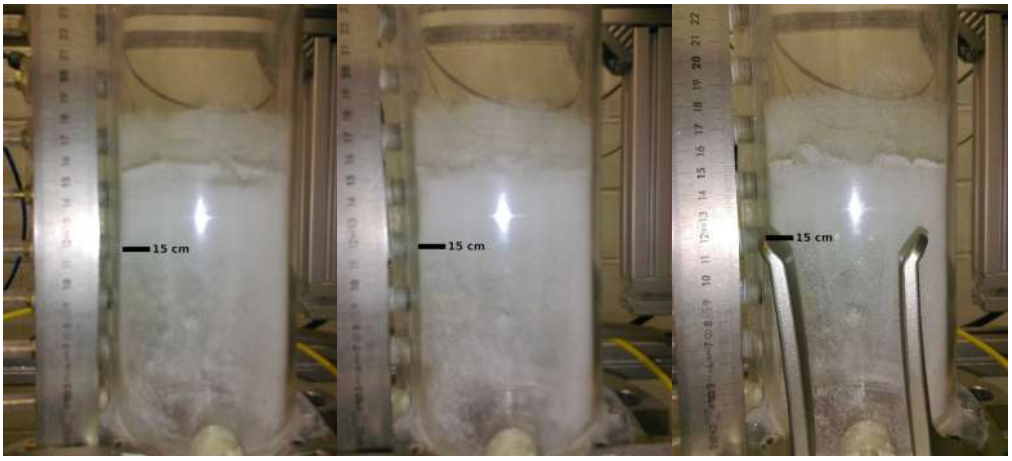

(a) RH = 5% **(b)** RH = 20% **(c)** RH = 60%

Figure 4.10: Bed preview of wall particles before taping for small glass beads ($d_{50} = 83\mu m$) at 0.73 Nm^3/h (1.9 U_{mf}) for different relative humidity values (RH)

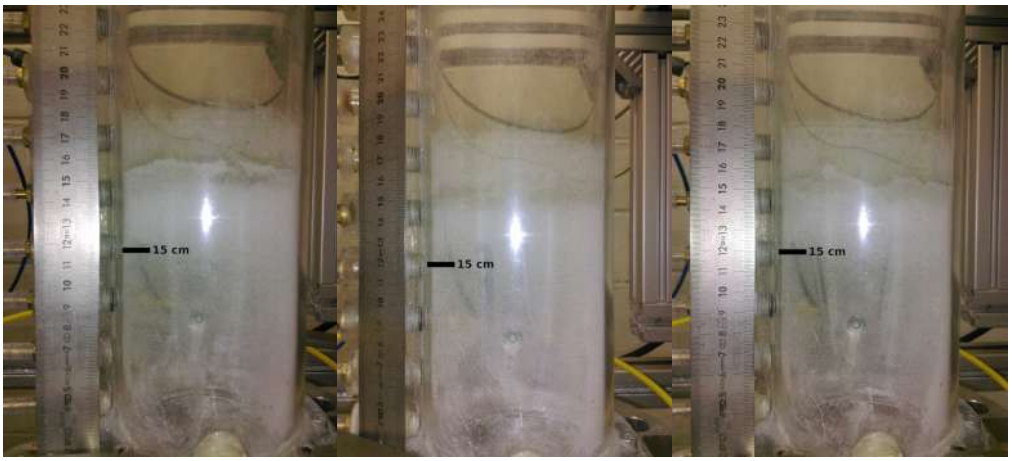

(a) RH = 5% **(b)** RH = 20% **(c)** RH = 60%

Figure 4.11: Bed preview of wall particles after taping for small glass beads ($d_{50} = 83\mu m$) at 0.73 Nm^3/h (1.9 U_{mf}) for different relative humidity values (RH)

Table 4.10: Equilibrium charge (μC/kg) of dropped and wall particles of small glass beads (d_{50} = 83μm) for different RH at Uf = 2U_{mf}

	5%	20%	60%
Dropped	0.09223	0.08789	0.08207
Wall	33.44	31.35	23.12
Ratio	363	357	282

Giffin and Mehrani 2013. The ratio wall to dropped charge shown in table 4.10 is higher than previous PSDs (medium and coarse). Going back to the gathered mass of wall particles (table 4.7), it is lower that other glass beads. This is illustrated visually in figure 4.10 (before taping) and 4.11 (after taping). No difference can be seen on pictures before and after. This is because the particles are small, less heavier and

highly charged. Inter-particle forces that make particles more cohesive can be an complementary explanation.

Regarding the effect of RH, and comparing to medium glass beads for instance, the wall particles charge does not decrease with the same rate at increasing RH (table 4.10 versus table 4.8). This was also recorded for dropped particles. The visual observation of figure 4.10 makes it more clear.

Ceramic beads

Table 4.11: Equilibrium charge (μC/kg) of dropped and wall particles of ceramic beads (d_{50} = 100μm) for different RH at Uf = 1.7U_{mf}

	5%	20%	60%
Dropped	-0.3041	-0.297	-0.2722
Wall	-75.03	-72.11	-59
Ratio	247	243	217

Ceramic beads behave like medium glass beads regarding the order of magnitude of the charge at 5%. despite their small size. However, Like the dropped one, wall particles are less sensitive the RH. As stated before, this is due to their different chemical composition.

Overall comparison

The same decreasing rate calculated through equation 4.3. Results are presented in table 4.12. This ratio goes with the previous conclusions for SGB and CB (less sensitivity to RH variation).

Table 4.12: Decreasing rate of equilibrium charge versus RH for wall particles

	$\Delta_{20\%}Q_{eq}$	$\Delta_{40\%}Q_{eq}$	$\Delta_{60\%}Q_{eq}$
CB	3.89	-	21.36
SGB	6.25	-	30.86
MGB	22.36	49.12	76.36
CGB	32.23	40.49	-

In order to have a general overview on the effect of RH, table 4.13 summarizes the ratio of wall to dropped particles equilibrium charge versus RH for different PSDs. The ratio decreases at increasing RH. However it does not decrease with the same rate. For glass beads, the ratio increases while the particle diameter decreases at a given RH.

Table 4.13: Ratio of wall to dropped particles equilibrium charge versus RH for different PSDs

	5%	20%	40%	60%
CB	247	243	-	217
SGB	363	357	-	282
MGB	361	309	328	240
CGB	214	168	167	-

4.7 Effect of gas velocity

The next step is the investigation of the effect of gas velocity. The RH is fixed at 20%. Experiments are performed at three different gas flow rates. These values were chosen to be a multiple of estimated U_{mf} from Wen and Yu correlation (2.5, 5 and 8). Which corresponds to $2.2U_{mf}$, $4.4U_{mf}$ and $7U_{mf}$ of experimental value of U_{mf} for medium glass beads. For coarse glass beads, experiments are performed at $2U_{mf}$ and $4U_{mf}$.

4.7.1 Dropped particles

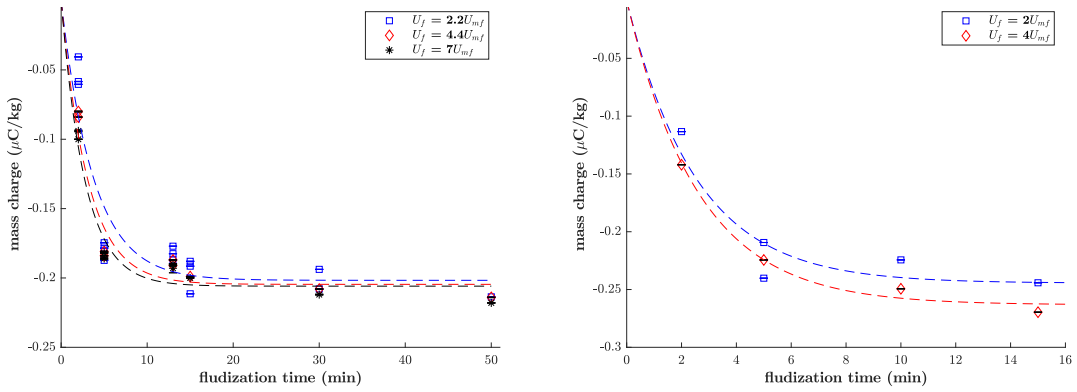

(a) MGB (d_{50} = 267μm) **(b)** CGB (d_{50} = 554μm)

Figure 4.12: Charge-to-mass ratio evolution of dropped particles versus fludization time at $RH = 20\%$

Medium glass beads

Figure 4.12a shows the evolution of charge per mass unit of dropped particles at $RH = 20\%$ for different gas velocities. The equilibrium charge of dropped particles is not affected by gas velocity. The time saturation is slightly increasing by increasing velocity. This can be explained by the increasing of collisions between particles. Which induces a faster transfer of charge inside the bed. It is concluded that, for bubbling regime, the gas velocity does not affect the total charge of dropped particles.

Coarse glass beads

Figure 4.12b presents the evolution of charge per mass unit of dropped particles at RH = 20 % for 2 and 4 U_{mf}. Unfortunately, the limitations of humidity controller does not allow to explore higher velocities. It leads to the same conclusions done for the medium glass beads.

4.7.2 Wall particles

Medium glass beads

Wall particles shows a different behavior unlike dropped ones. Figure 4.13a gives the evolution of wall particles charge per mass unit at RH = 20 % and different gas velocities. The charge increases significantly by increasing gas velocity because wall particles are the most likely to have collisions with the column. Increasing gas velocity increases collision frequency and the impact velocity. As seen in Chapter

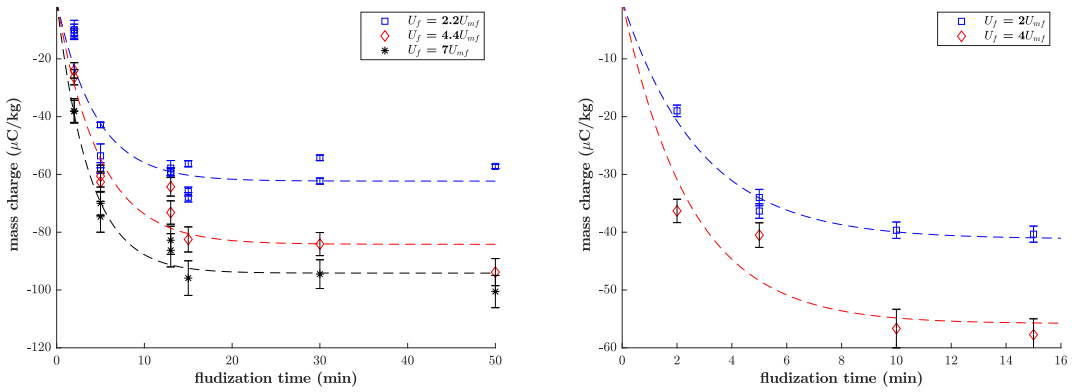

(a) MGB (d_{50} = 267μm) **(b)** CGB (d_{50} = 554μm)

Figure 4.13: Charge-to-mass ratio evolution of wall particles versus fludization time at $RH = 20\%$

3 subsection 3.3.4, the charge flux transferred from the wall during wall-particle collision depends on the particle kinetic energy in this region.

Table 4.14: Equilibrium charge (μC/kg) of dropped and wall particles of medium glass beads (d_{50} = 267μm) for different gas velocities at RH = 20%

	2.2 Umf	4.4 Umf	7 Umf
Dropped	-0.2017	-0.2046	-0.2059
Wall	-62.31	-84.18	-94.15
Ratio	309	411	457

Coarse glass beads

Wall particles charge per mass unit evolution for coarse glass beads are shown in figure 4.13b. The same effect appears for this PSD. However, the increasing percentage is not linear. This impact will be discussed later in section 4.8.

Table 4.15: Equilibrium charge (μC/kg) of dropped and wall particles of coarse glass beads (d_{50} = 554μm) for different gas velocities at RH = 20%

	2 Umf	4 Umf
Dropped	-0.2446	-0.2633
Wall	-41.18	-55.83
Ratio	168	212

4.8 Effect of PSD on charge generation

In this section, the analysis will be focused on the three PSD of glass beads: small, medium and coarse. The results are assumed to be compared to each other even if the fluidizing is slightly different. In fact the gas velocity was 1.9, 2.2 and 2 U_{mf} for small, medium and coarse particles respectively. Tables 4.16 and 4.17 give the values of equilibrium charge at different RHs of dropped and wall particles respectively. For all RHs, dropped particles charge increases when particle diameter increases. However, wall particles does not show a clear tendency.

Table 4.16: Equilibrium charge of dropped particles versus RH for different PSDs

	5%	20%	40%	60%
SGB	0.09223	0.08789	-	0.08207
MGB	-0.2226	-0.2017	-0.1245	-0.07897
CGB	-0.2842	-0.2446	-0.2164	-

Table 4.17: Equilibrium charge of wall particles versus RH for different PSDs

	5.00%	20.00%	40.00%	60.00%
SGB	33.44	31.35	-	23.12
MGB	-80.25	-62.31	-40.83	-18.97
CGB	-60.76	-41.18	-36.16	-

In order to deepen the analysis, the charge per surface unit is calculated. Note that the specific surface (the ratio of particle surface to its volume) was not calculated via the mean diameter, but given by the Malvern MS3000 device. It calculates the specific surface for each distance step of the distribution, which makes it more accurate. Table 4.18 shows the values of equilibrium charge per surface unit (instead of mass unit). This time, the surface charge increase by increasing diameter of particles. This was expected since the charge rate depends upon the contact surface, coarse particles are more likely to acquire charge since the contact surface is higher.

For the sake of including ceramic beads in the analysis, and since the ceramic beads have different density, the comparison will be based on Archimedes number. Tables shows that increasing Archimedes number increase the surface charge for both dropped and wall particles and for all RH rates except 60%. As stated before, the chemical composition is different and thus the ceramic beads have a different behavior regarding the presence of moist in the air. However, this conclusion need to be confirmed by investigating different materials with different densities.

Table 4.18: Equilibrium charge per surface unit of wall particles versus RH for different PSDs

	5.00%	20.00%	40.00%	60.00%	S_p (m^{-1})	A_r
SGB	1.120	1.050	-	0.774	73958	48.67
CB	-4.72	-4.54	-	-3.71	60849	131.59
MGB	-8.658	-6.722	-4.405	-2.047	22950	1620.24
CGB	-13.53	-9.169	-8.052	-	11120	14789.36

4.9 Conclusions

In this work, experiments were performed on different particles size distributions, different materials and different operating conditions. This aimed to understand the influence of each parameter on the charge generation/transfer and to supply the numerical modeling. Particles were fluidized for a given time then the air flow was stopped and the gas distributor is opened. Three particle size distributions (PSD) of glass beads and one of ceramic beads were studied for different relative humidity rates and different gas velocities. Results shows two categories of particles: dropped particles that falls immediately after opening the valve and wall particles that stick to the wall.

Results show no effect of relative humidity on U_{mf}. Comparison to correlation shows that correlation always underestimate the experimental values of U_{mf}.

The evolution of the net charge versus fluidization time showed an exponential trend that reached an equilibrium value for both categories (dropped and wall). Wall particles were charged 250 to 450 times than dropped ones.

Regarding the effect of RH, results showed that the net charge was decreased by increasing relative humidity for both dropped and wall particles for all PSDs. Small particles of glass beads showed a positive charge whereas all other PSDs were negatively charged. The same behavior for fine particles was highlighted in literature.

The gas velocity did not affect significantly the equilibrium charge of dropped particles. The time needed to reach equilibrium was slightly increased by increasing gas velocity. Wall particles equilibrium charge was significantly increased due to the increasing of the wall-particle collisions frequency and the relative velocity.

Increasing particle diameter for a given material make the charge per mass unit increase for dropped particles whereas the wall particles did not show a clear trend. Yet, the charge per surface unit increases (in absolute value) at increasing diameter.

5 Numerical simulations of electrostatic charges

Figures

Tables

5.1 Introduction

This chapter presents the numerical simulations of the electrostatic effects on the fluidized bed hydrodynamics. The first part discusses about the tribocharging model presented in Chapter 3. Previously in this work, it was shown that the characteristic time of the phenomenon is very high. The first section discusses about the possible alternative solutions. The second part aims to investigate the effect of the electrostatic charge in the permanent regime. In fact, the system will be considered as if the charge saturation is reached and its effect on the particles segregation and the mixing in the bed will be investigated.

5.2 Tribocharging model

In the previous Lagrangian model of Kolehmainen et al. 2016b, authors said that the equilibrium charge q_{eq} is generally larger than the saturated charge, since the already charged particles hinder the further accumulation of the charge in the system. If only the colliding particles were considered and the long-range electric field were neglected, the equilibrium charge and the saturated charge would be the same. The equilibrium charge was defined in their work by considering the interaction of an isolated particle with the wall and setting the local electric field term equal to the work function difference term:

$$q_{eq,Kolehmainen} = \frac{1}{2}\frac{\pi\varepsilon_0}{\delta_c}\Delta\varphi_{w,p}d_p^2 \tag{5.1}$$

this equilibrium charge is obtained for conducting walls ($\sigma_{wall} = 0$). In the case of non conducting walls, the charge of the wall needs to be taken into account. In this study, only the long-range electric field is considered in the fluidized bed, except the charge generation at wall which takes into account only the local electric field.

The previous estimation of the characteristic time done in Chapter 3 section 3.4 showed that the tribocharging model simulation will take days to reach saturation whereas it takes only $\approx$ 20min in experiments. The model was implemented in NEPTUNE_CFD and this observation was also verified by several numerical simulations of a 2D fluidized bed. A first solution would be amplifying the flux by a given constant to reach the equilibrium charge quicker or to modify the Young modulus. Even with a very soft Young modulus, the time saturation was still high.

Experiments showed that there are two categories of particles: dropped and wall particles. The issue is which value of q_{eq} will be set, will it be the Q_{drop} or Q_{wall}? If the q_{eq} is set to Q_{drop}, the flux will be zero once Q_{drop} is reached, thus there will not be the "wall" particles and all particles will have "dropped" particles charge. The second option is to take Q_{wall} as an equilibrium charge, but the flux needs to stop before reaching the equilibrium. In fact, if the flux continues until reaching Q_{wall}, all particles will stick to the wall because the Q_{wall} is 250 to 400 greater that Q_{drop}.

Remember that the flux equation is written as:

$$n_p \left\langle \chi_p u_p \right\rangle = n_p \underbrace{\frac{\Upsilon^{bc}}{2} \left(\frac{\rho_p}{\Upsilon^*} \right)^{\frac{2}{5}} \Theta^{\frac{9}{10}}}_{\text{charging velocity}} \left(\underbrace{\frac{\pi d_p^2}{m_p} \varepsilon_0 \left(\frac{\Delta \varphi_{w,p}}{\delta_c} + \frac{\sigma_{wall}}{2\varepsilon_0} \right)}_{\text{equilibrium charge}} - \left\langle \chi_p^c \right\rangle^- \right) \tag{5.2}$$

An alternative solution is to calculate the minimum electrostatic force required to keep particles at the wall. Since the charge flux is a function of the granular temperature, once this minimum electrostatic force is reached, it will prevent the particle from moving ($\Theta_{p,wall}$) and the charge flux will stop before reaching the equilibrium charge. Since this is just an estimation, a 1-D force balance is used. The electrostatic force is then estimated from the electrical potential in a 1-D domain whose source term depends on the dropped particles (i.e., charge q_{drop}, volume fraction α_p, and granular temperature Θ_p). The analysis provides a formula for wall-particle charge q_{wall} (coulombs) that depends on dropped-particle charge density $q_v = \alpha_p q_{drop}$ (coulombs/m^3) and known parameters in the fluidized bed. Note that the charge of a dropped particle is $q^*_{drop} = V_p q_{drop}$ where $V_p = \frac{\pi}{6} d_p^3$ is the particle volume.

5.2.1 Model for wall particles

Consider a particle of diameter d_p leaving the wall located at $x = 0$ with velocity v_0 and charge q_0. For $x \leq \lambda$ with the mean free path $\lambda = 2d_p/(3\alpha_p)$, collisions are negligible. A wall-normal force balance on the particle yields

$$\frac{dx}{dt} = v, \qquad m_p \frac{dv}{dt} = -F \tag{5.3}$$

where $m_p = \rho_p \frac{\pi}{6} d_p^3$ is the particle mass and $F = -q_0 \nabla \phi$ is the electrostatic force. Here, the question is how large F must be to trap a particle with $q_0 = q_{wall}$ within a distance λ from the wall. Over this short distance, $F > 0$ can be taken as constant. The rms velocity after collision is $v_0 = e_w \sqrt{3\Theta_p}$ where Θ_p is the granular temperature near the wall and e_w is the coefficient of restitution for particle–wall collisions.

Solving equation 5.3 with $x(0) = 0$ yields

$$v(t) = v_0 - (F/m_p)t, \qquad x(t) = v_0 t - \frac{1}{2}(F/m_p)t^2. \tag{5.4}$$

Let a (trapped) wall particle be defined by $v(t_p) = 0$ when $x(t_p) = \lambda$, i.e., a wall particle has zero wall-normal velocity at a distance λ from the wall. This leads to

$$t_p = m_p v_0 / F, \qquad \lambda = v_0 t_p - \frac{1}{2}(F/m_p)t_p^2; \tag{5.5}$$

which can be combined to find

$$F = \frac{9}{4} e_w^2 \Theta_p m_p \alpha_p / d_p, \tag{5.6}$$

which is the minimum electrostatic force required to keep a particle at the wall. In terms of the potential, its gradient at the wall must be

$$\nabla\phi|_{wall} \geq \nabla\phi|_{max} = \frac{9\alpha_p m_p e_w^2 \Theta_p}{4 d_p q_{wall}} \tag{5.7}$$

in order to have a wall layer. Physically, when the gradient of the potential reaches $\nabla\phi|_{max}$, a particle with charge q_{wall} can no longer move away from the wall. Obviously, this estimate is an upper limit since the assumed stopping distance is λ.

5.2.2 Approximation of potential and wall charge

In order to proceed further, an approximation for $\nabla\phi|_{wall}$ is needed. Assuming that the system can be approximated as 1-D for $x \in [0, D]$ with $\phi(0) = \phi(D) = 0$ and that in the interior of the fluidized bed $\alpha_p q_{drop}$ and ε_m are nearly constant, $\phi(x)$ obeys:

$$\frac{d^2\phi}{dx^2} = -\frac{\alpha_p q_{drop}}{\varepsilon_m \varepsilon_0}. \tag{5.8}$$

Solving this equation, and evaluating the gradient at the wall, yields:

$$\nabla\phi|_{wall} = \frac{D\alpha_p q_{drop}}{2\varepsilon_m \varepsilon_0}. \tag{5.9}$$

Note that in the experiments q_{drop} is initially zero, but increases with time due to the transfer of charge from the wall to the interior. However, transfer can only take place if $\nabla\phi|_{wall}$ is less than $\nabla\phi|_{max}$. When these two values are equal, charge transfer stops and q_{drop} becomes constant. With equation 5.7, this implies that at steady state q_{wall} (coulombs) and q_{drop} (coulombs/m^3) are related by:

$$q_{drop} q_{wall} \geq \frac{9\varepsilon_m \varepsilon_0 m_p e_w^2 \Theta_p}{2 D d_p} = \frac{3\pi\varepsilon_m \varepsilon_0 \rho_p d_p^2 e_w^2 \Theta_p}{4D}. \tag{5.10}$$

As this represents an order of magnitude estimate for the charges, the values for Θ_p and α_p can be taken for a fluidized bed without electrostatics (i.e., they depend on the fluidization velocity and the particle properties, etc.). Thus, the right-hand side can be multiplied by a system-independent constant that can be determined from experiments or simulations. Note that the system geometry enters in equation 5.10 only through the length scale D (distance between walls), which results from the estimate of the gradient of the potential.

For a system starting with zero charge, at steady state (equation 5.10) will be an equality, thereby relating the steady-state value of q^*_{drop} to q_{wall}. Note that equation 5.10 implies that q^*_{drop} and q_{wall} must have the same sign. Most physical systems (e.g., experiments) will correspond to this case. However, it is also possible to mix pre-charged particles with given charges $|q^*_{drop}| < |q_{wall}|$. As steady state, such a mixture would form a wall layer if equation 5.10 were satisfied. Otherwise, the particles with charge q_{wall} would be found throughout the bed. Another interesting case is when $q^*_{drop} = q_{wall}$ and equation 5.10 is satisfied. For such a case, none of the particles can move away from the walls, leaving a void in the center through which most of the gas passes. Such scenarios can easily be reproduced using numerical simulations with fixed charges.

5.2.3 Discussion

The result in equation 5.10 does not involve the equilibrium charge q_{eq} (coulombs). If $e_w = 1$, the particle would continue to collide with the wall until $q_{wall} = q_{eq}$. In real systems, $e_w < 1$, so that $|q_{wall}| < |q_{eq}|$. In any case, equation 5.10 is only valid if $|q_{eq}| \geq |q_{wall}|$, because otherwise at steady state $q_{eq} = q_{wall} = q^*_{drop}$ and no wall layer would be formed (i.e., F would never be large enough to trap particles at the wall). From the experiments, $|q_{wall}| \gg |q^*_{drop}|$, thus, the condition $|q_{eq}| \geq |q_{wall}|$ is verified. This implies that the system reaches a steady state wherein charge transfer stops because the wall-normal charge flux is null (i.e., wall particles cannot move away from the wall) and not because $q_{wall} = q_{eq}$.

In order to connect equation 5.10 to the experiments, the total charge of the dropped particles in the fluidized bed is defined as:

$$Q_{drop} = q_{drop} \frac{\pi}{4} D^2 \alpha_p H \quad \text{(coulombs)} \tag{5.11}$$

where H (m) is the bed height. Likewise, the total charge of the wall particles is

$$Q_{wall} = q_{wall} N_{wall} \quad \text{(coulombs)} \tag{5.12}$$

where N_{wall} is the number of wall particles. Experimentally, Q_{drop}, Q_{wall} and $N_{wall} =$ (total mass of wall particles)$/m_p$ can be measured. For different fluidization velocities, $\alpha_p H$ may be nearly constant, while N_{wall}, being proportional to H, would increase with increasing gas velocity. Thus, based on equation 5.10, if Θ_p also increases, $Q_{wall} \propto \Theta_p H$ is expected to increase while Q_{drop} remains nearly constant.

The current model for the wall-normal charge flux has the from

$$J_{wall} = k(q_{eq} - q), \tag{5.13}$$

and therefore does not account for the flux going to zero when $|q|$ is greater than $|q_{wall}|$, which is required for equation 5.10 to hold. A possible alternative flux model is

$$J_{wall} = k q_{eq} \left[1 - \max\left(\frac{q}{q_{eq}}, \frac{q}{q_{wall}} \right) \right], \tag{5.14}$$

which accounts for the flux inhibition due to the electrostatic force at the wall. In cases where $|q_{eq}| \geq |q_{wall}|$, the flux reduces to

$$J_{wall} = k \frac{q_{eq}}{q_{wall}} \left(q_{wall} - q \right). \tag{5.15}$$

This flux model is attractive because it shortens the time for reaching state state due to the enhancement factor $\frac{q_{eq}}{q_{wall}} \gg 1$. However, to use equation 5.15, q_{wall} must be known. This could be done using equation 5.10, but this only moves the problem to finding the steady-state value of q_{drop}.

If one is only interested in the steady-state charge distribution, knowledge of the flux is not required. At steady state, either particles are not trapped at the wall and $q_{eq} = q_{wall} = q^*_{drop}$, or a wall layer forms with q_{wall} and q_{drop} related by equation 5.10. Thus, the experimental data can be used to check if the scaling predicted by equation 5.10 is accurate, i.e., if the ratio of the left- and right-hand sides is nearly constant. For the numerical simulations, equation 5.15 can be used with the experimental values for the relaxation time (i.e., the enhancement factor) and q_{wall}.

5.3 Effect of electrostatic charge in the permanent regime

Table 5.1: Gas phase properties for numerical simulations

Description	Value
Density (kg/m^3)	1.18
Viscosity ($Pa \cdot s$)	1.8×10^{-5}
Velocity (m/s)	$2.2U_{mf} = 0.1417$
Turbulence model	$k - \varepsilon$ two-way coupling

Table 5.2: Solid phase properties for numerical simulations

Description	Value
Density (kg/m^3)	2476
Diameter (μm)	264
mass (kg)	2
$\alpha_{p,ini}$	0.39976
H_{ini} (m)	0.247
Agitation model	$q_p^2 - q_{gp}$
$\alpha_{p,max}$	0.64

Table 5.3: different cases and their charges

Case name	"neutral"	"half charged"	"75% charged"	"100% charged"	"double charged"
Q_p (μC/kg)	0	0.111	0.1665	0.222	0.444

This section aims to highlight the effect of the electrostatic charges on the fluidized bed hydrodynamics. It will be considered that all particles reached a saturation charge. The saturation charge will be equal to Q_{drop} since they represents the most particles in bed. Five case are simulated at different charges from $0 \rightarrow 2Q_{drop}$. Gas properties are presented in table 5.1. Solid phase properties are presented in table 5.2. Drag force and closure laws were defined in Chapter 3 section 3.1. The cases nomenclature and their charges are shown in table 5.3. The choice of the charge Q_{drop} was based on the measured value in experiment for medium glass beads at RH = 5 %. Then it was multiplied by different coefficients, in order to see the evolution of the bed hydrodynamics when the charge is varied. Simulations were run for 10 seconds without charges, then the electrostatic model is started. After that, the time averaging starts at t = 20s. All results were averaged over 400s, which means that the simulation lasted for 420s. The averaging duration was determined by plotting profiles over time until the time-averaged quantities were converged.

Table 5.4: Geometry parameters

Mesh	Δr (mm)	Δz (mm)	N_{cells}/diameter	Total N_{cells}
Coarse	2.55	3	48	251064
Medium	2.44	1.47	51	543375
Fine	2.08	1.23	61	907200

The mesh geometry was a 3-D cylinder with an 0.1 diamter an 0.5m height. Since the average bed height is located near to 20cm and there is no particle entrainment, the geometry height was reduced from 1m (experimental setup) to 0.5m in order to reduce the calculation cost. Convergence tests were done on three meshes with

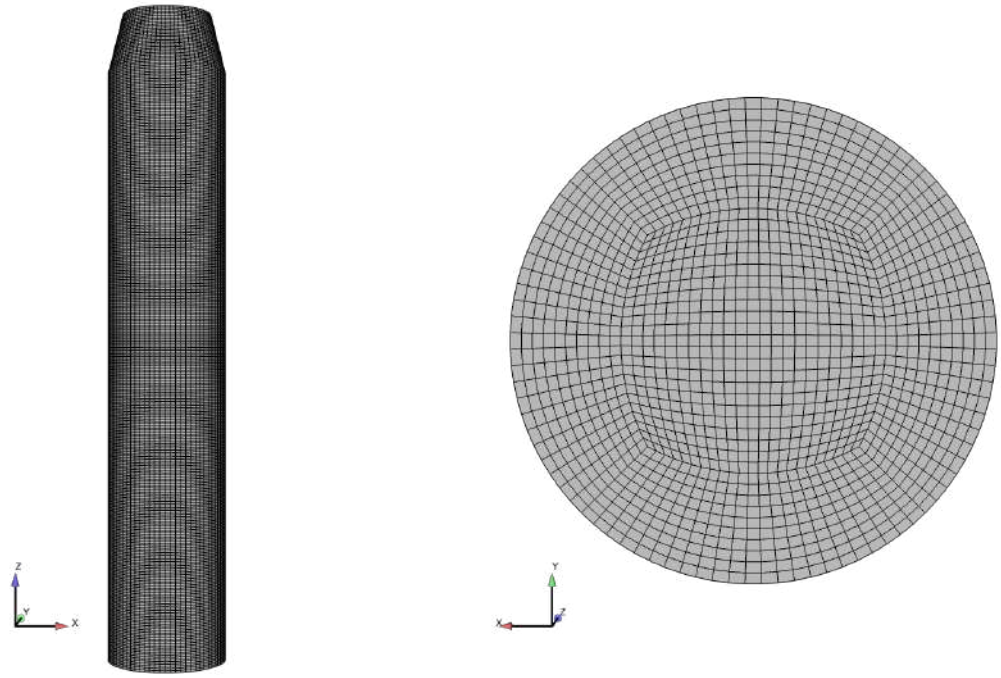

Figure 5.1: Coarse mesh preview

different cell size presented in table 5.4. All meshes were constructed by the O-grid technique. Figure 5.1 shows a preview of the coarse mesh. This convergence test was only run for "100% charged" case.

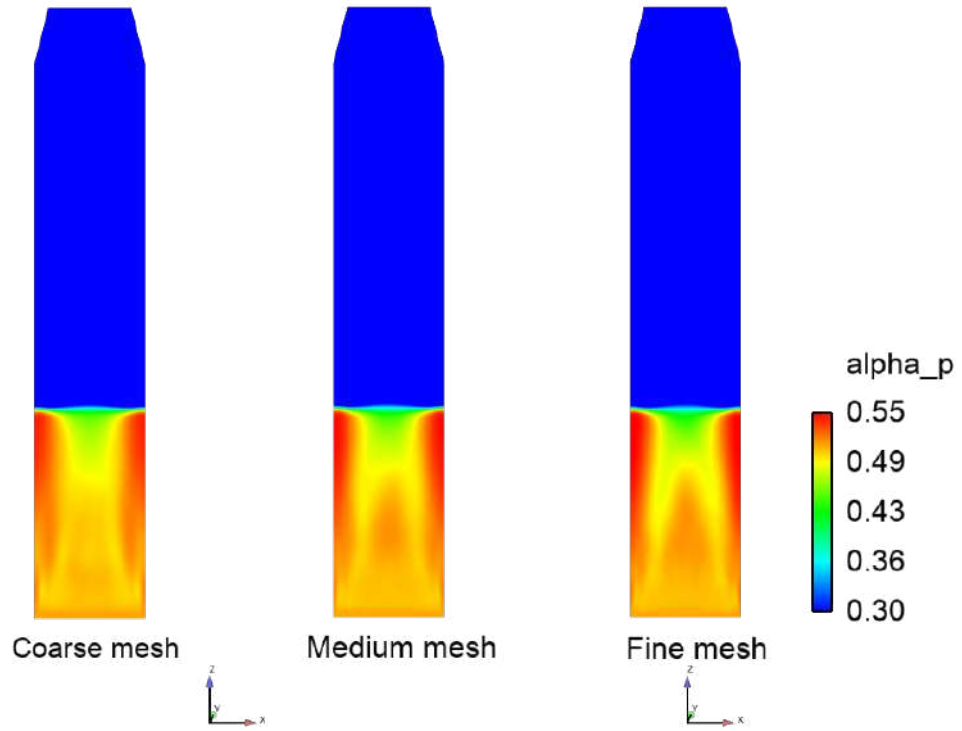

Figure 5.2: Time-averaged solid volume fraction contours for different meshes

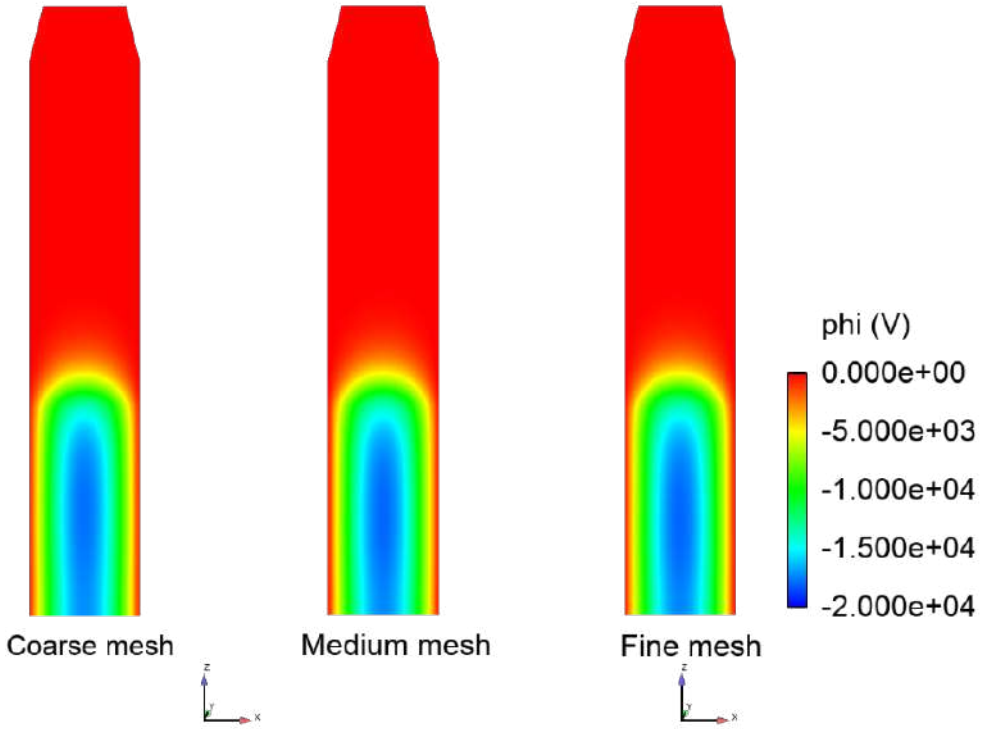

Figure 5.3: Time-averaged electric potential contours for different meshes

Figures 5.2 and 5.3 show the time-averaged solid volume fraction and time-averaged electric potential contours in a vertical plan (y=0) for different meshes. The electric potential is not sensible to mesh refining. The time-averaged solid volume fraction is slightly sensible in the bottom zone at the center. A dense zone is predicted with all meshes, but better predicted by the "medium" and "fine" mesh. This difference was not significant, thus, the mesh used is the "coarse" one with 251064 cells for all simulations.

5.3.1 Time-averaged pressure drop

Table 5.5: Average pressure gradient over the bed for different cases

Case	slope(mbar/m)	H_{bed}
Exp. RH=20%	128.25	19.5
Exp. RH=40%	128.66	19.4
Exp. RH=60%	128.93	19.4
Num. neutral	128.39	19.5
Num. $0.5Q_{drop}$	128.59	19.4
Num. $0.75Q_{drop}$	127.69	19.6
Num. Q_{drop}	127.42	19.6
Num. $2Q_{drop}$	128.89	19.4

Figure 5.4 shows the time-averaged normalized pressure evolution versus height for all simulated cases and experiments measurements. The electrostatic charges does not affect the average bed height. The differences between curves are not significant. Table 5.5 reports the pressure gradient calculated from the slope of the pressure profile

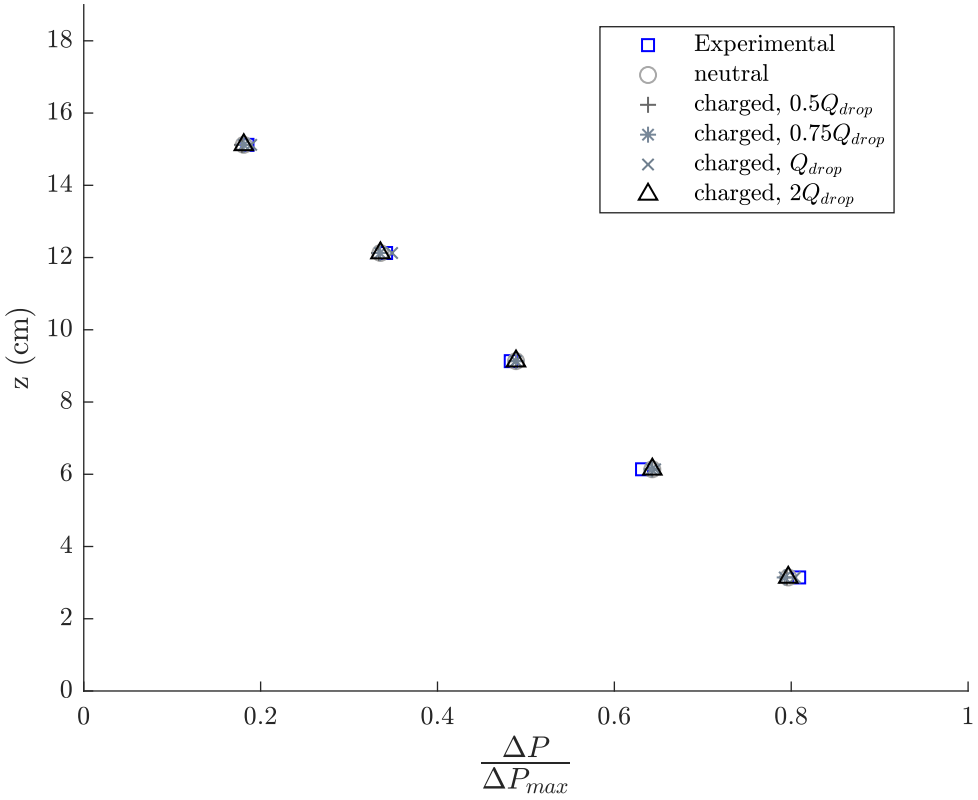

Figure 5.4: Normalized pressure drop versus height

and the average bed height. It shows no significant variation between simulated cases. This results match with experimental data that showed no effect of relative humidity, and consequently the charge, on the averaged bed height and pressure gradient. Note that this conclusion is valid only for the ranges of charge that keeps the bed fluidized. In the extreme case, where the charge are very strong, all the particles will stick to the wall, so we cannot talk about a pressure profile or a fluidized bed.

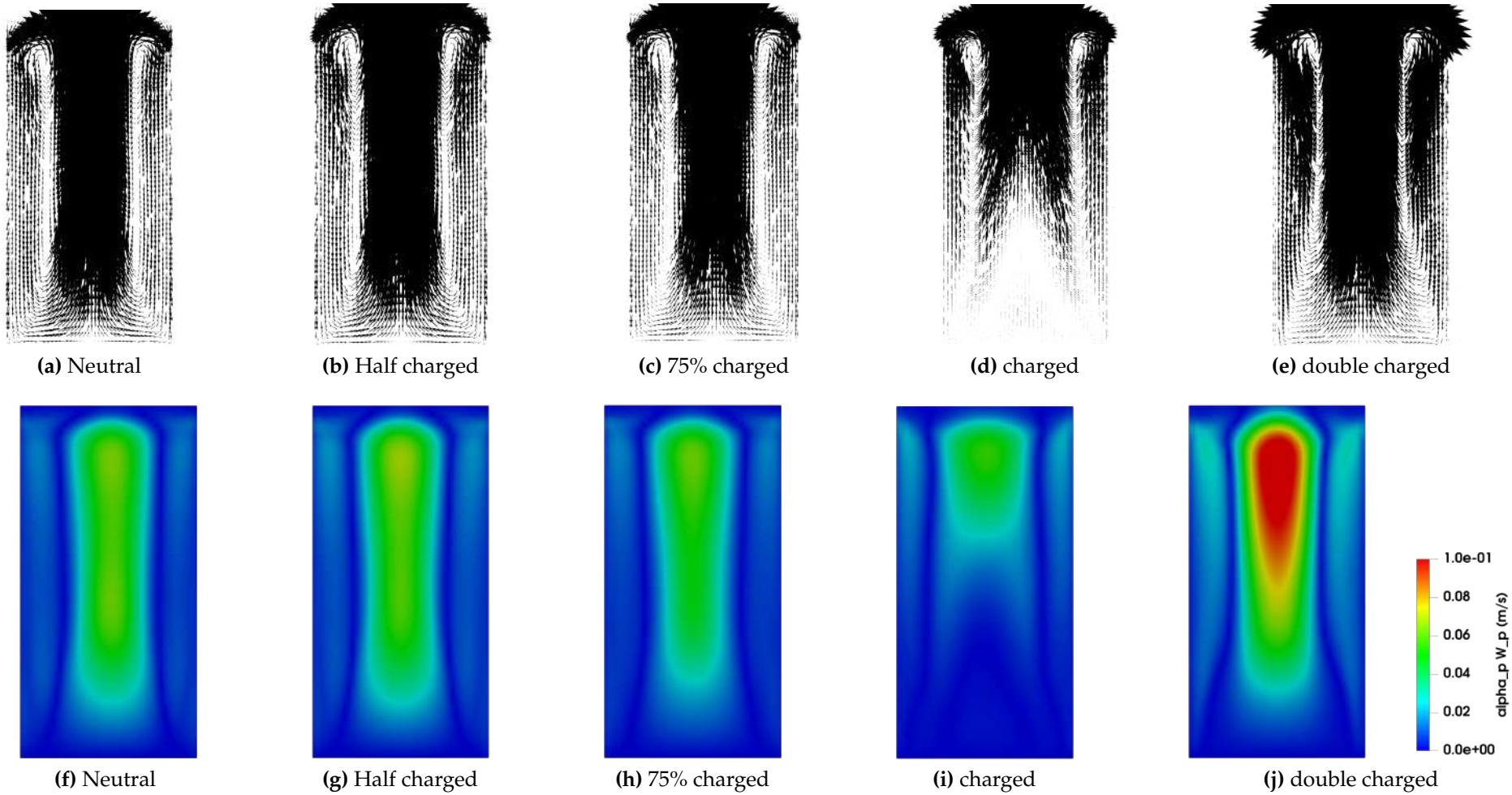

(a) Neutral **(b)** Half charged **(c)** 75% charged **(d)** charged **(e)** double charged

(f) Neutral **(g)** Half charged **(h)** 75% charged **(i)** charged **(j)** double charged

Figure 5.5: Time-averaged solid velocity field and its magnitude in a vertical plan for different charges

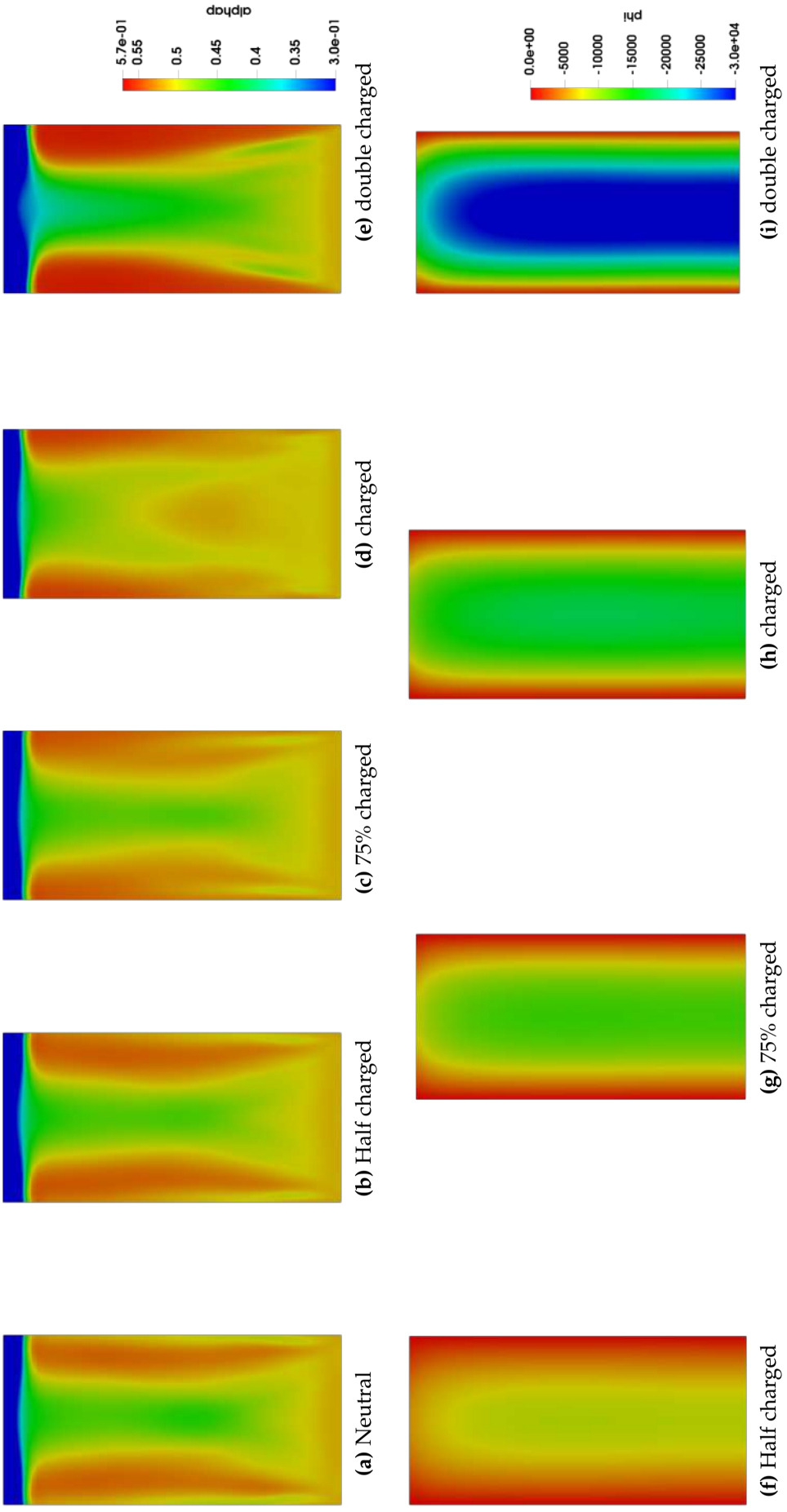

Figure 5.6: Time-averaged solid volume fraction and time-averaged electric potential contours in a vertical plan for different charges

5.3.2 Qualitative description

In this part, the analysis will be divided into two parts: the first one is the cases from $0 \rightarrow Q_{drop}$ and the second one is the "double charged" case, since they have different behaviors.

Figures 5.5a to 5.5d and 5.5f to 5.5i show the the time-averaged solid velocity field and its magnitude respectively in a vertical plan for an increase of charge from $0 \rightarrow Q_{drop}$. The vertical plan goes through the symmetry axis, which corresponds to y=0 in the simulation mesh. The magnitudes shown in figures 5.5f to 5.5i represent the norm of the time-averaged velocity third component weighed by the solid volume fraction $\overline{\alpha_p W_p}$. Figures show that, on average, the particles move upwards at the center of the reactor and downwards close to the wall. The time-averaged solid velocity field exhibits a single clockwise macroscopic mixing loop. According to the cylindrical symmetry of these time-averaged results, the 3D structure has a toroidal shape or donuts shape. In the bottom of the bed, the vertical velocity magnitude increases when going from the bottom towards the top. In the free-board region, the velocity magnitude decreases, the particles are ejected due to bubbles eruption, then the gravity overcome their kinetic energy and the go back to the bed. The mixing loop shows the formation of a cone know as "Werther cone" (Werther and Molerus 1973).

Regarding the effect of the electrostatic charge, the increase of charge from $0 \rightarrow Q_{drop}$ leads to a decrease in the velocity magnitude. Especially in the bottom of the bed. Figures 5.6f to 5.6h shows the time-averaged electric potential (φ) contours in the bed. It is related to the electrostatic force by equation 5.16:

$$\mathbf{F}_{qp,s} = -q_{p,s}\alpha_{p,s}\nabla\varphi \tag{5.16}$$

the electric potential magnitude increases when increasing the charge. A radial gradient is dominant in all bed regions for all cases. The gradient points from the center (hight potential) towards the wall (zero potential). Since all charges are negative, the electrostatic force is also directed towards the wall. The gradient is strong at the bottom and decreases in the last quarter of the bed. This explains the decrease in the velocity magnitude at the bottom of the bed near the wall, the particles are pulled towards the walls by the electrostatic force, which increases by increasing the charge. For the "100% charged" case, a clockwise loop appears at the bed bottom near the center.

Figures 5.6a to 5.6d show the time-averaged solid volume fraction contours for the charge from $0 \rightarrow Q_{drop}$. The lower values of solid volume fraction is located, on average, at the center and the dense zone is located near the walls. Right next the wall, a thick layer with lower values appears from the bottom to the third quarter of the bed for the "neutral" case. The layer height is reduced at increasing charge from $0 \rightarrow 75\%Q_{drop}$. The falling particles zone near the wall changes hardly in this charge range. However, the "100% charged" presents a dense region in the center. This region represents the recirculating zone observed on the solid velocity field (figures 5.5d and 5.5i).

The bed free-board has a form of a small "hill" for the "neutral" case. This "hill" disappears at increasing charge. A slight increase of the solid volume fraction near

the wall is observed for the "charged" case.

Now, regarding the "double charged" case, figures 5.5e and 5.5j show the time-averaged solid velocity field and its magnitude respectively in a the same vertical plan mentioned before. Both upward and downward region are thicker than "neutral" case and the velocity magnitude is highly increased in both regions. Figures 5.6i and 5.6e present the time-averaged electric potential and the time-averaged solid volume fraction respectively. The time-averaged electric potential magnitude is higher than other charged cases. The electric potential is, on average, nearly constant at the center but decreases strongly near the wall. Hence, there is a strong gradient near the wall but almost zero in the center, which pulls the particles towards the wall, letting the gas going mainly in the center. The bubbles pass mainly from the center and carry the particles. The solid volume fraction contours confirm this explanation. There is a dense region near the wall. This region is more dense than other cases. At the bottom, a tiny dense layer right next to the dense region, separated by a dilute zone. At the top, the bed is almost split into two parts, with a minimum value at the center.

5.3.3 Quantitative description

Time-averaged solid vertical velocity and net mass flux

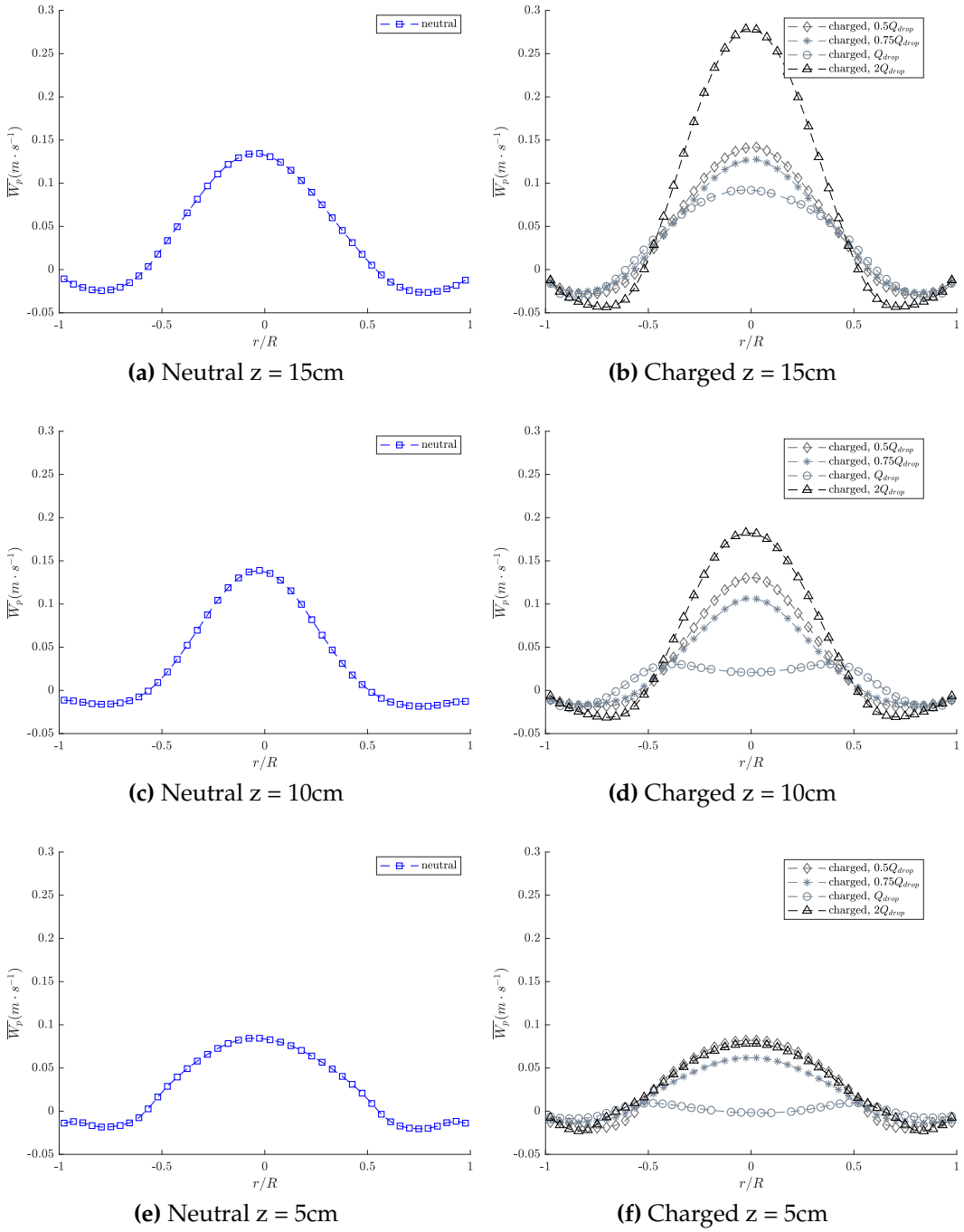

(a) Neutral z = 15cm **(b)** Charged z = 15cm

(c) Neutral z = 10cm **(d)** Charged z = 10cm

(e) Neutral z = 5cm **(f)** Charged z = 5cm

Figure 5.7: Radial evolution of time-averaged solid vertical velocity for neutral and charged cases

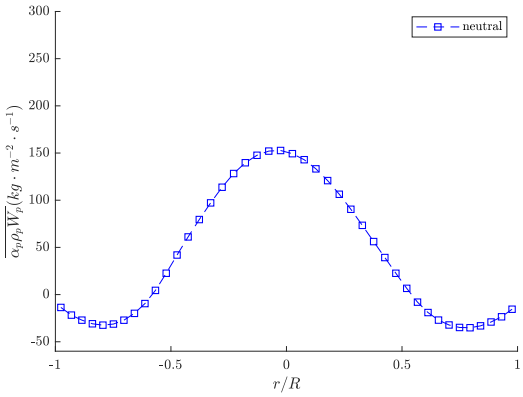

(a) Neutral z = 15cm

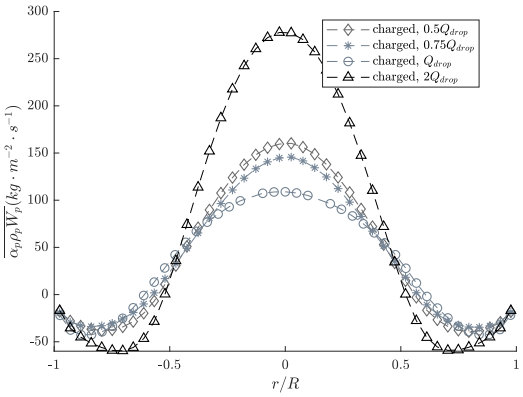

(b) Charged z = 15cm

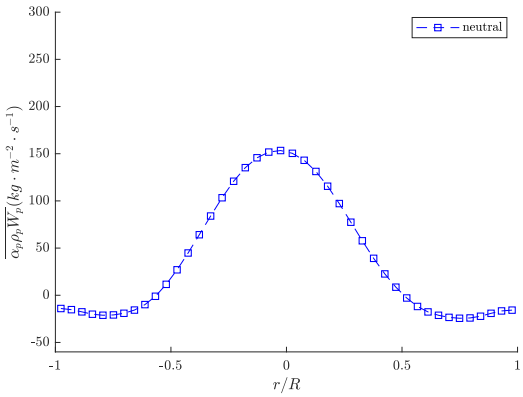

(c) Neutral z = 10cm

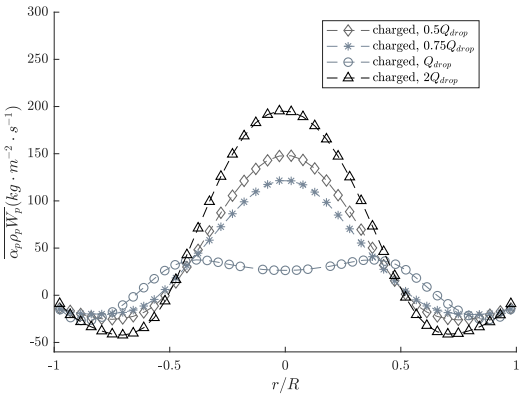

(d) Charged z = 10cm

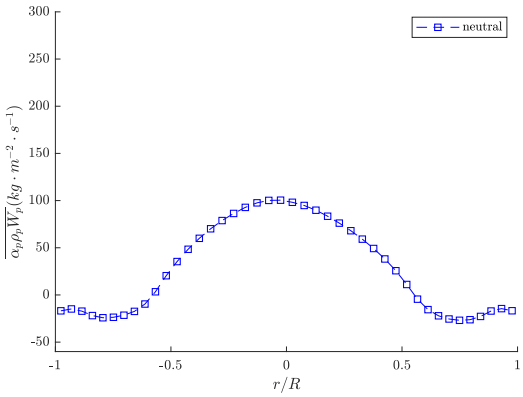

(e) Neutral z = 5cm

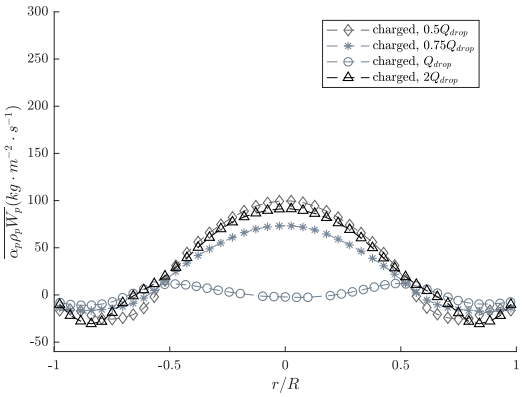

(f) Charged z = 5cm

Figure 5.8: Radial evolution of time-averaged solid net axial mass flux for neutral and charged cases

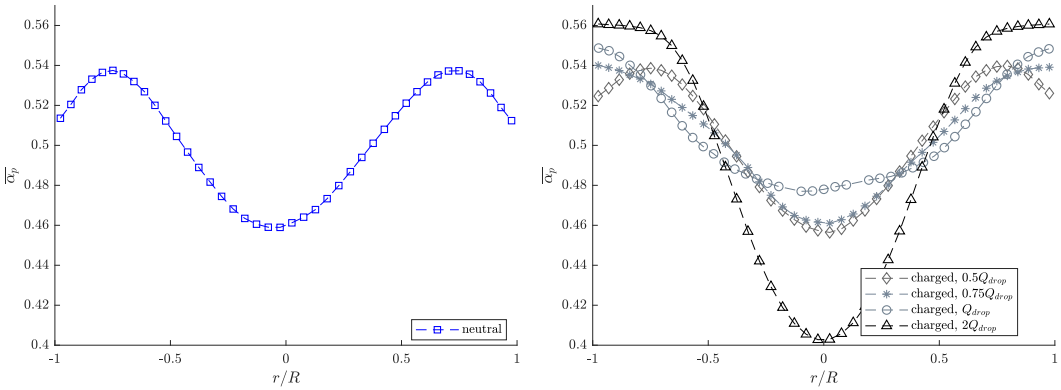

(a) Neutral z = 15cm **(b)** Charged z = 15cm

(c) Neutral z = 10cm **(d)** Charged z = 10cm

(e) Neutral z = 5cm **(f)** Charged z = 5cm

Figure 5.9: Radial evolution of time-averaged volume fraction for neutral and charged cases

Figure 5.7 shows radial profile of the time-averaged Eulerian solid velocity extracted at z = 5cm, 10cm and 15cm bed height respectively (see equation 3.143 for definition). Figure 5.8 shows the time-averaged net solid mass flux measured in the neutral and charged cases. The solid upward velocity is increased between $-0.5 < r/R < 0.5$ and a downward solid flow is observed near the wall for all cases. This phenomenon becomes more important at increasing bed height. The "half charged" and "75% charged" cases behavior is close to the "neutral" one with a slight decrease in the magnitude. The "100% charged" case has a different profile form at z = 5cm and 10cm. the vertical velocity magnitude barely changes at the center between $-0.5 < r/R < 0.5$. Besides, the downward flow region is moved toward the wall comparing to previous cases. It starts at $|r/R| > 0.7$. Increasing charge from $0 \rightarrow Q_{drop}$ leads to a decrease in the vertical velocity magnitude and consequently the vertical solid mass flux. At the bed center, this decrease rate is relatively high (75%) at the bottom of the bed at z = 5cm comparing to the top at z = 15cm where it decreases by $\approx$ 30%. The wall region is not significantly affected by the charges from $0 \rightarrow Q_{drop}$.

The "double charged" case, which represents the strongly charged case ($2Q_{drop}$), have a different behavior. At z = 5cm, "neutral" and "double charged" cases have similar profile shapes but different magnitudes. While going upward to the top, the vertical velocity of "double charged" particles becomes more important at the center and at the walls and hence the upward and downward solid mass flux are almost doubled. As stated before, this is due to the strong electric field near the wall.

Figure 5.9 gives the radial profile of time-averaged solid volume fraction neutral and charged casess. For the "neutral" case, the minimum value is located at the center. The "half charged" case has similar profile with a slight increase of the value at the wall. Increasing the charge to "75% charged" distort the profile shape at z = 10cm and 15cm. The peak near the wall is flattened and the boundary value is increased as well as the minimum value at the center.

The "charged" case profile shows a nearly constant value at the center for z = 5cm. It is much higher than previous cases. A peak appears in the center and a minimum value occurs at $|r/R| = 0.5$ for z = 10cm. This shape was observed in the solid volume fraction previously (see figure 5.6d). At z = 15cm, the peak in the center disappears and the profile takes the same shape as "75% charged" case with an increase in both the minimum value in the center and the boundary value.

The "double charged" case profile presents a distorted shape at z = 5cm. The value at the boundary is much higher. A peak appears at $|r/R| = 0.5$ which refers to the tiny layer described before in figure 5.6e. The minimum value is located at the center and is much lower than the charged case. This value at the center decreases when going toward the top. At z = 10cm, the profile take a v-shape. The volume fraction is almost constant near the wall $|r/R| > 0.8$ and decreases quickly when going towards the center. The wall region is more dense and the center is relatively dilute. At z = 15cm, the value at the center becomes lower and the dense region becomes thicker $|r/R| > 0.8$. The particles are mainly located near the wall.

Time-averaged solid horizontal velocity and radial net mass flux

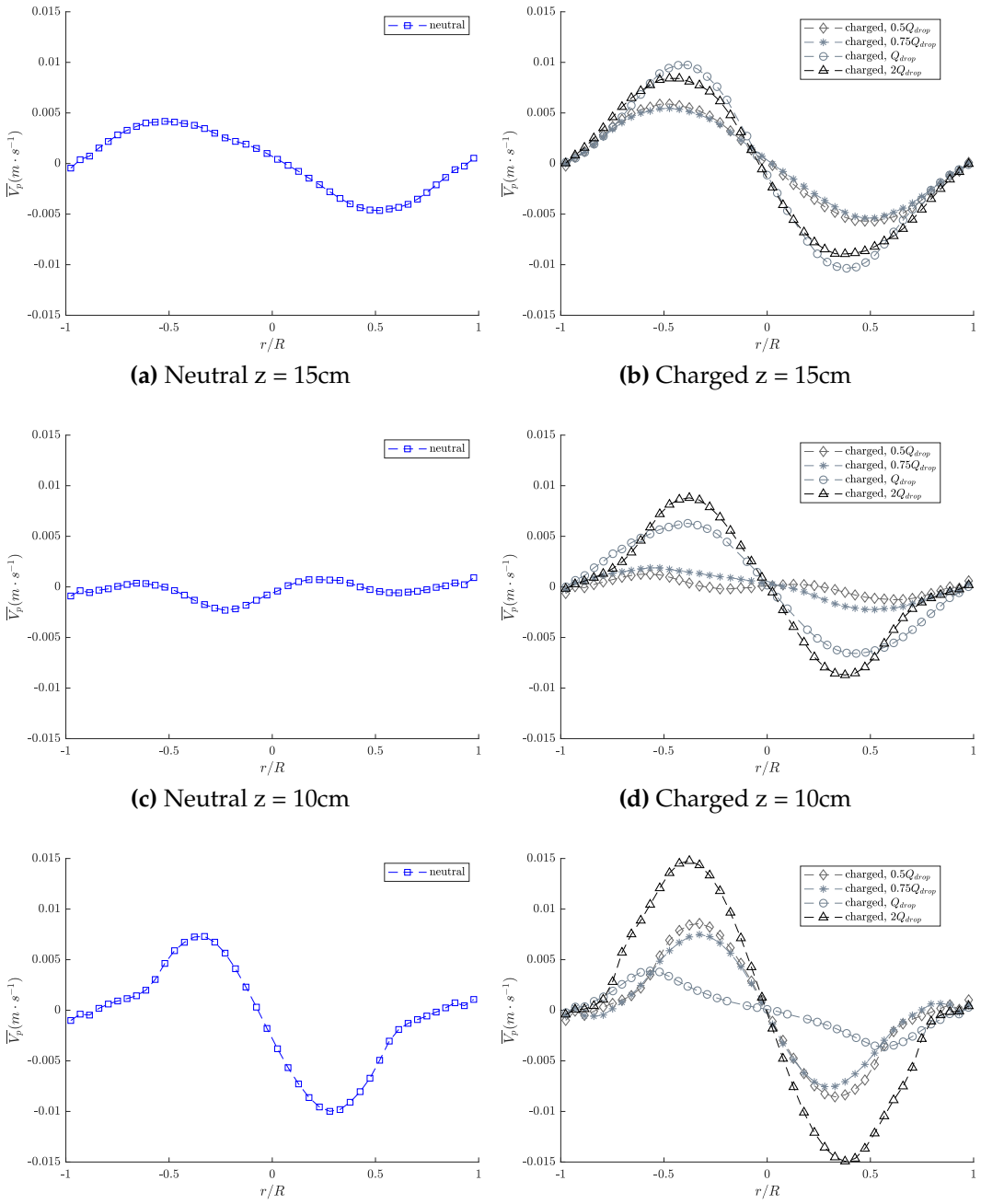

(a) Neutral z = 15cm **(b)** Charged z = 15cm

(c) Neutral z = 10cm **(d)** Charged z = 10cm

(e) Neutral z = 5cm **(f)** Charged z = 5cm

Figure 5.10: Radial evolution of time-averaged solid horizontal velocity for neutral and charged cases

Figures 5.10 and 5.11 show the time-averaged Eulerian solid horizontal velocity and the time-averaged net radial solid mass flux respectively. The peak appears at z =5cm for $|r/R| = 0.3$ for the "neutral", "half charged" and "75% charged". This peak translates the bottom part of the mixing loop where the particles recirculate from the wall to the center. The values near the wall and the center are zero because the velocity are mainly vertical (upward and downward). At z = 10cm, the horizontal velocity is almost zero for this two cases. At z = 15cm, the top part of the mixing loop shows the peak at $|r/R| = 0.5$. The "100% charged" case shows a smaller peak

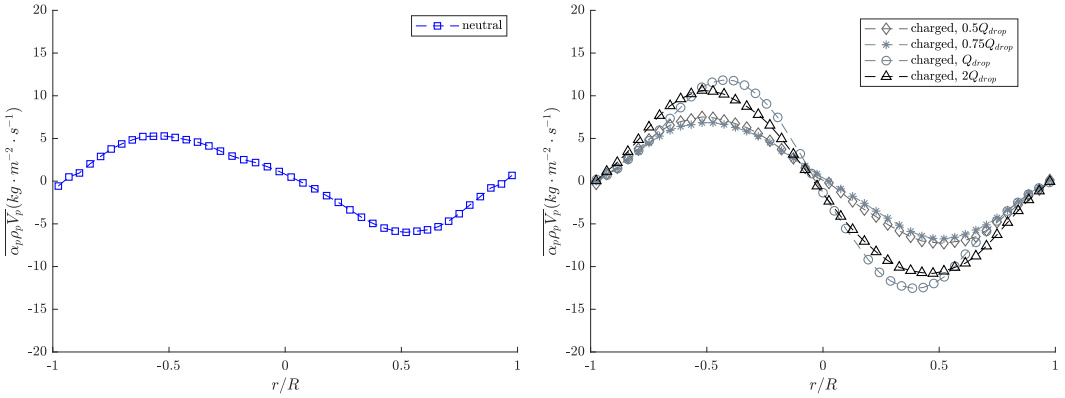

(a) Neutral z = 15cm

(b) Charged z = 15cm

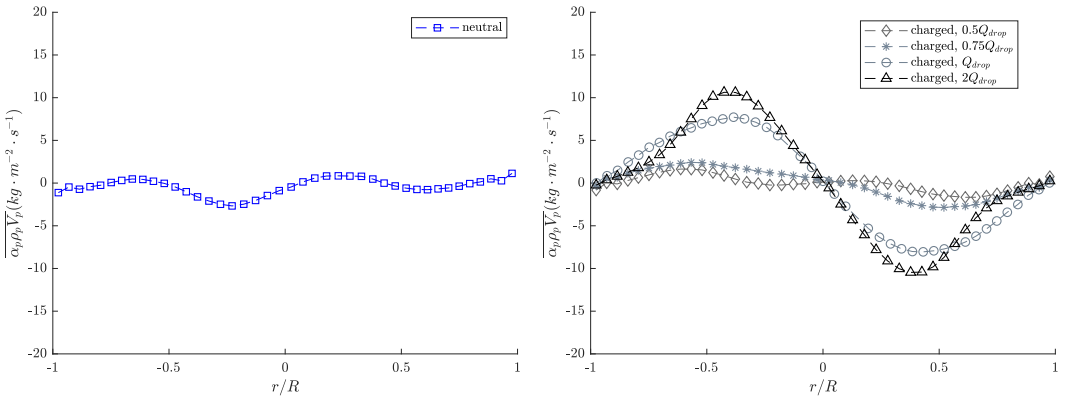

(c) Neutral z = 10cm

(d) Charged z = 10cm

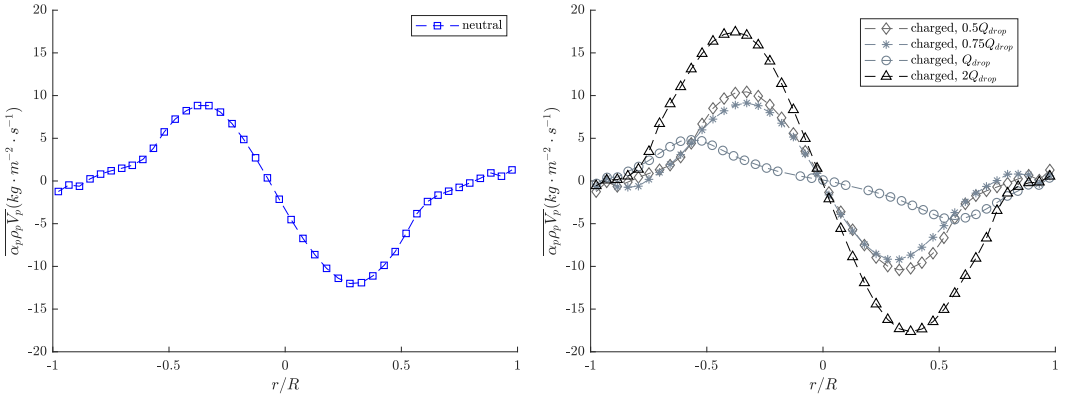

(e) Neutral z = 5cm

(f) Charged z = 5cm

Figure 5.11: Radial evolution of time-averaged radial solid net mass flux for neutral and charged cases

at z = 5cm for $|r/R| = 0.5$. This is due to dense zone appearing at the center in the bottom of the bed, which modifies the mixing loop shape and velocity magnitude. The peak at z = 10cm and 15cm is bigger because the mixing loop is moved to the top comparing to previous cases. The "double charged" shows a bigger peak than all other cases at z = 5cm and z = 10cm. This can be also seen in figure 5.5e. At z = 15cm, the solid vertical velocity is the same order of magnitude as the "100% charged" case. The same remarks go for the time-averaged net radial solid mass flux.

5.3.4 Meso-scale fluctuating motion in the bed

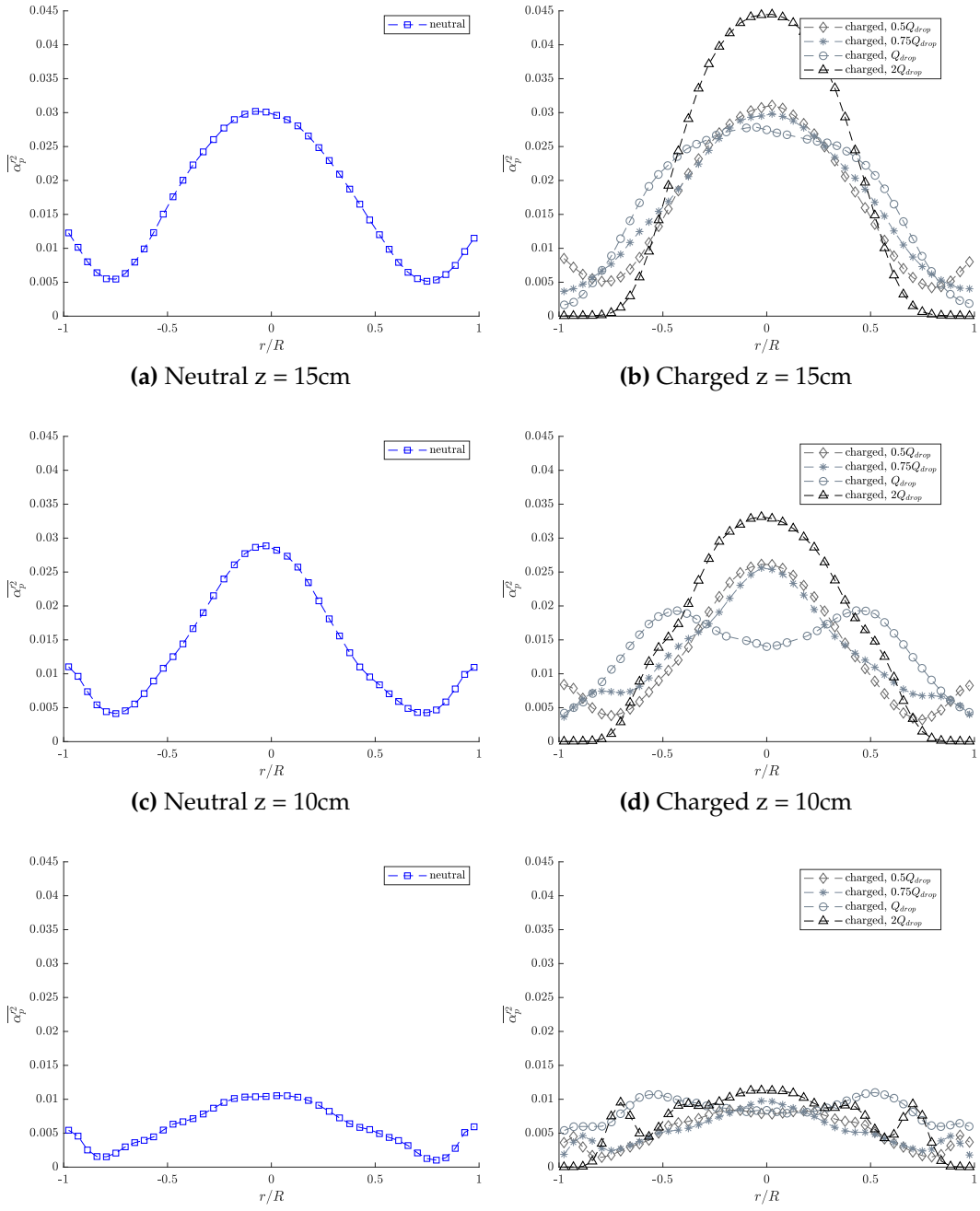

(a) Neutral z = 15cm **(b)** Charged z = 15cm

(c) Neutral z = 10cm **(d)** Charged z = 10cm

(e) Neutral z = 5cm **(f)** Charged z = 5cm

Figure 5.12: Radial evolution of time-averaged volume fraction variance for neutral and charged cases

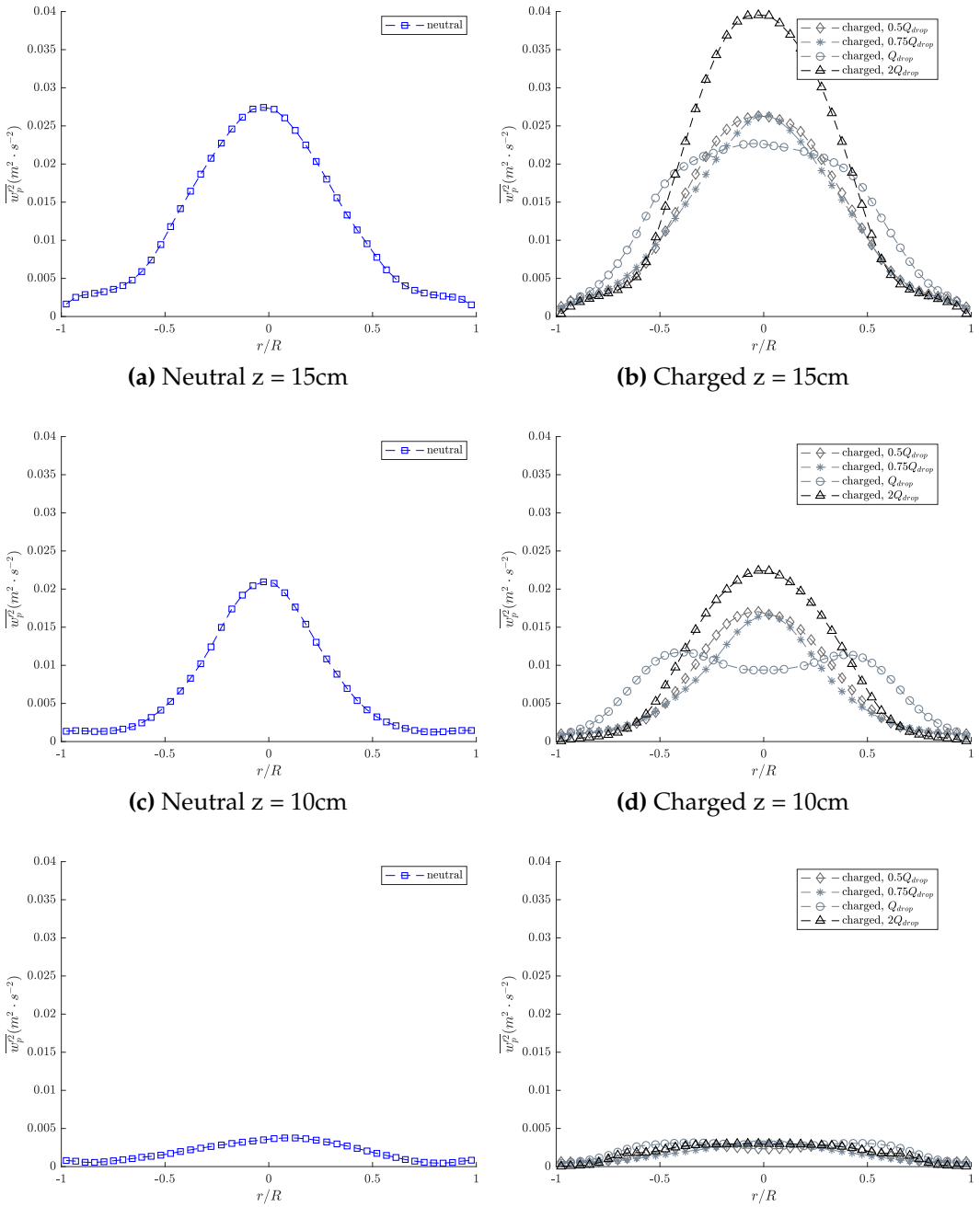

(a) Neutral z = 15cm

(b) Charged z = 15cm

(c) Neutral z = 10cm

(d) Charged z = 10cm

(e) Neutral z = 5cm

(f) Charged z = 5cm

Figure 5.13: Radial evolution of time-averaged solid vertical velocity variance for neutral and charged cases

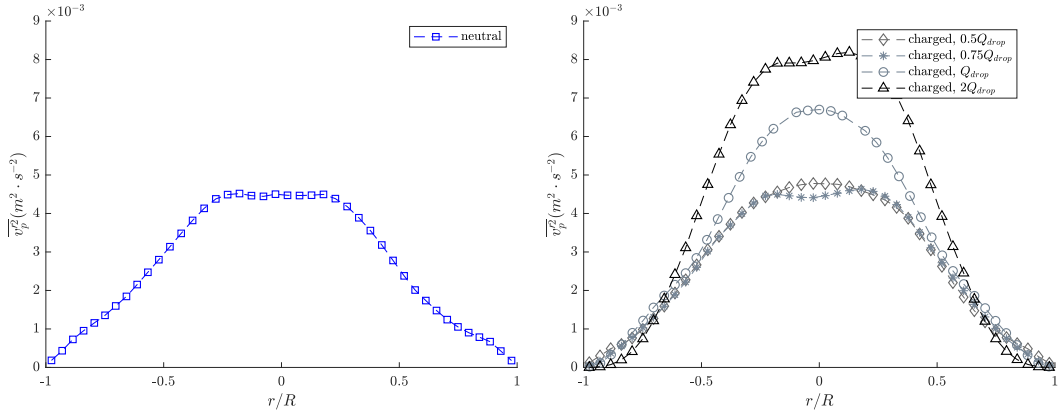

(a) Neutral z = 15cm

(b) Charged z = 15cm

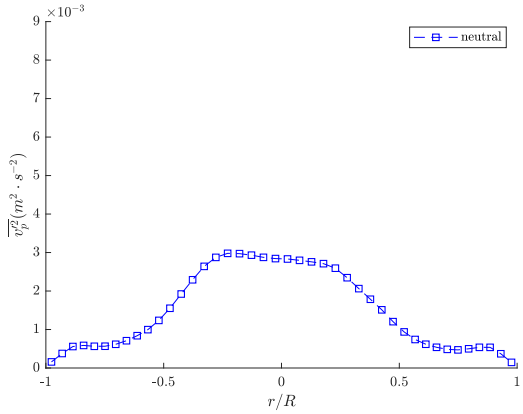

(c) Neutral z = 10cm

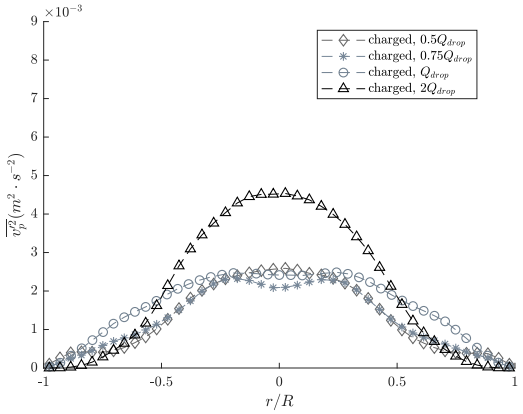

(d) Charged z = 10cm

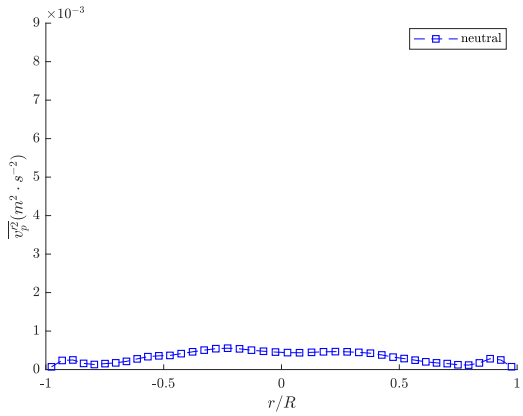

(e) Neutral z = 5cm

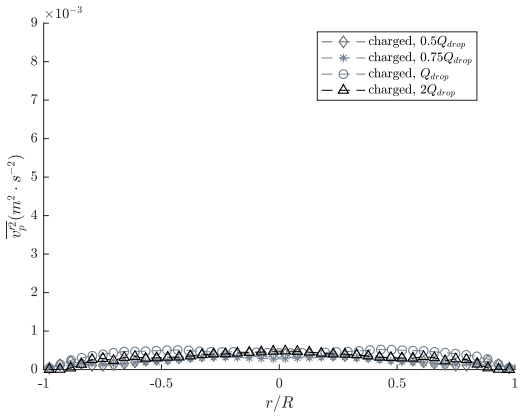

(f) Charged z = 5cm

Figure 5.14: Radial evolution of time-averaged horizontal velocity variance for neutral and charged cases

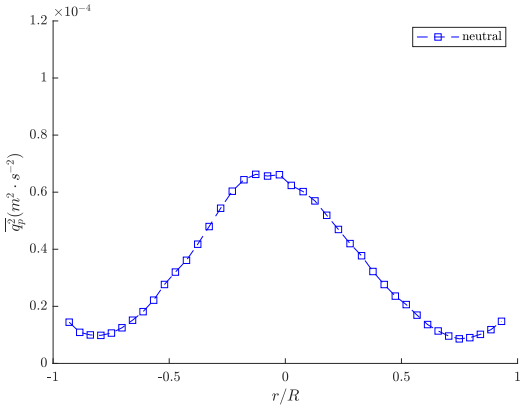

(a) Neutral z = 15cm

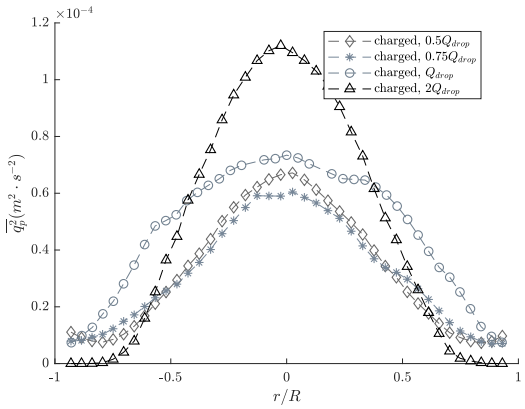

(b) Charged z = 15cm

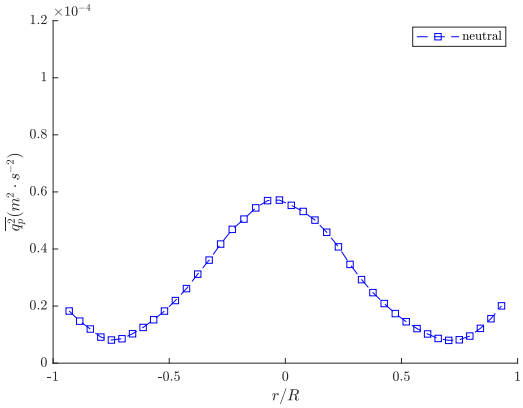

(c) Neutral z = 10cm

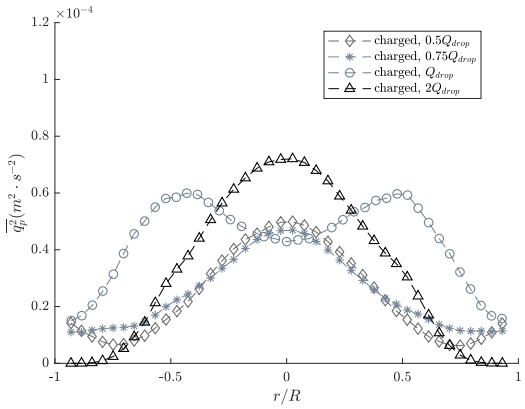

(d) Charged z = 10cm

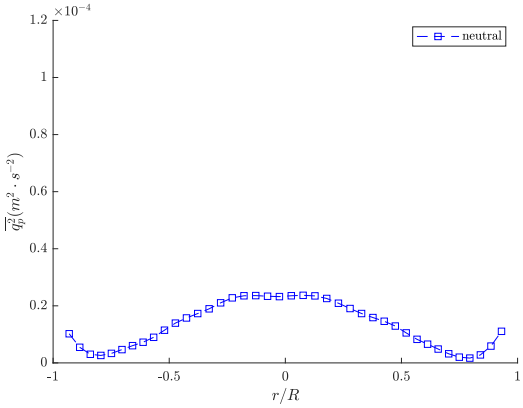

(e) Neutral z = 5cm

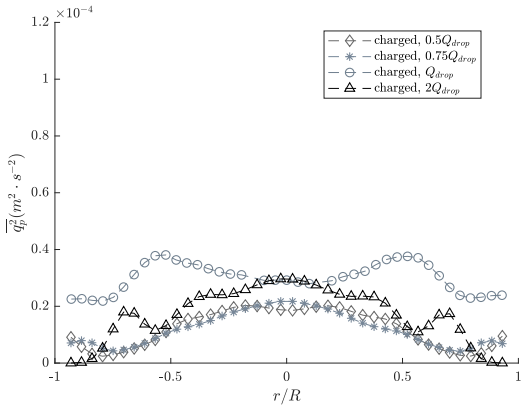

(f) Charged z = 5cm

Figure 5.15: Radial evolution of time-averaged particle random kinetic energy for neutral and charged cases

Figure 5.12 gives the time-averaged solid volume fraction variance. It characterizes the meso-scale variations of the local instantaneous particle concentration corresponding to the bubbles in the dense fluidized bed. At z = 5cm, the "neutral" case profile is almost flat at the center and it decreases near the wall. The value at the center increases when going towards the top because the bubbles become bigger due to the coalescence and generate a more important fluctuation in the solid volume fraction.

The "half charged" case profile has similar shape to the "neutral" one with a slight decrease in the boundary value. The "75% charged" case profile is a bit distorted. The distortion becomes more important at the bed top and it takes the shape of a hill, where the maximum value is located at the center and the minimum value is at the wall. The "100% charged" case shows a peak at $|r/R| = 0.5$ and a local minimum at the center. This profile links with the observations made before for this case at the bottom of the bed. This assumes that the bubbles have a preferential path. They start near the wall and rise up obliquely towards the center to end up in a similar profile at z = 15cm.

The "double charged" profile at z = 5cm shows a peak at $|r/R| = 0.8$. At the wall, the variance is equal to zero, which means that, on average, the particles located near the wall does not move. This "dead zone" near the wall becomes thicker when moving towards the top. It consist of almost 25% of the bed radius. At the center, the variance is increased. This observations confirms that the bubbles are mainly located at the center in the top half of the bed and that their size is bigger that the ones in neutral case.

The variance of the vertical and horizontal solid velocity is shown in figure 5.13 and 5.14 respectively. They are an indicator of the large scale fluctuating motion of the solid phase. Profiles are in coherence with the profiles of the solid volume fraction variance. The fluctuations are mainly in the bed center. The peak for the "100% charge" is at the moved to $|r/R| = 0.5$ as described before. For the "double charged" case, the variances are more important, which means that the axial and radial mixing is higher than other cases.

The radial profile of the time-averaged random particle kinetic energy is presented in figure 5.15. The particles agitation is increased by the presence of the charge. The "100% charged" is more agitated at z = 5cm due to the mixing loop described before. The value right next the wall is almost the same for the "double charged", "75% charged" and "100% charged" cases. The "double charged" case shows a zero value at the wall. This means that, on average, the particles does not move from the wall. This dead zone thickness becomes bigger when going upward as explained before.

5.4 Conclusions

This chapter presented the numerical work performed on two phenomenon: the charge generation mechanism and the effect of the charge once the permanent regime is established. The tribocharging model showed a very slow mechanism which does not represents the experimental measurements. A discussion was elaborated about the equilibrium charge and the charge flux. A 1-D model was presented to estimate the minimum force need to maintain a layer of particles diameter thickness near the wall. The equilibrium charge is set to the wall particles charge measured experimentally (Q_{wall}). The model showed that, once this minimum force is reached, the particles are stuck to wall ($\Theta_P = 0$) and the charge flux stops. This means that, once this saturation state is reached, the charge in the bed does not change anymore.

After that, numerical simulations were performed on the saturated bed and different charges were prescribed on the particles. Five cases were simulated with a charge varying from $0 \rightarrow 2Q_{drop}$ where Q_{drop} is the charge of dropped particles measured in the experiments at RH=5% for medium glass beads. Simulations were run for 420s and averaged over the last 400s. Results showed that the charges influences significantly the axial and radial segregation. Increasing the charge from $0 \rightarrow Q_{drop}$ showed a decrease in the vertical mass solid flux and a changing in the mixing loop and axial segregation of the solid. Moreover, the boundary value of the volume fraction increased. The $2Q_{drop}$ showed a different behavior. The charge being stronger, it induced a high electric field near the wall. The dense zone was more important and the particles, on average, did not move from the wall. On the micro-scale, the presence of the increasing of the charge value made particles more agitated.

This study showed that the presence of the electrostatic charge highly influence the topology and the mixing in the bed and need to be take into account in numerical simulations.

6 Conclusions and perspectives

Electrostatic forces have been, in most cases, a major issue in industrial applications of gas-solid fluidized beds. The phenomenon is complex and sensitive to many parameters, including gas and solid properties and operating conditions. The previous works in literature showed some gaps between the experimental and numerical approach to understand this phenomenon. This study aimed to link between the two approaches to make a representative model of electrostatic charge in gas-solid fluidized bed. The first scientific key was understanding how the electrostatic charge evolve as a function of fluidization time and to quantify the charge saturation (if there is one). Then investigating the effect of operating conditions and material on this mechanism. The next issue is how to represent the charge generation phenomenon with a theoretical model and reproduce the experimental findings with numerical simulation. This last question discussed in this study is how the presence of this charge, once the saturation is reached, influences the hydrodynamics of the bed.

The experimental part of this work was performed on a 0.1m inner diameter a 1m height Plexiglas column designed and built during this PhD. All recording systems have been calibrated and tested during the thesis. The experiments were performed in the framework of a Master degree internship. However, the system modifications, the post-processing and results interpretation were performed by the author of this thesis. The bed was fluidized for a given period of time and then the particles charge was measured by the mean of the Faraday cup technique. This cup was related to an electrometer. An amelioration of the measuring system was developed. The air network was connected to a humidity controller which was designed during this thesis. All experiments were performed at ambient pressure and temperature. Four Particle Size Distributions were investigate: three different distributions of glass beads and one of ceramic beads. The choice of these distributions aimed to see the influence of the particles size and chemical composition on the charge generation. Experiments showed two categories of particles: dropped particles which falls after opening the distributor valve and wall particles which remains adhering to the wall. Every category was measured and the charge was reported to the mass. Results showed that the total follows an exponential trend until reaching an equilibrium charge for both dropped and wall particles but wall particles were charged 250 to 400 times comparing to the dropped ones.

After that, the effect of relative humidity and gas velocity was highlighted:

- The relative humidity (RH) did not affect the averaged pressure profile of the minimum fluidization velocity.

- All PSDs were negatively charged except the small glass beads. This bipolar was reported by other works in literature.

- The relative humidity reduced the amount of charge in the bed for both categories. The ceramic beads were less sensitive to the RH comparing to glass beads.

- Increasing the gas velocity did not affect much the dropped particles charge whereas the wall particles charge increased.

- The wall to dropped charge ratio was also calculated and discussed. This ratio increased at increasing particles size.

Numerical work presented an electrostatic model based on Maxwell equation to calculate the electrostatic force induced by the presence of the charges in the bed. The model was already elaborated in literature. This model was implemented in the software simulation NEPTUNE_CFD using a Eulerian approach. The model was verified through many test cases and fully coupled with the multi-fluid model. Besides, a tribocharging model inspired from literature was presented. The model was implemented in NEPTUNE_CFD including the diffusion coefficient and wall boundary conditions. The model was based on the surface state theory where the charge transfer happens by collision. This study derived the wall boundary conditions and calculated the charge flux transferred from the wall to colliding particles. The charge flux was derived from the difference between the incident and reflected charge flux based on the probability density function of velocity.

However, the model showed a very slow timescale comparing to experiments. This model was discussed and an alternative solution was proposed. In order to reproduce the two particle categories (dropped and wall), a 1-D model is elaborated to estimate the minimum force required to maintain a layer of particles diameter thickness on the wall. Then numerical simulations were run with fixed charges, considering that the bed reached saturation, to see the influence of the charge on the meso and micro-scale. Different cases were simulated with a multiplying factor of dropped particles charge Q_{drop}. No effect on the average bed height or average pressure drop profiles were observed. This result matched with experimental findings.

Moreover, results showed that, increasing the charge from $0 \rightarrow Q_{drop}$ reduced the upward and downward flux. A changing in the bed topology occurred for Q_{drop} case where a counter clockwise mixing loop appeared in the bed bottom. The case where the charge were doubled $2Q_{drop}$ showed a different behavior. A strong electric field gradient near the wall occurred. A dead zone appeared near the wall where the particles volume fraction variance was zero on average. On the micro-scale, the charge presence make the particles more agitated.

Finally, this study quantified the effect of relative humidity, gas velocity and materials properties on electrostatic charge in the gas-solid fluidized bed. It also showed that, the presence of the charge significantly affects the bed hydrodynamics. This conclusion confirms that the electrostatic model needs to be taken into account in the CFD simulations. However, it is desirable to extend this work with further researches.

On the experimental work, more materials need to be investigated to complete the conclusions. Actually, different materials were ordered but the time did not allow to go through all of them. The choice of these materials needs to be done so that only one

the chemical composition is the changing parameter. For instance, distributions with the same Archimedes number. The Bipolar charging can be also investigated for small particles of different materials. The conclusions made about the relative humidity effects need to be also generalized for different fluidization regimes. The effect on particles entrainment was also planned to evaluate the effect of the charge on dilute regime. Unfortunately, the lack of time did not allow to perform the experiments. The entrainment will complete the database for numerical simulations.

Regarding the measuring techniques, the question that arise is about the charge distribution. The local probes used in literature can be used to complete this work. Further techniques like Particle Tracking or Electro-Capacitance Volume Tomography can also be a solution. This could be useful to investigate the effect of the charge on the local behavior of the suspension (particle trajectory and velocity and local agitation) and to validate the numerical predictions. However, The PEPT technique has a cost and safety issue and the ECVT has the image reconstruction issue. The results can be useful for comparison with tribocharging model results on numerical simulations.

On the numerical simulations, the electrostatic model with fixed charges showed important results. There is still a discussion about the influence of boundary conditions on the electric field, including the value at the wall. In fact, the zero potential at the wall is not real in some cases. Moreover, the effect of the boundary conditions of other quantities (gas and solid velocity, random kinetic energy, restitution coefficient) needs to be highlighted. The model needs also to be validated for the sub-grid meshes.

The tribocharging model, need to some improvements. A hybrid model is needed for the charge transfer at the wall to take into account the experimental timescale. Moreover, the charge for the non conductive materials is not necessarily distributed in a uniform way on the particle surface. Therefore, considering the charge on particles as a point charge located at the center is not representing the physics. This phenomenon should also be modeled. Besides, a generalization can be done for the polydisperse case and include charge transfer between particles of different phases. The interaction between different solid phase can be added as a source term in the transport equation of the averaged charge. The charge variance and charge velocity correlation need also to be modeled to complete the model.

So far, this work studied only the dense regime. Questions arise about the extent of models in dilute regime, mainly in pneumatic transport. The influence of the charge on the gas turbulence needs to be investigated.

On the other hand, the collisions were assumed to be non sensitive the electrostatic charge. However, the electrostatic force will also modify the collisions. For instance, two particles with the same charge polarity will repel each other, unless their relative velocity is sufficiently high to win the electrostatic repulsion. This means that the particles random kinetic energy model needs to be modified too.

A Appendix: Experimental table values

A.1 Minimum fludization velocity

A.1.1 Small glass beads

Table A.1: Pressure drop versus gas velocity for different gas relative humidity values - SGB

			ΔP (mbar)		
Q (Nm3/h)	Q (m3/s)	U_f (m/s)	RH=5%	RH=20%	RH=60%
0.66	1.71E-04	2.18E-02	23.81	23.71	23.79
0.56	1.45E-04	1.85E-02	23.72	23.68	23.75
0.46	1.19E-04	1.52E-02	23.39	23.42	23.51
0.39	1.01E-04	1.29E-02	22.68	22.71	23.05
0.36	9.32E-05	1.19E-02	21.15	21.42	21.57
0.33	8.54E-05	1.09E-02	19.46	19.75	19.89
0.31	8.02E-05	1.02E-02	18.45	18.58	18.83
0.28	7.25E-05	9.23E-03	16.63	16.75	16.87
0.23	5.95E-05	7.58E-03	13.51	13.56	13.70
0.20	5.18E-05	6.59E-03	11.59	11.60	11.72
0.16	4.14E-05	5.27E-03	9.11	9.03	9.16
0.13	3.36E-05	4.28E-03	7.21	7.06	7.15
0.10	2.59E-05	3.30E-03	5.33	5.11	5.16

A.1.2 Medium glass beads

Table A.2: Pressure drop versus gas velocity for different gas relative humidity values - MGB

			ΔP (mbar)			
Q (Nm3/h)	Q (m3/s)	U_f (m/s)	RH=5%	RH=20%	RH=40%	RH=60%
2.87	7.43E-04	9.46E-02	20.23	20.11	20.18	20.23
2.67	6.91E-04	8.80E-02	20.23	20.01	20.11	20.17
2.47	6.40E-04	8.14E-02	20.23	19.89	20.01	20.07
2.07	5.36E-04	6.82E-02	20.23	19.50	19.53	19.53
1.87	4.84E-04	6.17E-02	19.55	19.31	19.50	18.76
1.77	4.58E-04	5.84E-02	19.41	18.27	18.16	17.83
1.67	4.32E-04	5.51E-02	18.88	17.21	17.19	16.88
1.57	4.07E-04	5.18E-02	17.81	16.22	16.20	15.93
1.47	3.81E-04	4.85E-02	16.71	15.20	15.15	14.99
1.37	3.55E-04	4.52E-02	15.64	14.15	14.17	13.97
1.27	3.29E-04	4.19E-02	14.50	13.17	13.15	12.91
1.07	2.77E-04	3.53E-02	12.21	11.06	11.07	10.90
0.87	2.25E-04	2.87E-02	9.95	9.06	9.02	8.99
0.67	1.74E-04	2.21E-02	7.14	6.95	6.95	6.89
0.37	9.60E-05	1.22E-02	3.78	3.81	3.82	3.83

A.1.3 Coarse glass beads

Table A.3: Pressure drop versus gas velocity for different gas relative humidity values - CGB

			ΔP (mbar)	
Q (Nm3/h)	Q (m3/s)	U_f (m/s)	RH=5%	RH=60%
12.64	3.77E-03	4.80E-01	20.55	20.50
11.64	3.47E-03	4.42E-01	20.57	20.49
10.64	3.17E-03	4.04E-01	20.53	20.48
9.64	2.87E-03	3.66E-01	20.48	20.45
8.64	2.58E-03	3.28E-01	20.30	20.38
7.64	2.28E-03	2.90E-01	19.90	20.21
7.34	2.19E-03	2.79E-01	19.75	20.10
7.04	2.10E-03	2.67E-01	19.57	19.91
6.74	2.01E-03	2.56E-01	19.39	19.67
6.44	1.92E-03	2.44E-01	19.46	19.33
6.14	1.83E-03	2.33E-01	18.71	19.21
5.84	1.74E-03	2.22E-01	17.74	18.28
5.04	1.50E-03	1.91E-01	15.13	15.65
4.04	1.20E-03	1.53E-01	11.91	12.32
3.04	9.06E-04	1.15E-01	8.82	9.22
2.04	6.08E-04	7.74E-02	5.70	6.03
1.04	3.10E-04	3.95E-02	2.72	2.96

A.1.4 Ceramic beads

Table A.4: Pressure drop versus gas velocity for different gas relative humidity values - CB

			ΔP (mbar)	
Q (Nm3/h)	Q (m3/s)	U_f (m/s)	RH=5%	RH=40%
0.80	2.38E-04	3.04E-02	19.82	20.55
0.70	2.09E-04	2.66E-02	20.18	20.50
0.60	1.79E-04	2.28E-02	20.48	20.23
0.50	1.49E-04	1.90E-02	20.02	19.41
0.45	1.34E-04	1.71E-02	19.27	18.12
0.42	1.25E-04	1.59E-02	18.35	16.83
0.40	1.19E-04	1.52E-02	17.58	16.24
0.37	1.10E-04	1.40E-02	16.06	14.88
0.35	1.04E-04	1.33E-02	15.14	14.03
0.32	9.54E-05	1.21E-02	13.61	12.65
0.29	8.65E-05	1.10E-02	12.03	11.08
0.26	7.75E-05	9.87E-03	10.50	9.79
0.23	6.86E-05	8.73E-03	8.98	8.25
0.2	5.96E-05	7.59E-03	7.47	6.91
0.1	2.98E-05	3.80E-03	2.83	2.55

A.2 Electrostatic charge

A.2.1 Dropped particles

Small glass beads

Table A.5: Electric charge and powder weight versus RH for dropped particles at $U_f = 1.9U_{mf}$ - SGB

	RH = 5%		RH = 20%		RH = 60%	
T (min)	Q (nC)	M (g)	Q (nC)	M (g)	Q (nC)	M (g)
2	88	1981	79	1977	68	1981
3	94	1977	85	1979	72	1975
5	167	1979	159	1980	147	1976
10	174	1975	166	1978	151	1977
30	179	1973	169	1976	158	1975

Medium glass beads

Table A.6: Electric charge and powder weight versus RH for dropped particles at $U_f = 2.2U_{mf}$ - MGB

	RH = 5%		RH = 20%		RH = 40%		RH = 60%	
T (min)	Q (nC)	M (g)	Q (nC)	M (g)	Q (nC)	M (g)	Q (nC)	M (g)
2	-121	1973	-77	1894	-85	1978	-75	1951
2	-130	1968	-111	1899	-93	1981	-81	1963
2	-139	1965	-115	1905	-77	1972	-79	1976
5	-371	1960	-333	1907	-188	1954	-121	1934
5	-377	1970	-340	1905	-197	1962	-135	1941
5	-385	1969	-355	1895	-205	1950	-141	1952
13	-389	1959	-347	1901	-217	1965	-137	1943
13	-395	1966	-356	1904	-198	1971	-142	1933
13	-402	1958	-335	1892	-220	1978	-153	1940
15	-411	1957	-355	1888	-232	1977	-147	1944
15	-423	1967	-362	1890	-245	1981	-151	1961
15	-431	1970	-401	1897	-	-	-156	1940
30	-442	1953	-369	1904	-268	1967	-154	1931
30	-449	1962	-395	1900	-	-	-161	1947
50	-455	1977	-405	1896	-277	1973	-164	1935

Table A.7: Electric charge and powder weight versus U_f for dropped particles at RH = 20% - MGB

	$U_f = 2.2U_{mf}$		$U_f = 4.4U_{mf}$		$U_f = 7U_{mf}$	
T (min)	Q (nC)	M (g)	Q (nC)	M (g)	Q (nC)	M (g)
2	-77	1894	-166	1976	-197	1970
2	-111	1899	-159	1979	-185	1979
5	-333	1907	-356	1970	-366	1973
5	-340	1905	-365	1981	-359	1975
13	-347	1901	-369	1971	-374	1972
13	-356	1904	-375	1967	-388	1977
15	-355	1888	-394	1982	-396	1980
30	-369	1904	-409	1968	-418	1969
50	-405	1896	-423	1975	-431	1976

Coarse glass beads

Table A.8: Electric charge and powder weight versus RH for dropped particles at $U_f = 2U_{mf}$ - CGB

	RH = 5%		RH = 20%		RH = 40%	
T (min)	Q (nC)	M (g)	Q (nC)	M (g)	Q (nC)	M (g)
2	-288	1977	-223	1967	-185	1977
5	-520	1975	-472	1965	-388	1968
5	-	-	-413	1973	-	-
10	-541	1978	-444	1979	-401	1975
15	-553	1971	-481	1970	-420	1971

Table A.9: Electric charge and powder weight versus U_f for dropped particles at RH = 20% - CGB

	$U_f = 2U_{mf}$		$U_f = 4U_{mf}$	
T (min)	Q (nC)	M (g)	Q (nC)	M (g)
2	-223	1967	-280	1971
5	-472	1965	-441	1965
10	-444	1979	-491	1969
15	-481	1970	-533	1977

Ceramic beads

Table A.10: Electric charge and powder weight versus RH for dropped particles at $U_f = 1.7U_{mf}$ - CB

	RH = 5%		RH = 20%		RH = 60%	
T (min)	Q (nC)	M (g)	Q (nC)	M (g)	Q (nC)	M (g)
1	-284	2478	-241	2476	-198	2477
2	-533	2470	-504	2475	-482	2471
3	-646	2473	-611	2469	-571	2469
5	-721	2476	-699	2466	-631	2468
30	-730	2468	-707	2464	-647	2463

A.2.2 Wall particles

Small glass beads

Table A.11: Electric charge and powder weight versus RH for wall particles at $U_f = 1.9U_{mf}$ - SGB

	RH = 5%		RH = 20%		RH = 60%	
T (min)	Q (nC)	M (g)	Q (nC)	M (g)	Q (nC)	M (g)
2	12	1	14	1.1	13	1.3
3	17	1.2	20	1.6	12	1.1
5	31	1.1	24	1	30	1.5
10	42	1.4	34	1.3	23	1.2
30	53	1.6	32	1	41	1.7

Medium glass beads

Table A.12: Electric charge and powder weight versus RH for wall particles at $U_f = 2.2U_{mf}$ - MGB

	RH = 5%		RH = 20%		RH = 40%		RH = 60%	
T (min)	Q (nC)	M (g)	Q (nC)	M (g)	Q (nC)	M (g)	Q (nC)	M (g)
2	-18	1.1	-4	0.4	-3	0.6	-3	0.8
2	-19	0.9	-6	0.6	-4	0.7	-2	0.5
2	-22	1.1	-9	0.8	-4	0.6	-4	1
5	-69	1	-75	1.4	-61	2	-32	2.1
5	-75	1.2	-185	3.2	-79	2.9	-23	1.4
5	-92	1.3	-210	4.9	-83	2.2	-19	1.1
13	-105	1.4	-133	2.3	-33	1	-25	1.3
13	-121	1.7	-226	3.8	-42	1.2	-20	1.2
13	-134	1.9	-254	4.3	-64	1.8	-37	2.1
15	-79	1.1	-290	4.4	-111	2.9	-29	1.7
15	-197	2.6	-304	5.4	-139	3.5	-42	2.4
15	-232	2.9	-292	4.3	-	-	-39	2.1
30	-275	3.1	-320	5.9	-127	3.1	-37	2
30	-261	3.5	-380	6.1	-	-	-40	2.1
50	-289	3.4	-452	7.9	-123	2.9	-35	1.8

Table A.13: Electric charge and powder weight versus U_f for wall particles at RH = 20% - MGB

	$U_f = 2.2U_{mf}$		$U_f = 4.4U_{mf}$		$U_f = 7U_{mf}$	
T (min)	Q (nC)	M (g)	Q (nC)	M (g)	Q (nC)	M (g)
2	-4	0.4	-29	1.1	-38	1
2	-6	0.6	-24	1	-42	1.1
5	-75	1.4	-103	1.7	-112	1.5
5	-185	3.2	-119	1.9	-126	1.8
13	-133	2.3	-135	2.1	-138	1.6
13	-226	3.8	-139	1.9	-149	1.8
15	-290	4.4	-165	2	-163	1.7
30	-380	6.1	-185	2.2	-189	2
50	-452	7.9	-197	2.1	-191	1.9

Coarse glass beads

Table A.14: Electric charge and powder weight versus RH for wall particles at $U_f = 2U_{mf}$ - CGB

	RH = 5%		RH = 20%		RH = 40%	
T (min)	Q (nC)	M (g)	Q (nC)	M (g)	Q (nC)	M (g)
2	-33	1	-38	2	-25	1.8
5	-100	1.7	-85	2.5	-122	3.1
5	-	-	-109	3	-	-
10	-111	2	-115	2.9	-99	2.9
15	-131	2.1	-121	3	-67	2

Table A.15: Electric charge and powder weight versus U_f for dropped particles at RH = 20% - CGB

	$U_f = 2U_{mf}$		$U_f = 4U_{mf}$	
T (min)	Q (nC)	M (g)	Q (nC)	M (g)
2	-38	2	-69	1.9
5	-85	2.5	-81	2
10	-115	2.9	-102	1.8
15	-121	3	-127	2.2

Ceramic beads

Table A.16: Electric charge and powder weight versus RH for dropped particles at $U_f = 1.7U_{mf}$ - CB

	RH = 5%		RH = 20%		RH = 60%	
T (min)	Q (nC)	M (g)	Q (nC)	M (g)	Q (nC)	M (g)
1	-67	1.9	-45	1.5	-30	1.4
2	-122	2.3	-99	2.1	-53	1.5
3	-134	2.1	-113	2.2	-75	1.8
5	-181	2.5	-129	2	-101	2
30	-194	2.6	-155	2.1	-168	2.8

Bibliography

[1] Alan R Abrahamsen and D Geldart. Behaviour of gas-fluidized beds of fine powders part i. homogeneous expansion. *Powder technology*, 26(1):35–46, 1980.

[2] F. Sharmene Ali, M. Adnan Ali, G. S. P. Castle, and I. I. Inculet. Charge exchange model of a disperse system of spherical powder particles. In *The 1998 IEEE Industry Applications Conference, 1998. Thirty-Third IAS Annual Meeting*, volume 3, pages 1884–1891 vol.3, October 1998. doi: 10.1109/IAS.1998.729841.

[3] Gérard Antonini. Lits fluidisés: Caractéristiques générales et applications. *Techniques de l'ingénieur. Génie énergétique*, (BE8255), 2008.

[4] A. G. Bailey. Charging of Solids and Powders. *Journal of Electrostatics*, 30:167–180, May 1993. ISSN 0304-3886. doi: 10.1016/0304-3886(93)90072-F. URL `http://www.sciencedirect.com/science/article/pii/030438869390072F`.

[5] T. Baron, C. L. Briens, M. A. Bergougnou, and J. D. Hazlett. Electrostatic effects on entrainment from a fluidized bed. *Powder Technology*, 53(1):55–67, November 1987. ISSN 0032-5910. doi: 10.1016/0032-5910(87)80125-0. URL `http://www.sciencedirect.com/science/article/pii/0032591087801250`.

[6] HT Bi, JR Grace, and JX Zhu. Types of choking in vertical pneumatic systems. *International Journal of Multiphase Flow*, 19(6):1077–1092, 1993.

[7] Arnaud Boelle, Georges Balzer, and Olivier Simonin. Second-order prediction of the particle-phase stress tensor of inelastic spheres in simple shear dense suspensions. *ASME-PUBLICATIONS-FED*, 228:9–18, 1995.

[8] C. L. Briens, M. A. Bergougnou, I. I. Inculet, T. Baron, and J. D. Hazlett. Size distribution of particles entrained from fluidized beds: Electrostatic effects. *Powder Technology*, 70(1):57–62, April 1992. ISSN 0032-5910. doi: 10.1016/0032-5910(92)85054-Y. URL `http://www.sciencedirect.com/science/article/pii/003259109285054Y`.

[9] S. Chapman and T. G. Cowling. *The mathematical theory of non-uniform gases. 3rd edition.* 1970. ISBN 978-0521408448.

[10] Jeong-Hoo Choi, In-Yong Chang, Do-Won Shun, Chang-Keun Yi, Jae-Ek Son, and Sang-Done Kim. Correlation on the particle entrainment rate in gas fluidized beds. *Industrial & Engineering Chemistry Research*, 38(6):2491–2496, 1999. doi: 10.1021/ie980707i. URL `http://dx.doi.org/10.1021/ie980707i`.

[11] R Clift, JR Grace, and ME Weber. Bubbles, drops and particles new york. *NY: Academic Press [Google Scholar]*, 1978.

[12] Roland Clift and J. Grace. Bubble interaction in fluidized beds. 1970.

[13] Clayton T Crowe and EE Mechaelides. Basic concepts and definitions. *Multiphase Flow Handbook*, pages 24–25, 2006.

[14] Jianmin Ding and Dimitri Gidaspow. A bubbling fluidization model using kinetic theory of granular flow. *AIChE journal*, 36(4):523–538, 1990.

[15] Yann Dufresne, Vincent Moureau, Enrica Masi, Olivier Simonin, and Jeremy Horwitz. Simulation of a reactive fluidized bed reactor using cfd/dem. 2016.

[16] C Alberto S Felipe and SCS Rocha. Time series analysis of pressure fluctuation in gas-solid fluidized beds. *Brazilian Journal of Chemical Engineering*, 21(3):497–507, 2004.

[17] P Fevrier and O Simonin. Constitutive relations for fluid-particle velocity correlations in gas-solid turbulent flows. In *3rd Int. Conf. on Multiphase Flows*, pages 8–12, 1998.

[18] Justin Finn, Ming Li, and Sourabh Apte. Particle based modelling and simulation of natural sand dynamics in the wave bottom boundary layer. *Journal of Fluid Mechanics*, 796:340–385, 06 2016. doi: 10.1017/jfm.2016.246.

[19] Farzam Fotovat, Renaud Ansart, Mehrdji Hemati, Olivier Simonin, and Jamal Chaouki. Sand-assisted fluidization of large cylindrical and spherical biomass particles: Experiments and simulation. *Chemical Engineering Science*, 126:543–559, 2015.

[20] Farzam Fotovat, Turki A Alsmari, John R Grace, and Xiaotao T Bi. The relationship between fluidized bed electrostatics and entrainment. *Powder Technology*, 2016.

[21] Farzam Fotovat, John R Grace, and Xiaotao T Bi. Particle entrainment from gas-solid fluidized beds: Conductive vs. dielectric fines. *AIChE Journal*, 63(4): 1194–1202, 2017.

[22] Rodney O Fox. Quadrature-based moment methods for multiphase chemically reacting flows. In *Advances in Chemical Engineering*, volume 52, pages 1–50. Elsevier, 2018.

[23] Derek Geldart. Types of gas fluidization. *Powder technology*, 7(5):285–292, 1973.

[24] Dimitri Gidaspow. *Multiphase flow and fluidization: continuum and kinetic theory descriptions*. Academic press, 1994.

[25] Amanda Giffin and Poupak Mehrani. Effect of gas relative humidity on reactor wall fouling generated due to bed electrification in gas-solid fluidized beds. *Powder Technology*, 235:368–375, February 2013. ISSN 0032-5910. doi: 10.1016/j.

powtec.2012.10.037. URL http://www.sciencedirect.com/science/article/pii/S0032591012007140.

[26] Anne Gobin, Hervé Neau, Olivier Simonin, Jean-Richard Llinas, Vince Reiling, and Jean-Lo′fc Sélo. Fluid dynamic numerical simulation of a gas phase polymerization reactor. *International Journal for Numerical Methods in Fluids*, 43(10-11): 1199–1220, 2003.

[27] Jesús Guardiola, Victor Rojo, and Guadalupe Ramos. Influence of particle size, fluidization velocity and relative humidity on fluidized bed electrostatics. *Journal of Electrostatics*, 37(1-2):1–20, 1996.

[28] R. Gupta, D. Gidaspow, and D.T. Wasan. Electrostatic separation of powder mixtures based on the work functions of its constituents. *Powder Technology*, 75(1):79 – 87, 1993. ISSN 0032-5910. doi: https://doi.org/10.1016/0032-5910(93)80027-8. URL http://www.sciencedirect.com/science/article/pii/0032591093800278.

[29] Ziad Hamidouche, Enrica Masi, Pascal Fede, Renaud Ansart, Hervé Neau, Mehrdji Hemati, and Olivier Simonin. Numerical simulation of multiphase reactive flows. In *Advances in Chemical Engineering*, volume 52, pages 51–124. Elsevier, 2018.

[30] Honghao He, Xiaofeng Lu, Wei Shuang, Quanhai Wang, Yinhu Kang, Liyun Yan, Xuanyu Ji, Guangyu Luo, and Hai Liu. Statistical and frequency analysis of the pressure fluctuation in a fluidized bed of non-spherical particles. *Particuology*, 16:178–186, 2014.

[31] Gregory Hendrickson. Electrostatics and gas phase fluidized bed polymerization reactor wall sheeting. *Chemical Engineering Science*, 61(4):1041–1064, February 2006. ISSN 0009-2509. doi: 10.1016/j.ces.2005.07.029. URL http://www.sciencedirect.com/science/article/pii/S0009250905006433.

[32] SS Hsiau and ML Hunt. Kinetic theory analysis of flow-induced particle diffusion and thermal conduction in granular material flows. *Journal of Heat Transfer*, 115(3):541–548, 1993.

[33] Farzaneh Jalalinejad, Xiaotao T. Bi, and John R. Grace. Effect of electrostatic charges on single bubble in gas-solid fluidized beds. *International Journal of Multiphase Flow*, 44:15–28, September 2012. ISSN 0301-9322. doi: 10.1016/j.ijmultiphaseflow.2012.03.008. URL http://www.sciencedirect.com/science/article/pii/S030193221200050X.

[34] Farzaneh Jalalinejad, Xiaotao T. Bi, and John R. Grace. Effect of electrostatics on interaction of bubble pairs in a fluidized bed. *Advanced Powder Technology*, 26 (1):329–334, January 2015. ISSN 0921-8831. doi: 10.1016/j.apt.2014.10.015. URL http://www.sciencedirect.com/science/article/pii/S0921883114002805.

[35] J. T. Jenkins and S. B. Savage. A theory for the rapid flow of identical, smooth, nearly elastic, spherical particles. *Journal of Fluid Mechanics*, 130:187–202, 1983. doi: 10.1017/S0022112083001044.

[36] JAMES T Jenkins and MW Richman. Kinetic theory for plane flows of a dense gas of identical, rough, inelastic, circular disks. *The Physics of fluids*, 28(12): 3485–3494, 1985.

[37] JT Jenkins and MW Richman. Grad's 13-moment system for a dense gas of inelastic spheres. In *The breadth and depth of continuum mechanics*, pages 647–669. Springer, 1986.

[38] KL Johnson. Contact mechanics. *Cambridge University Press, Cambridge*, 1985.

[39] Jari Kolehmainen, Ali Ozel, Christopher M. Boyce, and Sankaran Sundaresan. A hybrid approach to computing electrostatic forces in fluidized beds of charged particles. *AIChE Journal*, 62(7):2282–2295, July 2016. ISSN 1547-5905. doi: 10.1002/aic.15279. URL http://onlinelibrary.wiley.com.proxy.lib.iastate.edu/doi/10.1002/aic.15279/abstract.

[40] Jari Kolehmainen, Ali Ozel, Christopher M Boyce, and Sankaran Sundaresan. Triboelectric charging of monodisperse particles in fluidized beds. *AIChE Journal*, 2016b.

[41] Jari Kolehmainen, Ali Ozel, and Sankaran Sundaresan. Eulerian modelling of gas–solid flows with triboelectric charging. *Journal of Fluid Mechanics*, 848: 340–369, 2018.

[42] Daizo Kunii and Octave Levenspiel. Industrial applications of fluidized beds. *Fluidization engineering*, 2(3):15–60, 1991.

[43] Daizo Kunii and Octave Levenspiel. Fluidization and mapping of regimes. *Fluidization engineering*, 2(3):61–94, 1991.

[44] J. C. Laurentie, P. Traoré, and L. Dascalescu. Discrete element modeling of triboelectric charging of insulating materials in vibrated granular beds. *Journal of Electrostatics*, 71(6):951–957, December 2013. ISSN 0304-3886. doi: 10.1016/j.elstat.2013.08.001. URL http://www.sciencedirect.com/science/article/pii/S0304388613001034.

[45] Shuo Li, Weibin Kong, Huili Zhang, Florian Sabatier, Renaud Ansart, Gilles Flamant, and Jan Baeyens. The fluidized bed air heat exchanger in a hybrid brayton-cycle solar power plant. In *AIP Conference Proceedings*, volume 2126, page 140002. AIP Publishing, 2019.

[46] Ismo V. Lindell, Johan C.-E. Sten, and Keijo I. Nikoskinen. Electrostatic image method for the interaction of two dielectric spheres. *Radio Science*, 28(3):319–329, May 1993. ISSN 1944-799X. doi: 10.1029/92RS02881. URL http://onlinelibrary.wiley.com.proxy.lib.iastate.edu/doi/10.1029/92RS02881/abstract.

[47] S. Matsusaka, H. Maruyama, T. Matsuyama, and M. Ghadiri. Triboelectric charging of powders: A review. *Chemical Engineering Science*, 65(22):5781–5807, November 2010. ISSN 0009-2509. doi: 10.1016/j.ces.2010.07.005. URL http://www.sciencedirect.com/science/article/pii/S0009250910004239.

[48] Shuji Matsusaka, Hiroaki Umemoto, Matami Nishitani, and Hiroaki Masuda. Electrostatic charge distribution of particles in gas–solids pipe flow. *Journal of Electrostatics*, 55(1):81–96, May 2002. ISSN 0304-3886. doi: 10.1016/S0304-3886(01)00185-1. URL http://www.sciencedirect.com/science/article/pii/S0304388601001851.

[49] T. Matsuyama and H. Yamamoto. Charge relaxation process dominates contact charging of a particle in atmospheric conditions. *Journal of Physics D: Applied Physics*, 28(12):2418, 1995. ISSN 0022-3727. doi: 10.1088/0022-3727/28/12/005. URL http://stacks.iop.org/0022-3727/28/i=12/a=005.

[50] N Méchitoua, M Boucker, J Laviéville, J Hérard, S Pigny, and G Serre. An unstructured finite volume solver for two phase water/vapour flows based on an elliptic oriented fractional step method. In *Proc. of The 10th International Topical Meeting on Nuclear Reactor Thermal-Hydraulics (NURETH-10), Seoul, Korea*, 2003.

[51] Poupak Mehrani, Hsiaotao T. Bi, and John R. Grace. Electrostatic charge generation in gas-solid fluidized beds. *Journal of Electrostatics*, 63(2):165–173, February 2005. ISSN 0304-3886. doi: 10.1016/j.elstat.2004.10.003. URL http://www.sciencedirect.com/science/article/pii/S0304388604001937.

[52] Poupak Mehrani, Hsiaotao T. Bi, and John R. Grace. Electrostatic behavior of different fines added to a Faraday cup fluidized bed. *Journal of Electrostatics*, 65 (1):1–10, January 2007. ISSN 0304-3886. doi: 10.1016/j.elstat.2006.05.002. URL http://www.sciencedirect.com/science/article/pii/S0304388606000490.

[53] James R Melcher. *Continuum electromechanics*, volume 2. MIT press Cambridge, MA, 1981.

[54] Carlos Montilla, Renaud Ansart, and Olivier Simonin. Eulerial modeling of mono-dispersed gas-particle flow with electrostatic forces. *Journal of Fluid Mechanics*, 2019. Submitted.

[55] Wajeeh O Moughrabiah, John R Grace, and Xiaotao T Bi. Effects of pressure, temperature, and gas velocity on electrostatics in gas- solid fluidized beds. *Industrial & Engineering Chemistry Research*, 48(1):320–325, 2008.

[56] Wajeeh O. Moughrabiah, John R. Grace, and Xiaotao T. Bi. Electrostatics in gas-solid fluidized beds for different particle properties. *Chemical Engineering Science*, 75:198–208, June 2012. ISSN 0009-2509. doi: 10.1016/j.ces.2012.02.041. URL http://www.sciencedirect.com/science/article/pii/S0009250912001376.

[57] Matti Murtomaa, Eetu Räsänen, Jukka Rantanen, Adrian Bailey, Ensio Laine, Jukka-Pekka Mannermaa, and Jouko Yliruusi. Electrostatic measurements on a miniaturized fluidized bed. *Journal of Electrostatics*, 57(1):91–106, January 2003. ISSN 0304-3886. doi: 10.1016/S0304-3886(02)00121-3. URL http://www.sciencedirect.com/science/article/pii/S0304388602001213.

[58] Hervé Neau, Jérôme Laviéville, and Olivier Simonin. Neptune_cfd high parallel computing performances for particle-laden reactive flows. 2010.

[59] Hervé Neau, Maxime Pigou, Pascal Fede, Renaud Ansart, C. Baudry, Nicolas Merigoux, Jérôme Lavieville, Y. Fournier, N. Renon, and Olivier Simonin. Massively parallel numerical simulation using up to 36,000 cpu cores of an industrial-scale polydispersed reactive pressurized fluidized bed with a mesh of one billion cells. *Powder Technology*, 2019. Submitted.

[60] Ah-Hyung Park, Hsiaotao Bi, and John R Grace. Reduction of electrostatic charges in gas-solid fluidized beds. *Chemical Engineering Science*, 57(1):153–162, January 2002b. ISSN 0009-2509. doi: 10.1016/S0009-2509(01)00352-9. URL http://www.sciencedirect.com/science/article/pii/S0009250901003529.

[61] Ah-Hyung Alissa Park, Hsiaotao T. Bi, John R. Grace, and Aihua Chen. Modeling charge transfer and induction in gas-solid fluidized beds. *Journal of Electrostatics*, 55(2):135–158, June 2002. ISSN 0304-3886. doi: 10.1016/S0304-3886(01)00188-7. URL http://www.sciencedirect.com/science/article/pii/S0304388601001887.

[62] M Ray, F Chowdhury, A Sowinski, P Mehrani, and A Passalacqua. An euler-euler model for mono-dispersed gas-particle flows incorporating electrostatic charging due to particle-wall and particle-particle collisions. *Chemical Engineering Science*, 197:327–344, 2019.

[63] Ram G. Rokkam, Rodney O. Fox, and Michael E. Muhle. Computational fluid dynamics and electrostatic modeling of polymerization fluidized-bed reactors. *Powder Technology*, 203(2):109–124, November 2010. ISSN 0032-5910. doi: 10.1016/j.powtec.2010.04.002. URL http://www.sciencedirect.com/science/article/pii/S0032591010001828.

[64] R.G. Rokkam, A. Sowinski, R.O. Fox, P. Mehrani, and M.E. Muhle. Computational and experimental study of electrostatics in gas-solid polymerization fluidized beds. *Chemical Engineering Science*, 92:146–156, April 2013. ISSN 00092509. doi: 10.1016/j.ces.2013.01.023. URL http://linkinghub.elsevier.com/retrieve/pii/S0009250913000365.

[65] Marc Sakiz and Olivier Simonin. Development and validation of continuum particle wall boundary conditions using lagrangian simulation of a vertical gas-solid channel flow. In *Proc of FEDSM*, volume 99, 1999.

[66] Fawzi Salama, Andrew Sowinski, Khaled Atieh, and Poupak Mehrani. Investigation of electrostatic charge distribution within the reactor wall fouling and bulk regions of a gas-solid fluidized bed. *Journal of Electrostatics*, 71(1):21–27, February 2013. ISSN 0304-3886. doi: 10.1016/j.elstat.2012.11.002. URL http://www.sciencedirect.com/science/article/pii/S0304388612001167.

[67] L. B. Schein, M. LaHa, and D. Novotny. Theory of insulator charging. *Physics Letters A*, 167(1):79–83, July 1992. ISSN 0375-9601. doi: 10.1016/0375-9601(92)90630-5. URL http://www.sciencedirect.com/science/article/pii/0375960192906305.

[68] Jaber Shabanian and Jamal Chaouki. Effects of temperature, pressure, and interparticle forces on the hydrodynamics of a gas-solid fluidized bed. *Chemical*

Engineering Journal, 313:580–590, 2017.

[69] O Simonin. Second-moment prediction of dispersed phase turbulence in particle-laden flows. In *8th Symposium on Turbulent Shear Flows, Volume 1*, volume 1, pages 7–4, 1991.

[70] O Simonin. Statistical and continuum modelling of turbulent reactive particulate flows part i; theoretical derivation of dispersed eulerian modelling from probability density function kinetic equations, part ii; application of a two phase second moment transport model for the prediction of turbulent gas-particle flows. *Theoretical and Experimental Lecture Series 2000*, 6, 2000.

[71] O Simonin, E Deutsch, and JP Minier. Eulerian prediction of the fluid/particle correlated motion in turbulent two-phase flows. *Applied Scientific Research*, 51 (1-2):275–283, 1993.

[72] Petteri Sippola, Jari Kolehmainen, Ali Ozel, Xiaoyu Liu, Pentti Saarenrinne, and Sankaran Sundaresan. Experimental and numerical study of wall layer development in a tribocharged fluidized bed. *Journal of Fluid Mechanics*, 849: 860–884, 2018.

[73] Andrew Sowinski, Fawzi Salama, and Poupak Mehrani. New technique for electrostatic charge measurement in gas-solid fluidized beds. *Journal of Electrostatics*, 67(4):568–573, July 2009. ISSN 0304-3886. doi: 10.1016/j.elstat.2008.11.005. URL `http://www.sciencedirect.com/science/article/pii/S0304388608001253`.

[74] Andrew Sowinski, Leigh Miller, and Poupak Mehrani. Investigation of electrostatic charge distribution in gas-solid fluidized beds. *Chemical Engineering Science*, 65(9):2771–2781, May 2010. ISSN 0009-2509. doi: 10.1016/j.ces.2010.01.008. URL `http://www.sciencedirect.com/science/article/pii/S0009250910000175`.

[75] Andrew Sowinski, Antonio Mayne, and Poupak Mehrani. Effect of fluidizing particle size on electrostatic charge generation and reactor wall fouling in gas-solid fluidized beds. *Chemical Engineering Science*, 71:552–563, March 2012. ISSN 0009-2509. doi: 10.1016/j.ces.2011.11.031. URL `http://www.sciencedirect.com/science/article/pii/S000925091100830X`.

[76] P.S.B. Stewart and J.F. Davidson. Slug flow in fluidised beds. *Powder Technology*, 1(2):61 – 80, 1967. ISSN 0032-5910. doi: http://dx.doi.org/10.1016/0032-5910(67)80014-7. URL `http://www.sciencedirect.com/science/article/pii/0032591067800147`.

[77] Milad Taghavivand, Bilal Elchamaa, Andrew Sowinski, and Poupak Mehrani. Study of electrostatic charging of single particles during pneumatic conveying. *Powder Technology*, 355:242–250, 2019.

[78] Zhen Tan, Cai Liang, Junfei Li, and Shuzhao Zhang. The effect of electrostatics on single bubble in fluidized bed and its mechanism analysis. *Powder Technology*, 325:545–556, 2018.

[79] Hongxiang Tang, Rui Song, Yan Dong, and Xiaoyu Song. Measurement of

restitution and friction coefficients for granular particles and discrete element simulation for the tests of glass beads. *Materials*, 12(19):3170, 2019.

[80] Elhadji I Thiam, Enrica Masi, Eric Climent, Olivier Simonin, and Stéphane Vincent. Particle-resolved numerical simulations of the gas–solid heat transfer in arrays of random motionless particles. *Acta Mechanica*, 230(2):541–567, 2019.

[81] V Thonglimp, N Hiquily, and C Laguerie. Vitesse minimale de fluidisation et expansion des couches fluidisées par un gaz. *Powder technology*, 38(3):233–253, 1984.

[82] Florence Vanni, Brigitte Caussat, Carine Ablitzer, and Méryl Brothier. Effects of reducing the reactor diameter on the fluidization of a very dense powder. *Powder Technology*, 277:268–274, 2015.

[83] O Vermorel, Benoit Bedat, Olivier Simonin, and Thierry Poinsot. Numerical study and modelling of turbulence modulation in a particle laden slab flow. *Journal of Turbulence*, 4(25):1–39, 2003.

[84] Bernd Wachmann and Stefan Schwarzer. Three-dimensional massively parallel computing of suspensions. *International Journal of Modern Physics C*, 9(05):759–775, 1998.

[85] CY Wen and YH Yu. A generalized method for predicting the minimum fluidization velocity. *AIChE Journal*, 12(3):610–612, 1966.

[86] J Werther and O Molerus. The local structure of gas fluidized beds—ii. the spatial distribution of bubbles. *International Journal of Multiphase Flow*, 1(1):123–138, 1973.

[87] A Wolny and I Opaliǹski. Electric charge neutralization by addition of fines to a fluidized bed composed of coarse dielectric particles. *Journal of electrostatics*, 14 (3):279–289, 1983.

[88] Wen-Ching Yang. Modification and re-interpretation of geldart's classification of powders. *Powder Technology*, 171(2):69 – 74, 2007. ISSN 0032-5910. doi: http://dx.doi.org/10.1016/j.powtec.2006.08.024. URL `http://www.sciencedirect.com/science/article/pii/S003259100600369X`.

[89] Li Yao, Hsiaotao T. Bi, and Ah-Hyung Park. Characterization of electrostatic charges in freely bubbling fluidized beds with dielectric particles. *Journal of Electrostatics*, 56(2):183–197, September 2002. ISSN 0304-3886. doi: 10.1016/S0304-3886(02)00062-1. URL `http://www.sciencedirect.com/science/article/pii/S0304388602000621`.

[90] Joseph Yerushalmi and NT Cankurt. Further studies of the regimes of fluidization. *Powder Technology*, 24(2):187–205, 1979.

[91] H Zhao, GSP Castle, II Inculet, and AG Bailey. Bipolar charging in polydisperse polymer powders in industrial processes. In *Industry Applications Conference, 2000. Conference Record of the 2000 IEEE*, volume 2, pages 835–841. IEEE, 2000.